Relevance of cGAMP-mediated bystander cell activation and cooperation of cGAS and TLR signaling in TREX1-related autoimmunity

Dissertation

zur

Erlangung des Doktorgrades (Dr. rer. nat.)

der

Mathematisch-Naturwissenschaftlichen Fakultät

der

Rheinischen Friedrich-Wilhelms-Universität Bonn

vorgelegt von

Bianca B. Jütte

aus

Schwelm

Bonn, Juli 2020

Angefertigt mit Genehmigung der Mathematisch-Naturwissenschaftlichen Fakultät der Rheinischen Friedrich-Wilhelms-Universität Bonn

Teile dieser Arbeit wurden im Juni 2020 bei der wissenschaftlichen Fachzeitschrift *Cell Reports* zur Veröffentlichung eingereicht.

	Erstgutachter	Prof. Dr. Peter Brossart
	Zweitgutachter	Prof. Dr. Sven Burgdorf
3.	Mitglied der Promotionskommission	Prof. Dr. Jörg Wenzel
4.	Mitglied der Promotionskommission	Prof. Dr. Jochen Dingfelder

Tag der Promotion: 25.09.2020

Erscheinungsjahr: 2020

Table of Contents

Table of Contents

Summary

The aberrant recognition of endogenous nucleic acids by innate immune sensors can trigger a wide range of autoimmune and autoinflammatory conditions, mediated by type I interferons. Loss-of-function mutations in the three prime repair exonuclease 1 (TREX1) cause cytosolic accumulation of DNA, which is recognized by the cyclic dinucleotide 2',3'-GMP-AMP (cGAMP) synthase (cGAS). cGAS catalyzes the formation of the second messenger cGAMP that in turn activates the signaling protein STING (stimulator of interferon genes). Bystander activation is a critical component of the host defense system against pathogens but has likewise been linked to the development of autoinflammatory and autoimmune diseases. During viral infections, intercellular transmission of the second messenger cGAMP represents a potent mode of bystander activation that enhances pathogen defense.

In the first part, a murine bone marrow transplantation strategy was used to demonstrate that in *Trex1*$^{-/-}$-associated autoimmunity, cGAMP shuttling from radio-resistant to immune cells induces interferon regulatory factor 3 (IRF3) phosphorylation and subsequent tonic interferon signaling, as well as NF-κB (nuclear factor kappa-light-chain enhancer of activated B cell) activation. cGAMP travel protected lymphocytes and myeloid cells from apoptosis promoting their accumulation in secondary lymphoid tissue. Innate immune activation, however, did not induce B cell differentiation into autoantibody-producing plasmablasts or aberrant T cell priming in the steady state. Furthermore, cGAMP-mediated bystander activation did not lead to spontaneous organ disease, but triggered interface dermatitis after UV light exposure. These findings thus reveal that in TREX1 deficiency intercellular cGAMP transfer elicits innate immunity and, under conducive environmental conditions, triggers tissue inflammation.

The co-activation of distinct nucleic acid-sensing pathways was analyzed in the second part of my thesis. Apart from cytosolic detection of DNA by cGAS, endosomal Toll-like receptors (TLRs) can also sense endogenous nucleic acids and thus trigger immune activation. Here, the *Unc93b1* 3d mouse model was used, in which endosomal TLR signaling

is impaired, to investigate whether nucleic acid sensing by TLRs contributes to autoimmunity in TREX1-deficient mice. *Trex1*$^{-/-}$*;Unc93b1*$^{3d/3d}$ animals revealed overall elevated tissue inflammation and T cell organ infiltration, leading to more pronounced myocarditis in the absence of endosomal TLRs. However, non-functional endosomal TLR signaling resulted in an improved survival of these animals, presumably attributed to virtually absent antibodies against self-nucleic acids. Furthermore, antibody-forming cells were reduced to wild-type levels in animals missing either STING or TLR signaling. Thus, my experiments indicate that TLRs greatly modulate autoimmunity that is primarily driven by the cGAS-STING pathway. Taken together, my results provide important insights into mechanisms of autoimmunity development, crucial for the identification of novel therapeutic strategies.

Zusammenfassung

Die fälschliche Erkennung endogener Nukleinsäuren durch angeborene Immunsensoren kann ein breites Spektrum autoimmuner und autoinflammatorischer Krankheiten auslösen, die durch Typ-I-Interferone vermittelt werden. Mutationen, die zu einer Fehlfunktion in der 3'-Exonuklease 1 (TREX1) führen, verursachen eine Anhäufung von DNA im Zytosol, die von der zyklischen Dinukleotid 2',3'-GMP-AMP (cGAMP)-Synthase (cGAS) erkannt wird. cGAS katalysiert die Bildung des Botenstoffs cGAMP, der wiederum STING (für: *stimulator of interferon genes*) aktiviert. Die Bystander-Aktivierung ist eine wichtige Komponente des Abwehrsystems des Wirts gegen Krankheitserreger, wurde aber ebenfalls mit der Entwicklung von Autoinflammation und Autoimmunerkrankungen in Verbindung gebracht. Bei Virusinfektionen stellt die interzelluläre Übertragung des Botenstoffs cGAMP eine wichtige Art der Bystander-Aktivierung dar, der die Pathogenabwehr steigert.

Im ersten Teil dieser Arbeit wurde die Strategie der Knochenmarkstransplantation in Mäusen angewandt, um zu zeigen, dass bei *Trex1*$^{-/-}$-assoziierter Autoimmunität die cGAMP-Übertragung von bestrahlungsresistenten Immunzellen auf Nachbarzellen die Phosphorylierung des Interferon-Regulationsfaktors 3 (IRF3), ein sich anschließendes

tonisches Interferon-Signal, sowie die Aktivierung des NF-κB (*nuclear factor kappa-light-chain-enhancer of activated B cell*)-Signalwegs induziert. cGAMP-Übertragung schützte Lymphozyten und myeloische Zellen vor Apoptose und förderte ihre Akkumulation im sekundären lymphatischen Gewebe. Die angeborene Immunantwort *per se* induzierte jedoch weder die Differenzierung von B-Zellen in Autoantikörper-produzierende Plasmablasten noch eine abnormale T-Zell-Aktivierung. Darüber hinaus führte die cGAMP-vermittelte Bystander-Aktivierung zu keiner spontanen Organentzündung, löste allerdings nach UV-Lichtexposition eine Dermatitis aus. Diese Ergebnisse machen deutlich, dass bei TREX1-Mangel der interzelluläre cGAMP-Transfer eine angeborene Immunantwort hervorruft und unter bestimmten Umweltbedingungen eine Entzündung des betroffenen Gewebes auslöst.

Die Koaktivierung verschiedener Nukleinsäure-Sensorwege war Gegenstand der Untersuchung im zweiten Teil meiner Arbeit. Neben der zytosolischen Erkennung von DNA durch cGAS können auch endosomale Toll-like-Rezeptoren (TLRs) endogene Nukleinsäuren erkennen und damit eine Immunaktivierung auslösen. Hier wurde anhand des *Unc93b1*-3d-Mausmodells, in dem die endosomale TLR-Expression gestört ist, untersucht, ob die Erkennung von Nukleinsäuren durch TLRs zur Autoimmunität bei TREX1-defizienten Mäusen beiträgt. Die *Trex1*$^{-/-}$;*Unc93b1*$^{3d/3d}$-Tiere zeigten insgesamt eine vermehrte Gewebeentzündung und T-Zell-Organ-Infiltration, was in Abwesenheit endosomaler TLRs zu einer ausgeprägteren Myokarditis führte. Defekte in endosomalen TLR-Signalwegen führten zu einem verbesserten Überleben dieser Tiere, was vermutlich in Zusammenhang mit nahezu nicht vorhandenen Auto-Antikörpern steht. Darüber hinaus waren die Antikörper-bildenden Zellen bei Tieren, bei denen entweder kein STING- oder TLR-Signal vorhanden war, auf Wildtyp-Niveau reduziert. Meine Experimente zeigen also, dass TLRs die Autoimmunität, die hauptsächlich durch den cGAS-STING-Signalweg gesteuert wird, stark modulieren. Zusammengenommen liefern meine Ergebnisse wichtige Einblicke in die Mechanismen der Autoimmunitätsentwicklung, die für die Identifizierung neuer therapeutischer Strategien entscheidend sind.

1 Introduction

1.1 Innate and adaptive immune system

To generate an effective host defense against infectious challenges, mammals are equipped with two main different types of immune response against invading pathogens: the innate and the adaptive, also called "acquired" immune system. An important part of the **innate immune system** comprises a number of receptors that recognize highly conserved microbial components, termed pathogen-associated molecular patterns (PAMPs). Since PAMPs often provide characteristic properties for a specific class of pathogens, such as lipopolysaccharides for Gram-negative bacteria, they significantly contribute to the choice of effector mechanisms by the immune system to eliminate a particular class of pathogen most efficiently.[1] The corresponding receptors are called pattern recognition receptors (PRRs), recognizing diverse microbial patterns, including complex polysaccharides, glycolipids, lipoproteins, flagellin, nucleotides and nucleic acids (NAs). Self-NAs are abundantly present in eukaryotic cells, necessitating efficient differentiation mechanisms from pathogen-derived NAs. Intrinsic host DNA is mainly contained in the nucleus and in mitochondria, leaving the cytoplasm largely free of self-DNA. Hence, the occurrence of NAs in the cytosol indicates either infection or cellular damage.[2] The innate immune system therefore also recognizes indicators of host cell damage, so-called danger-associated molecular patterns (DAMPs). Notably, both PAMPs and DAMPs are partly sensed by the exact same PRRs. For example, the NA sensor cGAS (cyclic dinucleotide 2',3'-GMP-AMP (cGAMP) synthase) detects both viral DNA and host DNA in the cytoplasm.

PRRs can be expressed by hematopoietic and non-hematopoietic cells and are able to initiate a protective inflammatory response within minutes after pathogen encounter, translating into distinct effector responses, but also trigger the subsequent long-term **adaptive immune response.**[3] Presentation of microbial antigens (name derived from antibody generators) by PRR-activated antigen-presenting cells (APCs), particularly dendritic cells (DCs), is crucial for the succeeding antigen-specific T and B cell response.

This process also generates an immunological memory, required for an enhanced response to repeated encounters with the same pathogen.

1.2 Nucleic acid sensing

Microbial NAs have been identified as major triggers of innate immune responses via PRRs. Interestingly, besides its function of carrying genetic information, DNA has even longer been known for stimulating immune responses.[4] The presence of DNA in the cytoplasm of mammalian cells is perceived as a signal of infection or danger due to the invasion of pathogens and leakage of DNA from the nucleus, respectively, indicating the occurrence of some sort of pathological condition. The best characterized NA-sensing PRRs include the Toll-like receptors (TLRs) 3, 7, 8, and 9, the RIG-I-like receptors (RLRs), cyclic guanosine-monophosphate adenosine-monophosphate synthase (cGAS), and absent in melanoma 2 (AIM2).

1.2.1 cGAS / STING signaling pathway

One of the most important cytosolic DNA sensors is cGAS, a nucleotidyltransferase, detecting double-stranded DNA (dsDNA) with at least 24 base pairs in length, sequence-independently, and, notably, without self-non-self-discrimination. Recently, it has been shown that cGAS is also stimulated by short single-stranded DNA (ssDNA) strands, featuring a stem-loop Y form, in a sequence-specific manner.[5] Stimulatory binding of DNA causes a conformational change in the active site of cGAS and the formation of cGAS-DNA dimers, triggering the production of the second messenger cGAMP, which contains mixed 2'-5' and 3'-5' phosphodiester bonds and is therefore also termed 2'-3'-cGAMP.[6–9] cGAMP binds to the endoplasmatic reticulum (ER)-localized protein stimulator of interferon genes (STING, encoded by *Tmem173*) and leads to its activation by a series of structural changes. Subsequently, STING recruits the TANK binding kinase 1 (TBK1) and translocates it to the perinuclear compartment. The STING-TBK1-complex in turn phosphorylates the

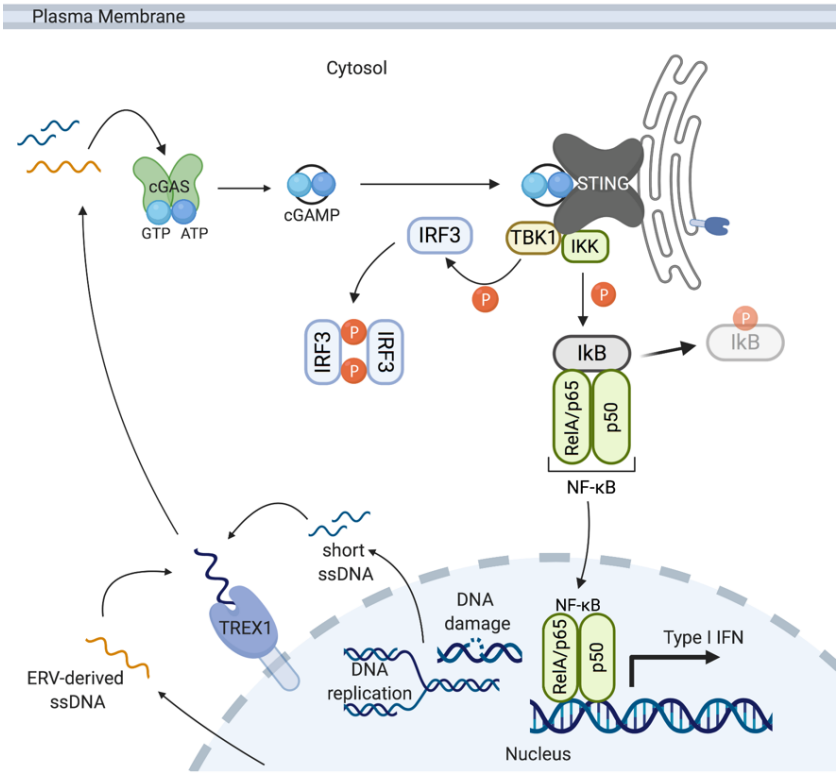

Figure 1. Sensing of cytosolic DNA via the cGAS-STING pathway. Cytosolic DNA acts as a pattern associated molecular pattern (PAMP) detected by pattern recognition receptors (PRRs) as for example cGAS, which catalyzes the production of the second messenger cyclic GMP-AMP (2'3'-cGAMP) from ATP and GTP. cGAMP binds to the adaptor molecule stimulator of interferon genes (STING) which recruits several kinases, such as TANK-binding kinase 1 (TBK1) and inhibitor of κB kinase (IKK). TBK1 and IKK phosphorylate the interferon regulatory factor 3 (IRF3) and inhibitor of NF-κB (IκB), respectively, resulting in both activated IRF3 and NF-κB to enter the nucleus and switch on the expression of a variety of immunomodulatory molecules. Figure created with BioRender.

transcription factor IFN regulatory factor 3 (IRF3), which then dimerizes and enters the nucleus in order to induce type I IFN and inflammatory cytokine production (Fig. 1).[10,11]

Moreover, STING can also activate the NF-κB (nuclear factor kappa-light-chain-enhancer of activated B cell) signaling pathway. NF-κB acts as a crucial regulator of inflammation, proliferation, and cell death, tightly controlled by the inhibitor of κB (IκB), which under normal conditions prevent NF-κB from entering the nucleus to induce the expression of IFNs and inflammatory cytokines. STING activation causes recruitment of the inhibitor of κB kinase (IKK), phosphorylating IκB to be degraded and thereby releasing

NF-κB.[2,12,13] Notably, IKK not only phosphorylates IκB, but also NF-κB, in which serine 536 of the RelA/p65 subunit represents the most potent phosphorylation site in terms of NF-κB activation in response to inflammatory stimuli.[14–17]

1.2.2 Toll-like receptor signaling

PRRs are a set of structurally, as well as functionally heterogenous proteins.[18] However, they are highly conserved between different species, as for example Drosophila and humans, as shown by the example of TLRs. These PRRs are transmembrane receptors containing an extracellular leucin-rich repeat (LRR) domain and a cytosolic signaling domain in both humans and flies, and play a crucial role in their immune systems.[1] It has been shown that, regardless of the species, different TLRs recognize distinct classes of pathogens and subsequently trigger an appropriate immune response cascade upon activation, that is most active against this exact kind of pathogen.[19] Furthermore, the location of TLRs may vary, depending on the presumable site of pathogen encounter.

There are 10 characterized TLR genes in humans (TLR1-TLR10) and 12 TLR genes in the murine (TLR1-TLR9, TLR11-TLR13) genome, each featuring different specificities. Based on their location, TLRs can be classified into two major categories, namely surface TLRs that comprise TLR1, TLR2, TLR4, TLR5, TLR6, and human TLR10, and intracellular TLRs, which cover TLR3, TLR7, TLR8, TLR9, TLR11, TLR12, and TLR13.[20] In humans as well as in mice, one common characteristic of TLRs 3, 7, 8, and 9 is the recognition of NAs in the endosomal compartment. TLR3 detects long double-stranded RNA (dsRNA) sequences, which are not supposed to be present in the endosomes of normal cells and therefore might be a sign of a viral infection, because cellular RNAs are commonly single-stranded. TLR7 and TLR8 are tandem duplicated genes on the X-chromosome, exhibiting different expression patterns, as TLR7 is mostly expressed by plasmacytoid dendritic cells (pDCs) and B cells, whereas TLR8 is highly expressed by myeloid cells, but absent in pDCs and B cells.[19,21] They both surveil phagocytic cargo for microbial RNA and presumably sense short ssRNA-degradation products.[22] TLR9 is activated by ssDNA fragments, produced by the endosomal deoxyribonuclease II (DNase II), which contain unmethylated CpG-rich motifs.

CpG dinucleotides are more frequent in microbial DNA than in mammalian cells, in which they additionally are mostly methylated.[23]

Generally, TLRs are synthesized in the ER and transported to their respective location in the cell, which are either the plasma membrane or endosomal membranes.[24] Notably, the unc-93 homolog B1 (UNC93B1) membrane protein has found to be a critical co-factor for trafficking of NA-sensing TLRs from the endoplasmatic reticulum (ER) to their endosomal target location.[25] More recently, it has been shown that UNC93B1 is furthermore required for the cell surface expression of the flagellin receptor TLR5.[26] Loss-of-function mutation in the *Unc93b1* gene (referred to as 3d mutation) obstructs maturation and expression of the endosomal TLRs and thus leads to a drastically impaired activity.[27]

1.3 DNA metabolism

To prevent the aberrant activation of DNA receptors, three main families of mammalian DNases are known to degrade DNA with different modes and sites of action. Defects in all of these DNases eventually lead to the accumulation of endogenous NAs and subsequently to the development of autoimmunity.

The **DNase I** family comprises at least four similar but distinct enzymes known to date: DNase I, DNase X, DNase1L3, and DNase1L2,[28] all of which are endonucleases and the major nucleases present in serum.[29,30] Cleaving both ssDNA and dsDNA in the extranuclear space, this nucleases are responsible for chromatin breakdown during apoptosis as well as for the clearance of circulating DNA debris originating from apoptotic and necrotic cell death.[31] Interestingly, numerous indications point to an involvement of apoptosis-derived DNA as a source of auto-antigens in systemic lupus erythematosus (SLE)[32] Indeed, mice deficient for DNase I and DNase1L3 manifest features similar to human SLE, exhibiting increased anti-nuclear antibodies as well as higher prevalence of glomerulonephritis.[33]

DNase II is a mammalian lysosomal endonuclease, located in various tissues and is also crucial for the degradation of debris caused by homeostatic erythropoiesis and apoptosis.[34,35] It is mainly accountabl

e for the digestion of exogenous DNA incorporated by endocytosis of *e.g.* pathogen-derived NAs.[31]

In the absence of DNase II, undigested DNA is potentially translocated into the cytoplasm, where it activates cytoplasmic DNA sensors. Undigested DNA is sensed by PRRs with a subsequent induction of excessive, embryonically lethal type I IFN production. In the absence of a functional type I IFN-receptor, mice defective for DNase II survive to adulthood, but develop autoimmunity based on the production of self-directed anti-nuclear antibodies (ANAs) later on.[36]

Three prime repair exonuclease 1 (TREX1), also termed **DNase III**, was first described in 1969 and is a dimeric cytosolic exonuclease, degrading ssDNA and dsDNA from the 3' end, thereby releasing 5'-mononucleotides as degradation product.[37] With its C-terminal hydrophobic domain, it associates with the endoplasmatic reticulum (ER) membrane or the outer nuclear membrane, facing the nuclease domain towards the cytosol. Thus, TREX1 functions as a sentinel nuclease to ensure immediate degradation of DNA metabolites leaking out of the nucleus.[38]

In the cytosol, TREX1 is essentially involved in the clearance of DNA. Different models have been discussed regarding the source of abundant cytosolic DNA to be degraded by TREX1, one of which is the continuous leakage of aberrant replication intermediate NAs potentially leading to a chronic activation of the DNA damage response pathway.[39] DNA damage repair also involves the excision of short ssDNA byproducts, emanating into the cytosol.[38] Furthermore, accumulating DNA is suggested to originate from apoptotic cells[40] or endogenous retroelement replication, transpiring unrestricted in TREX1 deficiency and resulting in the activation of the cGAS-STING pathway with subsequent IFN type I production.[41,42] TREX1 in turn prevents the recognition of self-DNA by cytosolic NA sensors such as cGAS, which ultimately leads to autoimmunity.[43] Consequently, in humans, lack of TREX1 or loss-of-function mutations are associated with autoimmune conditions as for example Aicardi-Goutières Syndrome (AGS) or SLE. Strikingly, mutations in *Trex1* represent the highest known risk factor documented for a single susceptibility gene for the development of polygenic SLE.[44] In mice, mutations of *Trex1* are known to cause

inflammatory myocarditis associated with massively impaired survival.[29] In summary, functional TREX1 acts as a crucial negative regulator of an IFN-stimulating response to endogenous DNA that could lead to potentially lethal autoimmunity.

1.4 Nucleic acid-driven autoinflammation and autoimmunity

Aberrant recognition of endogenous NAs by innate sensors comprising either endosomal TLRs or cytosolic sensors such as cGAS can trigger the development of a wide range of autoinflammatory and autoimmune diseases. Those are characterized by elevated levels of IFNs, particularly type I IFNs (α/β), but also type II (γ) and III (λ) IFNs, which control overlapping gene sets. IFNs influence the general activation of innate and adaptive immune cells, which is important for an effective clearance of pathogens. Moreover, erroneous regulation due to the recognition of self-NAs might trigger DC maturation with increased expression of MHC (major histocompatibility complex) class I and II molecules presenting endogenous antigens, promoting the production of self-reactive antibodies by B cells. Further dysregulation via type I IFNs affects lymphocytes, leading to an expansion of autoreactive T and B cells.[45] Besides modulating immune cells, type I IFNs also influence endothelial function, potentially contributing to an increased risk for cardiovascular conditions found in autoimmunity.[46]

An excessive induction of type I IFNs caused by disturbed recognition of endogenous NAs is commonly referred to as type I interferonopathy. AGS, as the prototype of type I interferonopathies, is a monogenic disease, clinically resembling symptoms of viral infections, but also featuring systemic autoimmunity, attributed to a single gene defect.[47,48] SLE on the other hand, is a multi-factorial polygenic disorder, which is likewise characterized by tissue inflammation affecting multiple organs. In humans, it predominantly affects young women with a female to male ratio of about 9:1, but the severity does not differ between sexes.[49] A wide spectrum of symptoms involve numerous organs and systems, for example the skin (causing the typical “butterfly rash” in lupus patients), joints, kidneys, lungs, central nervous system, and hematopoietic system. Therefore,

clinical presentations are strikingly heterogeneous,[50] with Lupus nephritis most commonly causing morbidity and mortality.[51]

There is a paucity of information how different NA sensors together might establish the full clinical spectrum of autoimmune disease. For example, in DNase II-deficient mice, a model for defective DNA clearance, it has been shown that the diversity of disease manifestation depends on different signaling pathways, such as the cGAS-STING axis, which modulates arthritis, and on the other hand endosomal TLRs, which are indispensable for the production of ANAs.[35] Thus, the co-activation of NA sensors might play an important role in the development of autoimmunity, but is scarcely investigated.

1.5 Bystander Activation

Bystander activation in the context of an antimicrobial response represents a special form of intercellular communication, in which infected cells trigger immune signals in previously uninvolved neighboring cells to rapidly boost an immune response and circumvent pathogen-mediated inhibition of the immune response in the directly infected cell.[52] Bystander cell activation was first defined in 1996 as a heterologous activation of non-antigen-specific T cells in a T cell receptor (TCR)-independent manner in order to explain a massive expansion of T cells after a viral infection.[53] Accordingly, bystander cell activation was later on defined as a cellular immune response unspecific for the pathogenic antigen, mediated by indirect signals, such as cytokines and chemokines, and without the involvement of specific B or T cell receptors. However, several studies suggested that the majority of activated T cells related to pathogen infection are antigen-specific and only fractionally dependent on bystander activation.[54,55] Holmgren *et al.* defined bystander cell activation in a more universal manner as uninvolved cells in close proximity to directly infected cells, that induce immune signaling even though lacking a direct pathogen encounter.[52]

The intercellular transfer of the second messenger molecule cGAMP has recently been identified as a novel mechanism of bystander activation.[56] Initially, it was demonstrated that cGAMP can be shuttled to neighboring cells via gap junction, bypassing the need for

cell-intrinsic PRR engagement in the recipient cell. Later studies demonstrated that cGAMP may, among others, also be packaged into viral particles and thereby transferred into newly infected cells.[57] Another novel study identified the LRRC8 protein-comprising volume-regulated anion channel to be critically involved in the host defense against viral infection. Herein, cGAMP was shuttled across plasma membranes to promote STING-dependent IFN response in bystander cells.[58]

Altogether, these studies revealed a role for cGAMP-mediated bystander activation in inducing a robust type I IFN response in viral and bacterial infections. In addition to its physiological function, the activation of bystander cells has been connected to the development of several autoimmune conditions, characterized by a loss of immunological tolerance to self-antigens. In co-culture experiments, TREX1-deficient mouse embryonic fibroblasts induce cGAS-dependent bystander activation, suggesting that intercellular cGAMP transmission is indeed conducive to the development of autoimmunity.[59] Nonetheless, very few studies available to date address the relevance of cGAMP transfer *in vivo,* and none of them has substantiated cGAMP-mediated bystander activation in the context of autoimmunity so far.[60–62]

1.6 Project outline

In this study, I investigated the mechanisms underlying autoimmune diseases that are primarily driven by the DNA sensor cGAS, such as autoimmunity in the *Trex1*$^{-/-}$ mouse model. Specifically, two key aspects were addressed:

First, I examined the implication of bystander cell activation by intercellular cGAMP transfer on promoting disease development in TREX1 deficiency. It is unclear, whether cells have to be directly stimulated by NAs in order to promote immune responses. Since the activation of originally uninvolved bystander cells has been suggested to play a role in autoimmune conditions[56,58,63,64], it is conceivable that the transfer of the second messenger cGAMP might substantially contribute to the development of autoimmunity. Here, a bone marrow transplantation model was used to examine whether cGAMP shuttling contributes

to hallmarks of autoimmunity such as type I IFN expression, autoantibody formation and organ inflammation *in vivo*.

Second, I studied how the interplay of signals derived from the co-detection of NAs in the cytosol and endosomes by cGAS/STING and TLRs, respectively, shape autoimmunity in TREX1 deficiency. Due to the complexity of autoimmune diseases, little is known about the functional interactions of distinct NA sensors. Here, a deficiency model for endosomal TLRs harboring the *Unc93b1* 3d mutation was used to reveal the impact of TLR-mediated immune activation in *Trex1*$^{-/-}$-related autoimmune disease.

In summary, two specific aims can be defined for this thesis:

Aim 1: Relevance of intercellular cGAMP transfer for disease in *Trex1*$^{-/-}$ mice.

Aim 2: Effect of TLR signaling on disease manifestation in TREX1 deficiency.

2 Animals and Materials

2.1 Mice

All mice were maintained under specific pathogen-free conditions with food and water *ad libitum* in individual ventilated cages in the house of experimental therapy, Bonn University Clinics. All procedures were performed in accordance with institutional guidelines and the German Federal Regulations of Animal Experimentation of the *Landesamt für Natur, Umwelt und Verbraucherschutz*, as well as the German Animal Welfare Act.

2.1.1 *Trex1*$^{-/-}$ mice

B6;129P2-*Trex1*^{tm1Tld} (*Trex1*$^{-/-}$) mice were kindly provided by Tomas Lindahl (Cancer Research UK, London) and backcrossed to C57BL/6J (purchased from Jackson Laboratories, Bar Harbor, USA) mice for at least 10 generations. Initially generated by targeted disruption of the *Trex1* gene via replacement of the sequence encoding for amino acid residues 103 to 207 with a *neo* cassette, this mouse strain is considered a model for inflammatory myocarditis and autoimmune disease.[29]

2.1.2 *Trex1*$^{-/-}$*; Tmem173*$^{gt/gt}$ mice

C57BL/6J-*Tmem173*^{gt}/J mice were originally published by Sauer *et al.* in 2011[65] and purchased from Jackson Laboratories. The goldenticket (gt) mutation refers to a chemically induced missense mutation in exon 6 of the transmembrane protein 173 (*Tmem173* translating to STING). This mutant harbors an isoleucine to asparagine change in amino acid residue 199 (I199N) of the protein's C terminus leading to non-existent STING expression. Mice double-deficient for TREX1 and STING (*Trex1*$^{-/-}$*;Tmem173*$^{gt/gt}$) were generated by intercrossing. Genotyping was performed via PCR for *Trex1*$^{-/-}$ and Sanger sequencing (Seqlab, Göttingen) for *Tmem173*$^{gt/gt}$, respectively.

2.1.3 *Mb21d1*$^{-/-}$ mice

B6(C)-*Cgas*$^{tm1d(EUCOMM)Hmgu}$/J mice exhibit a defect in the *Mb21d1* gene, encoding for cytosolic cGAS, caused by the excision of exon 2, which includes the active catalytic domain.[66] Mice were purchased from Jackson Laboratories and backcrossed to C57Bl/6J mice for at least 10 generations.

2.1.4 *Trex1*$^{-/-}$*;Unc93b1*$^{3d/3d}$ mice

Mice deficient for TREX1 harbor the additional 3d mutation in the unc-93 homolog B1. This mutation was initially named triple defect mutation as it has been found to result in a loss of function of the nucleic acid-recognizing TLR3 (detecting dsRNA), TLR7 (ssRNA), and TLR9 (CpG DNA) in mice.[67] Nowadays it is known that UNC93B1 is also essential for a functional TLR5 (flagellin receptor) and TLR8.[27] This mutant mouse line was generated by usage of the mutagen N-ethyl-N-nitrosourea, resulting in a single-nucleotide substitution in exon 9 at histidine 412 towards arginine (H412R). *Unc93b1*$^{3d/3d}$ mice were bred homozygously. Mice double-deficient for TREX1 and UNC93B1 were generated by intercrossing. Genotyping was performed by PCR for *Trex1*$^{-/-}$ and Sanger sequencing (Seqlab) for *Unc93b1*$^{3d/3d}$, respectively.

2.2 Synthetic oligonucleotide primers for qPCR

All oligonucleotides were synthesized by Thermo Fisher (Waltham, USA) and reconstituted in molecular grade water at a concentration of 100 µM.

Primer Sequences (5' → 3')

Mb21d1_common_fwd	ATA TTT CCC CCT GTG TTG GA
Mb21d1_mutant_rev	CGG ATG GAT GAA CAA ACA GA
CCR2_fwd	TTA CCT CAG TTC ATC CAC GG
CCR2_rev	ACA TGT TGC CCA CAA AAC CA

2.3 Synthetic oligonucleotide primers for mouse genotyping

All oligonucleotides were synthesized by Thermo Fisher and reconstituted in molecular grade water at a concentration of 40 µM.

Mouse Line	**Primer Name**	**Primer Sequence (5' → 3')**
***Mb21d1* (cGAS)** knockout *Expected bands:* *wt: 188 bp; mutant 298 bp*	Mb21d1_common_fwd	ATA TTT CCC CCT GTG TTG GA
	Mb21d1_wt_rev	GTC CCA GGT GAC ACA ACA TC
	Mb21d1_mutant_rev	CGG ATG GAT GAA CAA ACA GA
Trex1 knockout *Expected bands:* *wt: 500 bp; mutant: 800 bp*	Trex_fwd	CGG GAT CCG ATG ACA ACC TGG CCA TCC TGC TCC GAG
	Trex_rev	CCT GCC ATT GCT GGG ACT TCC ATT G
	neo2	GTT TCG CTT GGT GGT CGA AT

2.4 Antibodies and staining chemicals

Antibody	**Label**	**Dilution**	**Manufacturer**	**Clone**
Anti-mouse IgG (goat)	FITC	1:500	Southern Biotech, Birmingham, USA	polyclonal
Anti-mouse Kappa, IC	BV421	1:100	Biolegend, San Diego, USA	RMK-45
Anti-mouse Kappa, SF	unconjugated	1:100	Biolegend	RMK-45
Anti-rat IgG2a	PE	1:100	Biolegend	MRG2a-83
Blimp1	AF647	1:100	Biolegend	5E7
Bst-2	eFlour 450	1:250	eBioscience, San Diego, USA	eBio927
Cardiac myosin heavy chain antibody	*ELISA standard*	n.a.	GeneTex, Irvine, USA	3-48
CD4	PE/Cy7	1:400	Biolegend	GK1.5
CD4	BV421	1:400	Biolegend	GK1.5

CD8a	PE	1:500	Life Technologies, Carlsbad, USA	5H10
CD8a	APC/Cy7	1:200	Biolegend	53-6.7
CD8a	BV421	1:400	Biolegend	53-6.7
CD11b	BV510	1:100	Biolegend	M1/70
CD11c	AF488	1:200	Biolegend	N418
CD11c	PE/Cy7	1:200	Biolegend	N418
CD19	PerCP/Cy5.5	1:400	Biolegend	6D5
CD19	PE/Cy7	1:400	Biolegend	6D5
CD19	AF647	1:200	Biolegend	6D5
CD25	AF647	1:200	Biolegend	PC61
CD26	PE	1:100	Biolegend	H194-112
CD44	AF488	1:200	Biolegend	IM7
CD44	APC/Cy7	1:200	Biolegend	IM7
CD45	APC/Cy7	1:400	Biolegend	30-F11
CD62L	APC/Cy7	1:250	Biolegend	MEL-14
CD86	PE	1:100	Biolegend	GL-1
CD86	FITC	1:200	Biolegend	GL-1
CD115	PE	1:200	Biolegend	AFS98
CD138	PE	1:400	Biolegend	281-2
CX3CR1	BV421	1:200	Biolegend	SA011F11
F4/80	Pacific Blue	1:400	Biolegend	BM8
FoxP3	PE	1:400	eBioscience	FJK-16S
I-A/I-E	AF488	1:400	Biolegend	M5/114.15.2
I-A/I-E	APC/Cy7	1:400	Biolegend	M5/114.15.2
IFNγ	BV421	1:200	Biolegend	XMG1.2
IκBα	PE	1:100	Cell Signaling, Frankfurt, Germany	L35A5
Ki67	AF488	1:500	Biolegend	16A8

Ki67	AF647	1:500	Biolegend	16A8
Ly6B.2	AF647	1:200	Bio-Rad AbD Sero–tec, Hercules, USA	7/4
Ly6G	PE/Cy7	1:200	Biolegend	1A8
Anti-MuLV gp70 env	unconjugated	1:50	Gift from Philipp Yu, Marburg, Germany	
NK1.1	PerCP/Cy5.5	1:250	Biolegend	PK136
PDC-Trem	PE	1:100	Biolegend	4A6
Phospho-IRF-3 (Ser396)	PE	1:50	New England Bio–labs, Ipswich, USA	D6O1M
Sca-1 (Ly6A/E)	PE/Cy7	1:100	Biolegend	D7
SiglecH	eFlour660	1:250	eBioscience	eBio440c
TCRß	BV421	1:100	Biolegend	H57-597
TCRß	BV510	1:100	Biolegend	H57-597
TCRß	PerCP/Cy5.5	1:250	Biolegend	H57-597
TNFalpha	PE	1:100	Biolegend	MP6-XT22
Ethidium Monoazide Bromide	504/600 nm	1:20,000	Biotium, Fremont, USA	-
Propidium Iodide	535/617 nm	1:10,000	Life Technologies	-
YO-PRO™-1 Iodide	491/509 nm	1:40,000	Invitrogen, Carlsbad, USA	-
BRW4	*ELISA standard*			
PL2-3	*Gift from Mark Shlomchik, Yale University, USA*			

2.5 Analytical chemicals, reagents, and kits

λ Protein phosphatase	New England Biolabs
100 bp-DNA ladder extended	Carl Roth, Karlsruhe, Germany
2-Propanol	AppliChem, Darmstadt, Germany
Anti-Nuclear Antibodies HEp-2 Kit	Orgentec, Mainz, Germany

Alkaline Phosphatase	New England Biolabs
AmpliTaq Gold 360 Master Mix and 360 GC Enhancer	Applied Biosystems / Thermo Fisher Scientific, Waltham, USA
BrdU	Invitrogen
Brefeldin A Solution (1,000X)	Biolegend
BSA	Carl Roth
Cardiac myosin protein (bovine)	Biozol Cytoskeleton, Denver, USA
Calf thymus DNA	Sigma Aldrich, Darmstadt, Germany
Calf thymus histones type II-A	Sigma Aldrich
CCL2 ELISA Kit	R&D Systems, Minneapolis, USA
cDNA Synthesis Kit	Bio-Rad
cGAMP ELISA Kit	Cayman Chemicals, Ann Arbor, USA
Chloroform	Merck, Darmstadt, Germany
Collagenase D	Roche, Basel, Switzerland
Cotrim K	Ratiopharm, Ulm, Germany
DNase I	Roche
PBS (Dulbecco's Phosphate-buffered Saline)	Gibco, Darmstadt, Germany
EDTA	AppliChem
Ethanol absolute	Carl Roth
FBS (Fetal Bovine Serum superior)	Merck
Fixation buffer	Biolegend
FoxP3 Staining Kit	Invitrogen
GelPilot Loading Dye, 5x	Qiagen, Hilden, Germany
Gentamycin	Merck
Goat anti-mouse IgG-AP (alkaline phosphatase)	Southern Biotech
Goat serum	Merck
HBSS	Gibco
Heparin	Rotexmedica, Trittau, Germany

HEPES	Lonza, Basel, Switzerland
Interferon-γ (Recombinant Mouse IFNγ)	Biolegend
Intracellular Staining Permeabilization Wash Buffer	Biolegend
Ionomycin	Sigma Aldrich
Isoflurane	Abbott, Chicago, USA
iTaq Universal SYBR Green Supermix	Bio-Rad
Lipopolysaccharide	Invivogen, San Diego, USA
Methanol	AppliChem
Mouse Cytokine Antibody Array I	RayBiotech Inc., Peachtree Corners, USA
Mouse serum	Invitrogen
NEBuffer for Protein MetalloPhosphatases	New England Biolabs
Permeabilization buffer	Biolegend
PFA (Paraformaldehyde)	AppliChem
PMA (Phorbol-12-myristat-13-acetat)	Sigma Aldrich
pNPP (p-Nitrophenyl phosphate buffer tablets)	Sigma Aldrich
Poly-L-Lysine	Sigma Aldrich
Proteinase K, recombinant	AppliChem
Quant-iT PicoGreen dsDNA Reagent	Invitrogen
QuantSeq 3'-mRNA-Seq Library Prep Kit (FWD)	Lexogen, Vienna, Austria
Rabbit serum	Invitrogen
Rat serum	Invitrogen
Red Blood Cell (RBC) Lysis Buffer	Biolegend
Revert Aid	Thermo Fisher Scientific
Roti-Safe GelStain	Carl Roth
RPMI 1640 Medium + GlutaMax	Gibco
S1 nuclease	Promega, Mannheim, Germany
Slides for immunohistochemistry	Matsunami, Bellingham, USA

Sodium acide	AppliChem
Sodium Metaperiodate	AppliChem
SPLIT RNA extraction kit	Lexogen
Tissue Tek	Sakura, Alphen aan den Rijn, Netherlands
Total RNA Purification Kit	Maxwell / Promega, Mannheim, Germany
Tris buffer	AppliChem
TruStain fcX	Biolegend
Trypan Blue	Gibco
Tween 20	AppliChem
Water, molecular grade	AppliChem
Yeast RNA	Sigma Aldrich

2.6 Solutions and buffers

2.5 % FBS RPMI	RPMI 1640 Medium + GlutaMax Supplement 2.5 % (v/v) FBS 1 % (w/v) HEPES 0.2 % (w/v) Gentamycin
Collagenase D digestion mix	HBSS 1 % (v/v) FBS 100 Mandl U / ml collagenase D 50 Kunitz U / ml DNase I
Digestion Buffer (for biopsy digestion)	50 mM Tris-HCl, pH 8 50 mM KCl 2.5 mM EDTA 0.45 % Igepal 0.45% (v/v) Tween-20
Fixation buffer	PBS 1% (w/v) PFA

Injection buffer	PBS 10 mM HEPES 0.2 % (w/v) Gentamycin
MACS buffer	PBS 5 mM EDTA 0.5 % (w/v) BSA 0.2 % (w/v) Gentamycin
Proteinase K solution	50 mM Tris-HCl, pH 8 25 mg Proteinase K 1 mM $CaCl_2$
RBC lysis buffer	10 x Biolegend RBC lysis buffer 1:10 diluted in ddH_2O
Staining medium (SM)	PBS 0.5 % (w/v) BSA 0.05 % (w/v) Sodium acide
Stimulation medium	RPMI 1640 Medium + GlutaMax Supplement 10 % (v/v) FBS 1 % (w/v) HEPES 0.2 % (w/v) Gentamycin
TAE buffer	40 mM Tris, pH 8.3 20 mM acetic acid 1 mM EDTA
TBS buffer	50 mM Tris-HCl, pH 7.5 150 mM NaCl
TE buffer	10 mM Tris-HCl, pH 8 1 mM EDTA

2.7 Consumables

24-well plates	Becton Dickinson, Franklin Lakes, USA

96-well plates for cell culture	TPP, Trasadingen, Swiss
96-well plates for staining	Ratiolab, Dreieich, Germany
96-well plates for qPCR	Nerbe Plus, Winsen, Germany
Cell strainer	Feinwerkstatt Bonn University, Germany
Coverslips	Marienfeld, Lauda-Königshofen, Germany
Counting chamber	Brand, Wertheim, Germany
Dishes	Greiner Bio-One, Kremsmünster, Austria
Injection syringes	Servoprax GmbH, Wesel, Germany
Other syringes	Braun, Kronberg, Germany
Microlon 600 96-well plates	Greiner Bio-One
Nitex Mesh, 70 µM	Klein & Wieler oHG, Königswinter, Germany
Reaction tubes (0.2, 0.5, 1.5, and 2 mL)	Sarstedt
Reaction tubes (15 and 50 mL)	Greiner Bio-One
Pipette tips (10, 200, and 1000 µL)	Starlab, Hamburg, Germany
Reaction tubes for flow cytometry	Sarstedt
Serological pipettes	Corning, New York, USA
Tissue embedding cassettes	Marienfeld, Lauda-Königshofen, Germany

2.8 Instruments and equipment

Confocal microscope	LSM 710 inverted	Zeiss, Oberkochen, Germany
ELISA reader	Infinite M200	TECAN, Männedorf, Swiss
Flow cytometer	Canto II	Becton Dickinson
Fluorescence-activated cell sorter (FACS)	Aria II	Becton Dickinson
Fluorescence microscope	Axio Observer	Zeiss
Gel imaging system	ChemiDoc XRS+	Bio-Rad
Hema-Vet	BC-5000	Mindray, Shenzhen, China

Microscope for plates	E-200	Nikon, Düsseldorf, Germany
Microscope for slides	TS-100	Nikon
Multichannel pipette	12-channel, 20-200 µl	Costar, New York, USA
PCR cycler	Mastercycler Pro	Eppendorf, Hamburg, Germany
Pipetting aid	Pipetboy acu 2	Integra, Zizers, Switzerland
qPCR cycler	realplex^2	Eppendorf
Sequencer	HiSeq 2500 v4	Illumina, San Diego, USA
Single channel pipettes	eppendorf Research	Eppendorf
Spectrophotometer	Nanodrop 2000	Peqlab, Erlangen, Germany
Ultrasound imaging system	Vevo 2100 Ultra High Frequency	FUJIFILM VisualSonics, Toronto, Canada
UV irradiation unit	UV 801 KL	Waldmann, Wheeling, USA
X-ray irradiator	RS-2000 Biological Irradiator	Radsource, Brentwood, USA

2.9 Software

BioRender	BioRender, Toronto, Canada
DeSeq2	Bioconductor
FlowJo v9	Becton Dickinson
Genomics Suite	Partek, St. Louis, USA
GraphPad Prism 6	Graphpad Software, LaJolla, USA
GSEA-P 2.0	Broad Institute, Cambridge, USA
Illustrator CS6	Adobe, Dublin, Ireland
ImageJ	National Institutes of Health, USA
Image Lab 6.1	Bio-Rad
Office 2018, Mac Version	Microsoft, Redmond, USA

3 Methods

3.1 Mouse genotyping

Mouse tail clips or ear punches were taken at the age of three weeks for all animals that had to be genotyped. 100 µl of Digestion Buffer containing 1.5 µl of proteinase K solution were added to the biopsy material and placed in a 56 °C water bath for overnight incubation. The samples were vortexed thoroughly until tissue was dissolved and subsequently heated to 95 °C for 10 min to inactivate proteinase K. Samples were frozen for at least 2 h at -80 °C. Afterwards, 1 µl of DNA-containing solution was subjected to genotyping PCR. Deletion or mutation of genes were confirmed using the respective primer pairs listed in section 2.3.

For genotyping PCR, AmpliTaq Gold 360 Mastermix was mixed with GC Enhancer as well as the appropriate amount of each primer to obtain a final primer concentration of 0.5 µM. The mix was filled up with ddH_2O to 11.5 µl, before adding 1 µl of DNA sample each. Amplification was performed on an Eppendorf Mastercycler Pro with thermal cycling conditions and primer melting temperatures adjusted according to the manufacturer's instructions.

For gel electrophoresis, gels were prepared by dissolving 1.5 % agarose in TAE buffer and subsequent microwave heating until bubbling. As gel staining reagent, 0.005 % Roti-Safe GelStain was added before curing of the gel. The PCR reaction was mixed with 1 µl of GelPilot Loading Dye and each sample was applied to one well of the gel. As a control, a 100 bp DNA-ladder was utilized. Gels were run at 140 V for 55 min.

3.2 Cell isolation from mouse organs and preparation of single-cell suspensions for flow cytometry

Spleens were removed, minced, and pressed through a metal strainer. After perfusion of mice with PBS, hearts and salivary glands were also removed, injected with Collagenase D digestion mix, minced with a scalpel and digested at 37 °C for 45 min. To obtain a single

cell suspension, the digested tissue pieces were pressed through a metal cell strainer using the plunger of a 2 ml syringe and filtered through a 70 µm Nitex nylon mesh before further use. To enhance the lymphocyte population and therefore extinguish vast amounts of erythrocytes present in the samples, cell suspensions were resuspended in 4 ml of RBC lysis buffer and incubated for 4 min at room temperature. To stop lysis, 5 ml of 2.5 % FBS RPMI was added to each sample before centrifugation at 500 rcf for 5 min. Cells were washed twice in staining medium (SM) and resuspended in an appropriate amount of 2.5 % FBS RPMI.

3.3 Preparation of bone marrow for transplantation

Both femurs of bone marrow donors were removed and cut at both ends under sterile conditions. Bones were flushed with 3 ml of fresh MACS buffer and cells were filtered through a 70 µm mesh filter. After centrifugation at 500 rcf for 10 min at 8 °C, cell pellets were treated with sterile RBC lysis buffer for 1 min. Lysis was stopped with MACS buffer and cells were washed once. After counting, cell suspension was adjusted to $1x10^7$ cells / 0.2 ml in injection buffer and kept on ice for subsequent i.v. injection.

3.4 Preparation of mouse serum from fresh blood samples

Whole blood samples were collected from the vena cava posterior and transferred to a 1.5 ml tube. The blood was left at room temperature for 15-30 min for clotting. For serum separation the samples were centrifuged at 1500 rcf for 8 min and the supernatant was carefully removed and transferred to a new tube. Serum samples were stored at -80 °C until further use.

3.5 Irradiation and transplantation of bone marrow recipient mice

Mice were irradiated with a dosage of 5.5 Gy (0.037 Gy/s for a duration time of 149 s) twice with 4 h resting time in between. Bone marrow transplantation was performed 8 h after

the second irradiation using a 27 G needle intravenously. For every mouse, $1x10^7$ cells in 200 µl injection buffer were used. Mice received antibiotic treatment with 1 mg / ml Co–trim K in the drinking water for 3 weeks following the transplantation procedure. Analyses were performed 12 weeks after transplantation.

3.6 Flow cytometry surface staining

Surface staining was performed on ice in PBS containing 0.5 % (w/v) BSA and 0.05 % (w/v) sodium acide. Intracellular staining was carried out using the Biolegend Fixation buffer and the Biolegend Permeabilization buffer, or the Invitrogen FoxP3 Staining Kit for Ki67 and FoxP3 staining. For intracellular cytokine staining, $1x10^7$ splenocytes were stimulated for 5 h at 37 °C with 750 ng / mL ionomycin and 20 ng / mL PMA in stimulation medium. After 1 h of stimulation, 5 mg / mL brefeldin A was added to the cultures. For exclusion of dead cells in subsequent staining, ethidium monoazide bromide (EMA) was used. In order to stain specifically for cell death, unfixed cells were stained with Yo-Pro1 and immediately measured. Stained cells were analyzed on a FACSCanto II or subjected to sorting on a FACSAria II.

3.7 Phosflow

To determine the endogenous phosphorylation state of IRF-3 (Ser396), spleen cells were instantly fixed with 1 % (w/v) PFA in RPMI containing 5 % (v/v) FCS at RT while pressing the organ through a strainer to generate a single cell suspension. After 15 min incubation at RT, cells were transferred to 15 ml tubes through 70 µm Nitex nylon mesh, washed once with 10 ml of RPMI containing 5 % FBS at 500 rcf for 5 min at 8 °C followed by incubation with 2 ml ddH_2O for 2 min. Cells were centrifuged again, resuspended in 500 µl of RPMI containing 5 % FCS, and transferred to a 96-well plate for subsequent staining. 50 µl of the respective antibody dilution in SM were added and incubated for 15 min on ice, followed by two washing steps. For cell permeabilization, samples were incubated with 90 µl of ice-cold methanol for 30 min on ice. Since cells shrink due to methanol permeabilization,

following centrifugation steps were conducted at 800 rcf. Cells were washed twice with TBS and each sample was divided to obtain a negative control for dephosphorylated cell fluorescence. For dephosphorylation, control samples were incubated for 30 min at 37 °C with 250 U gamma phosphatase present in 30 µl NEBuffer for Protein MetalloPhosphatases with 1 mM $MnCl_2$. After washing, all samples were blocked with Biolegend TruStain fcX and 10 % (v/v) rabbit serum in PBS. Incubation with Phospho-IRF-3 (Ser396) rabbit monoclonal Antibody (PE conjugate) and antibodies against surface markers in TBS with 1 % BSA (w/v) was carried out over night at 4 °C.

3.8 Intracellular staining for endogenous retroviruses

In order to stain intracellularly for endogenous retroviruses, an antibody against murine leukemia virus (MuLV) envelope glycoprotein 70 (gp70 env) was used. After fixation in Biolegend fixation buffer, cells were permeabilized in Biolegend permeabilization buffer and labeled with rat-anti-MuLV gp70 env for 30 min. Following to a 10 min block with mouse serum, for further detection, cells were stained with a secondary fluorophore-coupled anti-rat IgG antibody for 1 hr. Prior to subsequent surface staining, to prevent cross-contermination, cells were blocked with 10 % (v/v) rat serum in PBS for 10 min.

3.9 ELISAs and Cytokine arrays

Serum **anti-nucleosome IgG** concentrations were determined by ELISA. 96-well polystyrene plates were coated with poly-L-lysine and incubated with S1 nuclease-pre-treated dsDNA, phenol-extracted from calf thymus (Sigma-Aldrich) for 1 h at RT. Afterwards, 10 µg / mL calf thymus histones type II-A were added for another hour. After blocking with 1 % (w/v) BSA in PBS to prevent unspecific binding, serial dilutions of sera from 1:50 to 1:1350 were added to each well. The nucleosome-specific antibody clone PL2-3 was used as a standard.[68] Plates were washed and blocked with 1 % (v/v) goat serum in PBS for 1 h at RT in order to prevent unspecific binding of the secondary goat antibody. Specific antibodies were detected with 40 µL of goat anti-mouse IgG-AP (alkaline phosphatase) and

40 µL of pNPP solution as substrate. Optical density was measured at 405 / 630 nm wavelength.

For the **anti-cardiac myosin IgG** ELISA, polysterene plates were coated with 10 µg / mL bovine cardiac myosin protein in PBS without BSA. After blocking with 1 % (w/v) BSA in PBS for 2 h, sera were applied in serial dilutions from 1:50 to 1:1350 and specific antibodies were detected by goat anti-mouse IgG-AP (as described above). For quantification, absorbance at 405/630 nm was compared to an anti-cardiac myosin heavy chain antibody standard, clone 3-48.

Accordingly, to elucidate concentrations of **anti-RNA IgG** in serum, ELISA plates were coated with 10 µg/mL poly-L-lysine and incubated overnight before application of yeast RNA (15 µg/mL) in PBS, serving as antigen for potential anti-RNA antibodies.[69] After blocking with 1 % (w/v) BSA in PBS for 2 h, the mouse sera were added in serial dilutions from 1:50 to 1:1350 for 2 h and detected with goat anti-mouse IgG-AP as described before. BWR4 antibody was used as standard.

The Mouse Cytokine Array C1 (RayBiotech) was performed according to the manufacturer's protocol. Briefly, membranes were blocked with the provided blocking buffer for 30 min and subsequently incubated with 1 ml of a 1:100 serum sample dilution overnight at 4 °C. After a washing step with the provided Wash Buffers I and II, 1 ml of the supplied antibody cocktail was added to the membranes for 2 h at RT, followed by another washing step. Lastly, 2 ml of the kit-included horseradish-peroxidase-streptavidin solution was applied for another 2 h before chemiluminescence detection via the supplied detection buffer, consisting of a 1:1 mixture of Detection Buffer C and Detection Buffer D. Imaging was performed on a ChemiDoc XRS+ Imaging System with an exposure time of 95 s.

3.10 Anti-nuclear antibody (ANA) detection assay

Anti-nuclear IgG antibodies (ANAs) serve as markers for the diagnostic of several autoimmune diseases. For the detection of ANAs in mouse serum, the anti-nuclear antibodies HEp-2 Kit from Orgentec was employed according to the manufacturer's protocol. The HEp-2 cell line features large cells with a high mitosis rate, which makes it

suitable for the detection of fluorescently labeled ANAs via fluorescence microscopy. Slides are delivered with HEp-2 cells readily attached to them. Mouse sera were diluted 1:50 with PBS and added to each well on the slide, along with a negative control (C57Bl/6) and a positive control (MRL.*Fas*^{lpr}). After incubation and washing, a FITC-conjugated goat-anti-mouse IgG was applied and samples were analyzed using a 400 x magnification.

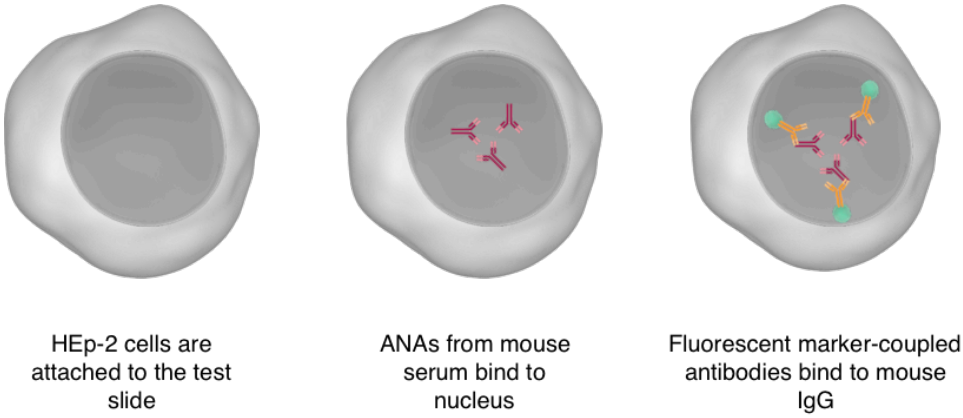

Figure 2. Schematic of ANA detection on HEp-2 cells. Anti-nuclear antibodies potentially present in mouse sera bind to the nucleus of HEp-2 cells attached to a test slide. Antibodies reactive against mouse IgG, which are labeled with fluorescent markers allow for subsequent quantitative detection by utilizing fluorescence microscopy.

3.11 Measurement of free serum DNA

Serum samples were diluted 1:10 in TE buffer. The appropriate amount of Quant-iT PicoGreen reagent was added and the samples were incubated 5 min at RT, protected from light. Fluorescence was measured using standard fluorescein wavelength (excitation at 480 nm, emission at 520 nm).

3.12 3'-mRNA sequencing

For 3'-mRNA sequencing, mRNA was extracted from spleen tissue using the SPLIT RNA Extraction Kit (Lexogen). Sequencing was performed with 200 ng of mRNA per library on a HiSeq 2500 v4 machine with 1 x 50 bp, single read, employing the Lexogen QuantSeq 3'-mRNA-Seq Library Prep Kit (FWD).

3.12.1 Differential expression analysis

Pre-processing of RNA-Seq data was performed using the Partek® Genomics Suite® (PGS, build 8.0.19.0819). Briefly, adapter-trimmed raw reads were uploaded to PGS, trimmed for a Phred quality score > 20 and aligned to the mouse reference genome mm10 by STAR (version 2.6.1) with slightly modified standard settings (max mismatches = 14) as recommended by Lexogen®.[70] For mRNA quantification mm10 Ensembl transcripts (release 98) were used as annotation files. Afterwards, raw gene counts were normalized and differentially expressed genes (defined by p value < 0.05) identified by the DESeq2 (package version 1.25.16) algorithm in R.[71] Heatmaps and several plots were generated using the ggplot2 library. Principal component analysis was performed using the ggbiplot library. For gene set enrichment analysis (GSEA) a pre-ranked list was generated based on a metric score calculated by: $log_2(fold\ change)\ x\ (-log_{10}(pvalue))$ and applied to the GSEA java desktop application provided by the Broad Institute.[72]

3.13 qPCR on genomic DNA

To analyze the genetic composition of bone marrow transplanted mice, genomic DNA was extracted from FACS purified cells and used as template. PCR was performed using the iTaq Universal SYBR Green Supermix on a realplex2 cycler.

3.14 UV stimulation

In order to induce dermatitis, 12 weeks after bone marrow transplantation mice were shaved on the back and subjected to UV irradiation on 3 consecutive days with 450 mJ/cm^2 of UVB per day using the UV 801 KL system, equipped with UV21 UVB lamps. Skin biopsy samples were taken after sacrificing the animals on day 12 after start of UV exposure.

3.15 Histology

Tongues and hearts were formalin fixed, embedded in paraffin, sectioned, and stained with hematoxylin and eosin (H&E) in the laboratory of Prof. Peter Boor, Aachen. Organ inflammation was scored in a blinded fashion from 0 to 3 and 0 to 4, respectively, where 0 is no inflammation, 1 depicts slight inflammation with few scattered infiltrates, 2 is medium inflammation characterized by several scattered infiltrates and less than 3 large infiltrates, and 3 represents extensive inflammation with many scattered infiltrates and 3 or more large infiltrates.

3.16 Echocardiography

For echocardiography, each mouse was anesthetized in a closed chamber with 1.5 % (v/v) isoflurane in oxygen for approximately 5 min until immobilized. The mouse was removed from the chamber, taped to a heating plate at 37 °C, and anesthesia was perpetuated by usage of a nose cone connected to an anesthesia machine, supplying 2 % (v/v) isoflurane in oxygen. Electrocardiogram, respiratory rate and body temperature were monitored continuously. Hair removal lotion was applied to the chest to completely depilate the hair for improved image quality. For functional analysis, a Fujifilm Visualsonics Vevo 2100 Ultra High Frequency Imaging Platform was used. Left ventricular ejection fraction, fractional shortening, ventricular volumes, and wall diameters were measured in parasternal short-axis M-modes.

4 Results

4.1 cGAMP-mediated bystander cell activation induces innate immune activation and tissue inflammation in TREX1 deficiency

To determine the contribution of cGAMP-mediated bystander activation to the development of *Trex1*$^{-/-}$-associated autoimmunity, a bone marrow transplantation approach was used (Fig. 3a). Specifically, mice double-deficient for TREX1 and STING, a downstream mediator of cGAS (*Trex1*$^{-/-}$*;Tmem173*$^{gt/gt}$, hereafter called dKO) were lethally irradiated and reconstituted with bone marrow (BM) from either cGAS deficient mice (*Mb21d1*$^{-/-}$ BM), TREX1 and STING double-deficient mice (dKO BM), or a 50:50 mixture of cells from both strains (*Mb21d1*$^{-/-}$ + dKO BM). In dKO cells unmetabolized cytosolic DNA is sensed by cGAS. The resulting cGAMP, however, does not lead to cell-intrinsic immune activation due to the lack of STING, but can be shuttled to neighboring *Mb21d1*$^{-/-}$ cells, which have a functional STING (Fig. 3b). In *Mb21d1*$^{-/-}$ BM mice cGAMP is only produced by non-hematopoietic radioresistant cells (such as epithelial cells and fibroblasts) and few hematopoietic radioresistant cells (such as a subset of Kupffer cells and alveolar macrophages). In contrast, cGAMP in *Mb21d1*$^{-/-}$ + dKO BM mice can additionally be generated by half of the transplanted hematopoietic cells. This strategy allowed to unequivocally determine the pathophysiological relevance of immune cell activation by cGAMP transmission.

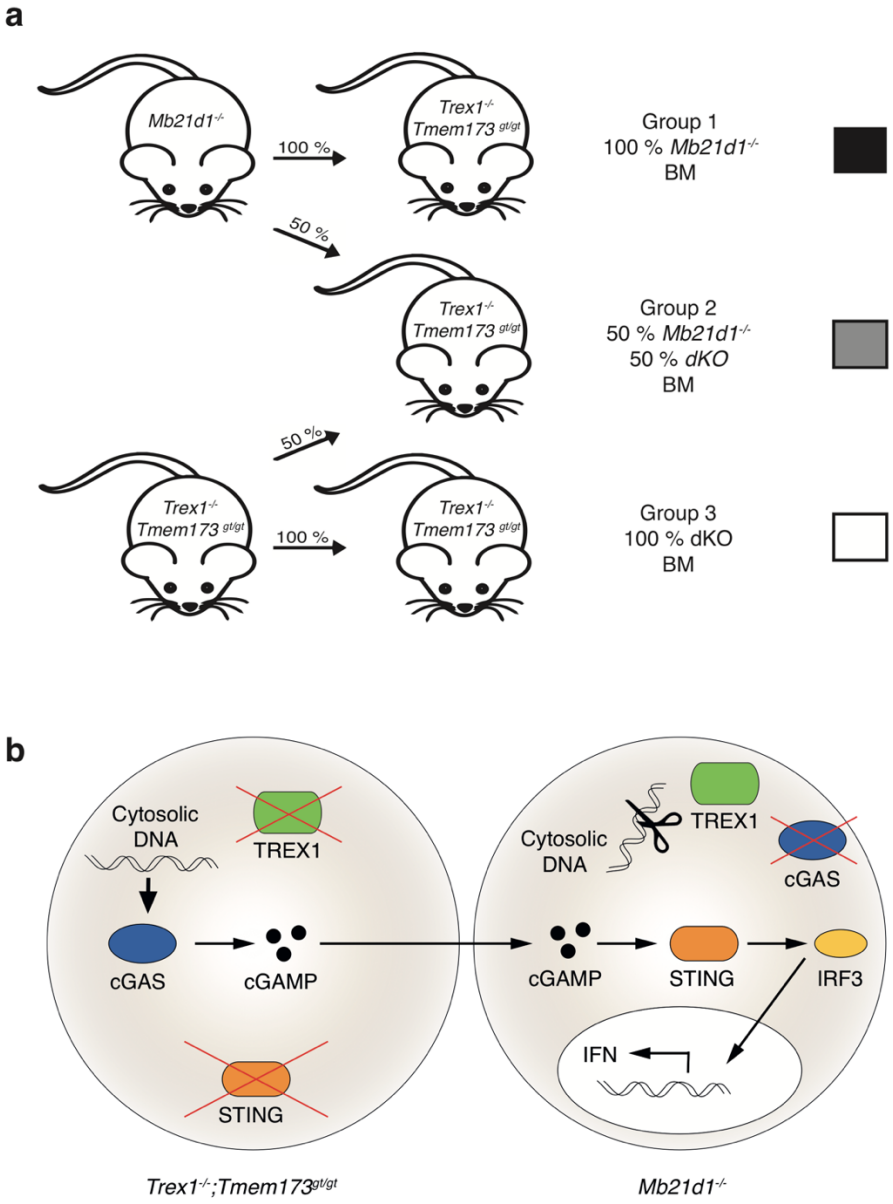

Figure 3: Schematic of bone marrow transplantation experiments. (a) Lethally irradiated *Trex1*$^{-/-}$;*Tmem173*$^{gt/gt}$ (dKO) mice received bone marrow from *Mb21d1*$^{-/-}$ or dKO donor mice for group 1 and 3, respectively. For group 2, recipients were transplanted with a mix of bone marrow from both types of donors. **(b)** Schematic of cGAMP transfer to bystander cells. Cells lacking TREX1 accumulate cytosolic DNA which, upon recognition by cGAS, lead to subsequent cGAMP production. Since STING (encoded by *Tmem173*) is also absent in these cells, cGAMP can be transferred to neighboring cells, unable to sense DNA due to cGAS (*Mb21d1*) knockout, via gap junctions and hypothetically trigger cytokine production.

4.1.1 Cell-extrinsic cGAMP activates the IRF3 pathway in cDCs

In a first step, I assessed whether there was any selective pressure favoring the survival of *Mb21d1*$^{-/-}$ or dKO cells in *Mb21d1*$^{-/-}$ + dKO BM mice. Across all examined immune cell subsets sorted from spleens 12 weeks after transplantation, in *Mb21d1*$^{-/-}$ + dKO BM mice deletion of *Mb21d1* was 45-54 % (Table 1) as determined by qRT-PCR. Thus, the genetic composition was virtually the same as in the BM mixture used for transplantation, revealing that neither *Mb21d1*$^{-/-}$ nor dKO cells had a competitive advantage over each other.

Group	Cell population	Deletion (%)
Mb21d1$^{-/-}$ BM	B cells	99.1
Mb21d1$^{-/-}$ + dKO BM		54.6
dKO BM		0.00
Mb21d1$^{-/-}$ BM	cDCs	99.0
Mb21d1$^{-/-}$ + dKO BM		46.2
dKO BM		0.00
Mb21d1$^{-/-}$ BM	macrophages	92.8
Mb21d1$^{-/-}$ + dKO BM		49.8
dKO BM		0.00
Mb21d1$^{-/-}$ BM	T cells	85.5
Mb21d1$^{-/-}$ + dKO BM		45.4
dKO BM		0.00

Table 1. Deletion of Mb21d1 in BM transplant models. Deletion efficacy of *Mb21d1* in various cell types isolated from spleens was determined by measuring the amount of residual *Mb21d1* by qPCR. The amount of *Mb21d1* in each sample was normalized to the unaffected gene *Ccr2*. Cell populations were sorted by flow cytometry using the respective population-specific surface markers: T cells (TCRß$^{+}$CD19^{-}), B cells (CD19^{+}TCRß$^{-}$), cDCs (CD11c^{hi}MHC-II^{+}CD19^{-}), red pulp macrophages (CD11b^{+}F4/80^{+}CD11c^{-}).

Autoimmunity in TREX1 deficiency depends on the induction of type I IFN by the transcription factor IRF3 together with its transcriptional co-activator CBP/p300.[73,74] Therefore, phosphorylation of IRF3 has been used as readout for cGAMP shuttling and subsequent STING activation. Phosflow was utilized to determine the native phosphorylation state of IRF3 directly *ex vivo*. Type 1 and 2 cDCs (cDC1s, cDC2s) in *Mb21d1*$^{-/-}$ BM and *Mb21d1*$^{-/-}$ + dKO BM demonstrated substantially elevated basal amounts of p-IRF3 (Ser396) when compared to their counterparts in dKO BM mice (Fig. 4). The

increase was more pronounced in cDCs from *Mb21d1*$^{-/-}$ BM than in those from *Mb21d1*$^{-/-}$ + dKO BM mice, likely reflecting the twice as high frequency of cGAMP-responsive *Mb21d1*$^{-/-}$ cells. These results indicate that cGAMP is delivered from dKO cells to *Mb21d1*$^{-/-}$ cDCs where it initiates IRF3 signaling. Interestingly, cGAMP derived from radioresistant cells was sufficient to elicit this response. In conclusion, traveling of cGAMP presumably mediates the activation of bystander cDCs *in vivo* in the context of autoimmunity.

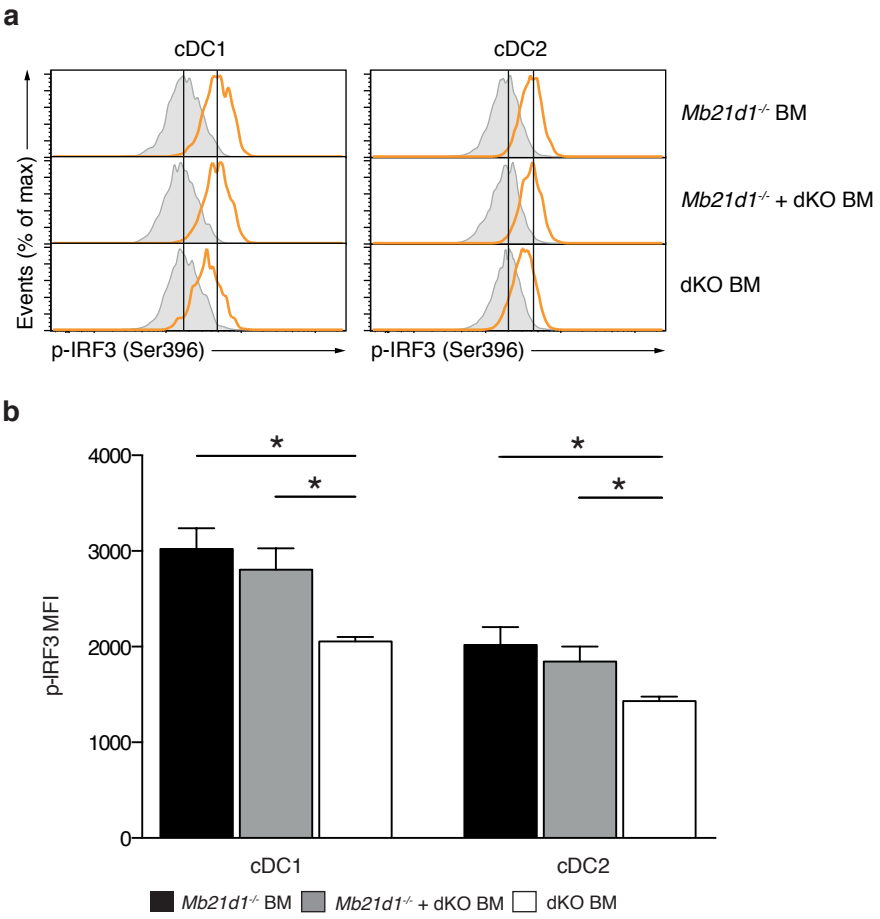

Figure 4. Cell-extrinsic cGAMP activates the IRF3 pathway in DCs. (a) Spontaneous signaling in splenic cDCs. Histograms display representative results for p-IRF3 (Ser396) of gated cDCs in instantly fixed spleens. Each histogram shows an overlay of λ protein phosphatase-treated (grey shaded) and untreated (colored) cells. **(b)** Mean fluorescence intensity (MFI) for p-IRF3 in cDCs from instantly fixed spleens (n = 5 mice for *Mb21d1*$^{-/-}$ BM; n = 4 mice for *Mb21d1*$^{-/-}$ + dKO and dKO BM). Data are represented as mean + SEM. Statistics were calculated by two-tailed Mann-Whitney U Test with *p < 0.05. Experiments in (a-b) were performed twice and data are representative of a single experiment.

4.1.2 Delivery of cGAMP from radioresistant cells to immune cells induces tonic IFN and NF-κB signaling in TREX1 deficiency

To test whether IRF3 activation resulting from cGAMP transmission provoked functional activation of immune cells, global transcriptional analysis was conducted. Given that the greatest difference in p-IRF3 was observed between *Mb21d1*$^{-/-}$ BM and dKO BM mice, 3'-mRNA sequencing of splenocytes from these animals was performed. Unsupervised hierarchical clustering of the most variable genes (Fig. 5a) and principal component analysis (Fig. 5b) demonstrated that intercellular cGAMP travel led to differential expression in 684 genes (non-adjusted p value < 0.05). Importantly, *Trex1* was found to be significantly upregulated in *Mb21d1*$^{-/-}$ BM mice and *Mb21d1* to be significantly upregulated in dKO BM mice confirming the validity of the analysis (Fig. 5c).

To better define how cGAMP travel shapes gene transcription it was investigated which Hallmark gene sets were enriched in *Mb21d1*$^{-/-}$ BM compared to dKO BM mice (Fig. 5d). Genes upregulated in *Mb21d1*$^{-/-}$ BM mice were associated with IFN-α and IFN-γ, which induce largely overlapping gene sets, and NF-κB signaling, consistent with STING activation in these mice.

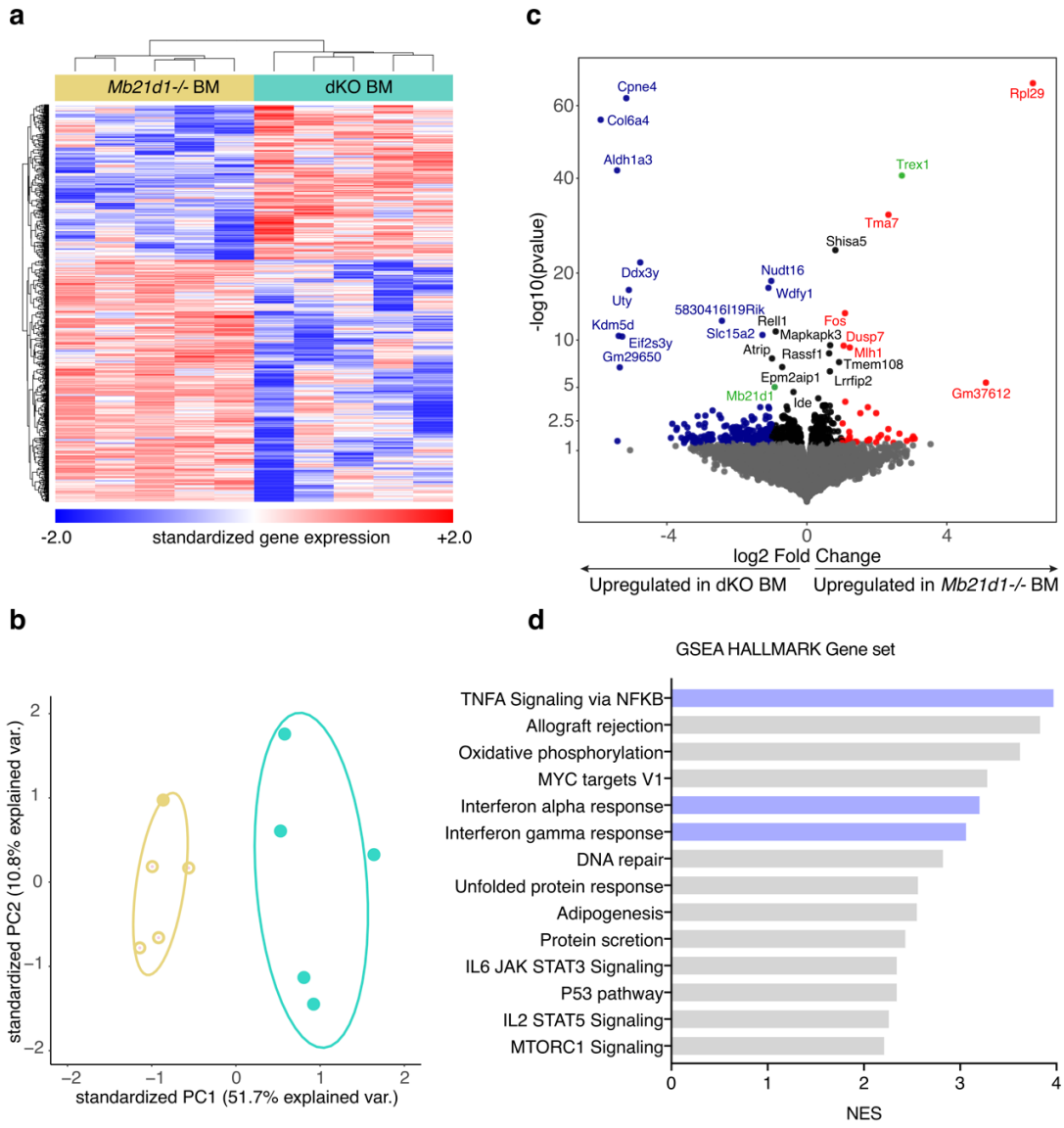

Figure 5. Intercellular shuttling of cGAMP induces IFN and NF-κB signaling in Trex1 deficiency. Global gene expression analysis by 3'-RNA-seq. **(a)** Gene and sample wise hierarchical clustering based on differentially expressed genes (non-adjusted p value < 0.05, n = 684) within the dataset of spleen tissue from *Mb21d1*$^{-/-}$ BM and dKO BM mice. Gene expression values are Z score standardized. For visualization purposes Z scores were limited to numbers between -2 and 2. **(b)** PCA plot of spleen tissue data from *Mb21d1*$^{-/-}$ BM and dKO BM mice. PCA is based on differentially expressed genes (non-adjusted p value <0.05, n = 684). **(c)** Volcano plot indicating transcriptomic changes between *Mb21d1*$^{-/-}$ BM and dKO BM mice. Genes with a non-adjusted p value < 0.05 and a signed fold change > 2 are colored in red (upregulated in *Mb21d1*$^{-/-}$ KO BM mice) and blue (upregulated in dKO BM mice). Differentially expressed genes with an adjusted p-value < 0.05 are labeled. **(d)** Normalized Enrichment Scores (NES) of Hallmark gene sets significantly upregulated (false discovery rate q value < 0.01) in *Mb21d1*$^{-/-}$ BM mice compared to dKO BM mice in a pre-ranked Gene Set Enrichment Analysis (GSEA) based on a metric score calculated by $\log_2$(fold change) x (-$\log_{10}$(p value)). n = 5 mice per group.

To verify NF-κB activation and determine the precise cell subgroups in which it is occurring, NF-κB signaling events such as IκBα degradation and RelA phosphorylation were evaluated by flow cytometry. The frequency of cells with high IκBα expression among classical monocytes and red pulp macrophages was substantially lower in *Mb21d1*$^{-/-}$ BM than in dKO BM mice (Fig. 6), indicating that cGAMP transmission initiates NF-κB

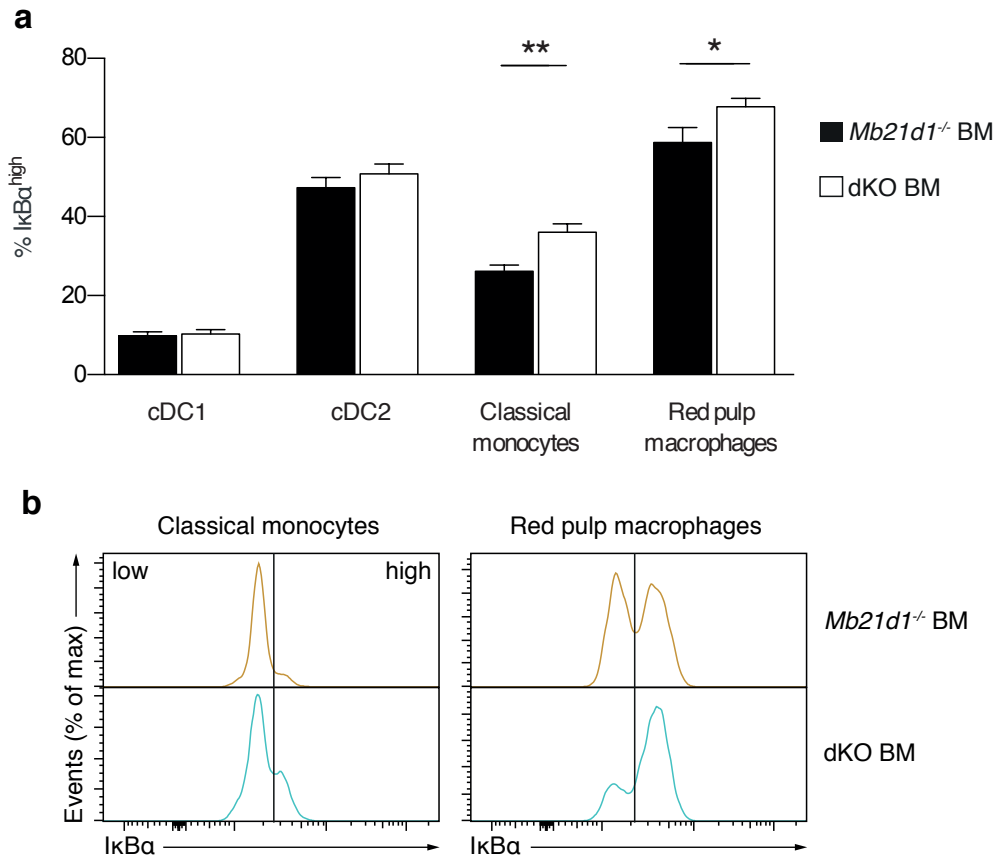

Figure 6. cGAMP transfer causes NF-κB activation due to upregulation of IκB in classical monocytes and red pulp macrophages. (a) Percentage of splenic cDCls, cDC2s, classical monocytes, and red pulp macrophages with high expression of IκBα (n = 7 for *Mb21d1*$^{-/-}$ BM mice, n = 6 for dKO BM mice) **(b)** Histograms display representative results for IκBα staining of gated T cells. Data in bar graphs are represented as mean + SEM. Statistics were calculated by two-tailed Mann-Whitney U test, *p < 0.05; **p < 0.01. Data are pooled from 2 independent experiments.

signaling. In line with this, also basal RelA (p536) phosphorylation was increased in classical monocytes and red pulp macrophages in *Mb21d1*$^{-/-}$ BM compared to dKO mice (Fig. 7). Notably, there were no significant differences observed among cDCs.

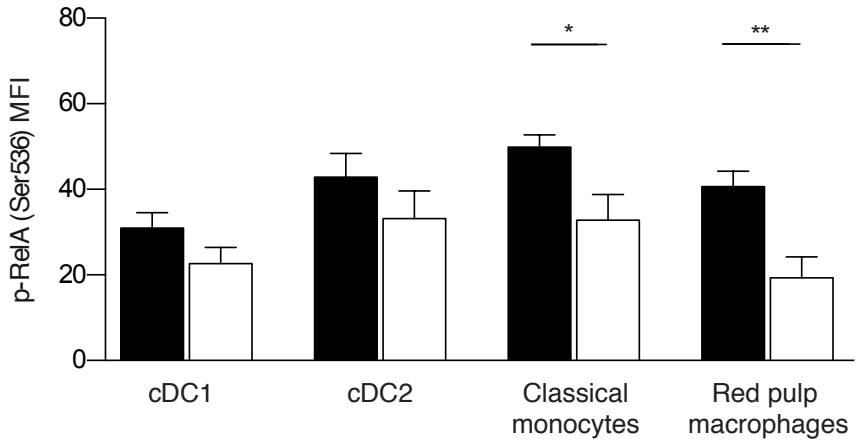

Figure 7. NF-κB signaling is initiated by cGAMP transmission via phosphorylation of RelA (p536). Mean fluorescence intensity (MFI) for p-RelA in dendritic cells (cDC1 and cDC2), classical monocytes, and red pulp macrophages from instantly fixed spleens (n = 7 for *Mb21d1*$^{-/-}$ BM mice, n = 6 for dKO BM mice) Data represented as mean + SEM. Statistics were calculated by two-tailed Mann-Whitney U Test with *p < 0.05; **p < 0.01.

Since differences in NF-κB signaling were detected, I next assessed whether this translated into altered cytokine levels. Therefore, the relative expression of cytokine proteins in the serum in *Mb21d1*$^{-/-}$ BM and dKO BM mice was also determined by utilizing the Cytokine Array C1 (RayBiotech), but no obvious differences could be detected (Fig. 8). Taken together, these data support the notion that cGAMP-mediated bystander activation leads to constitutive IFN and NF-κB signaling in TREX1 deficiency.

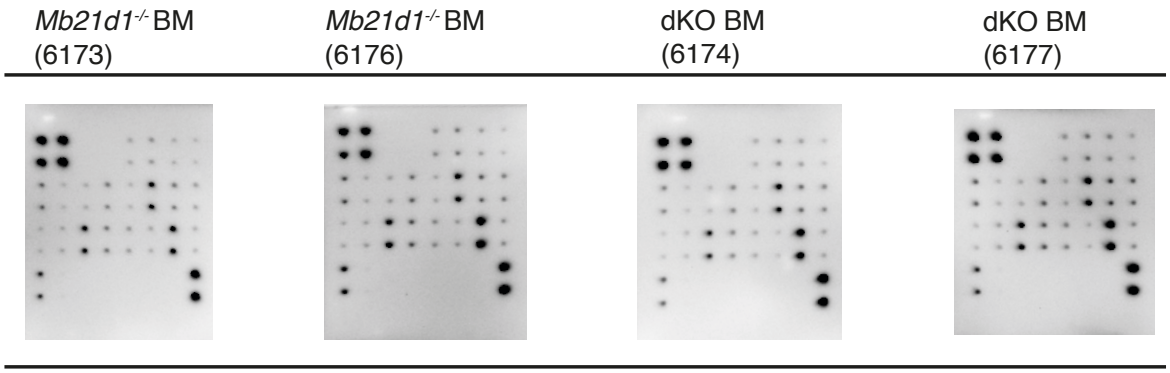

	A	B	C	D	E	F	G	H
1	Pos	Pos	Neg	Neg	GCSF	GM-CSF	IL-2	IL-3
2								
3	IL-4	IL-5	IL-6	IL-9	IL-10	IL-12 p40/p70	IL-12 p70	IL-13
4								
5	IL-17A	IFNγ	MCP-1 (CCL2)	MCP-5	RANTES (CCL5)	SCF	TNF RI	TNFα
6								
7	TPO	VEGF-A	Blank	Blank	Blank	Blank	Blank	Pos
8								

Figure 8. cGAMP transfer does not result in different cytokine expression profile. Cytokine array membranes for two representative *Mb21d1*$^{-/-}$ BM and dKO BM transplanted mice. Dots represent cytokines corresponding to the table on the right in duplicates.

4.1.3 cGAMP transfer promotes T cell accumulation in lymphoid tissue but not T cell priming

Elucidating the contributions of intercellular cGAMP travel to the spontaneous self-directed T cell response in TREX1 deficiency was the next step. $CD4^+$ and $CD8^+$ T cell numbers in spleens were considerably higher in *Mb21d1*$^{-/-}$ BM and *Mb21d1*$^{-/-}$ + dKO BM mice than in dKO mice (Fig. 9a), indicating that cGAMP transmission facilitates T cell accumulation.

Expression of stem cell antigen 1 (Sca-1) on lymphocytes is associated with persistent IFN signaling . Consistent with the finding that cGAMP transmission induces an IFN gene

signature, Sca-1 protein expression was increased in T cells from *Mb21d1*$^{-/-}$ BM and *Mb21d1*$^{-/-}$ + dKO BM compared to those from dKO BM controls (Figs. 9b and 9c).

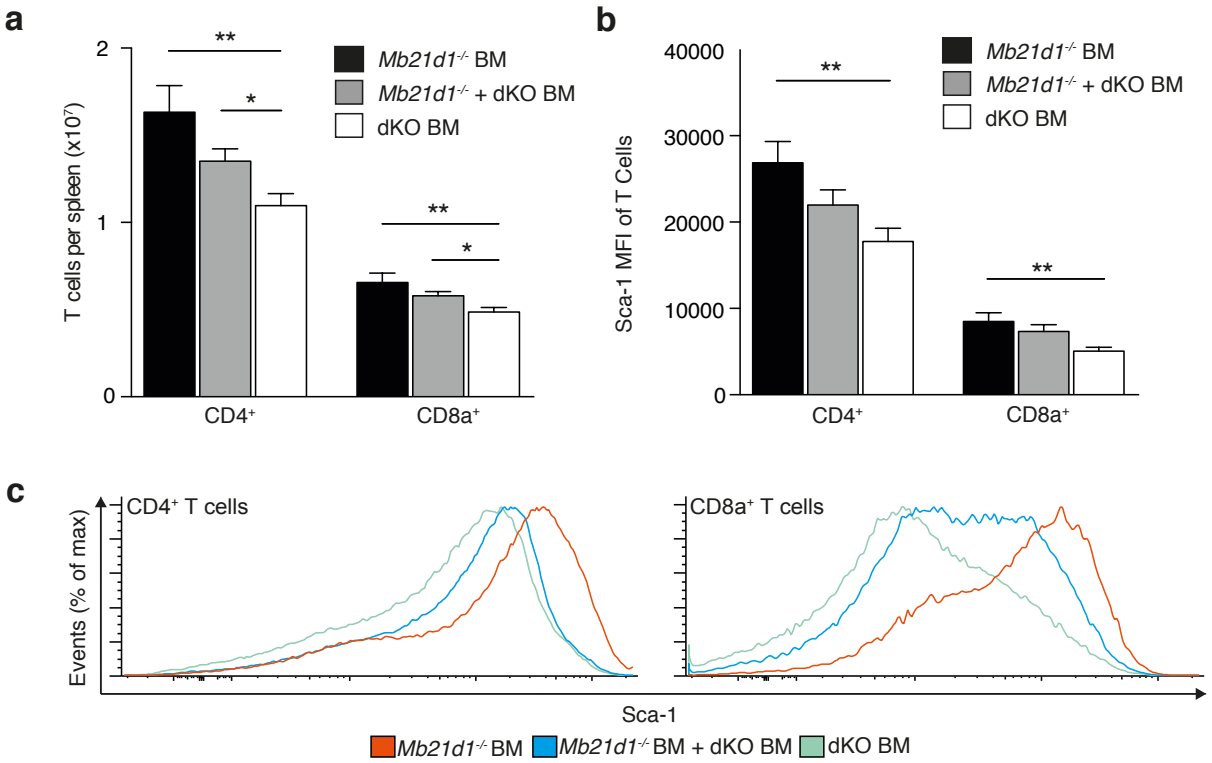

Figure 9. cGAMP transfer promotes T cell accumulation in lymphoid tissue. (a) Number of CD4$^+$ and CD8$^+$ T cells in spleens from *Mb21d1*$^{-/-}$ BM (n = 14), *Mb21d1*$^{-/-}$ + dKO BM (n = 14) and dKO BM mice (n = 16). **(b)** Mean fluorescence intensity (MFI) for Sca-1 of splenic CD4$^+$ and CD8a$^+$ T cells in *Mb21d1*$^{-/-}$ BM (n = 7), *Mb21d1*$^{-/-}$ + dKO BM (n = 7) and dKO BM mice (n = 6). **(c)** Representative Sca-1 staining histograms of splenic CD4$^+$ and, CD8a$^+$ T cells. Bar graphs show mean + SEM. Statistics were calculated by two-tailed Mann-Whitney U Test with *p < 0.05, **p < 0.01. Data are pooled from 4 (a) or 2 (b, c) independent experiments.

However, cGAMP delivery to bystander cells did not promote T cell activation. There was no appreciable difference in the frequency of phenotypically naïve CD4$^+$ and CD8$^+$ T cells in any of the three groups of mice (Fig. 10a). In addition, no differences were observed in the frequency of regulatory Foxp3$^+$CD25$^+$CD4$^+$ T cells (Fig. 10b).

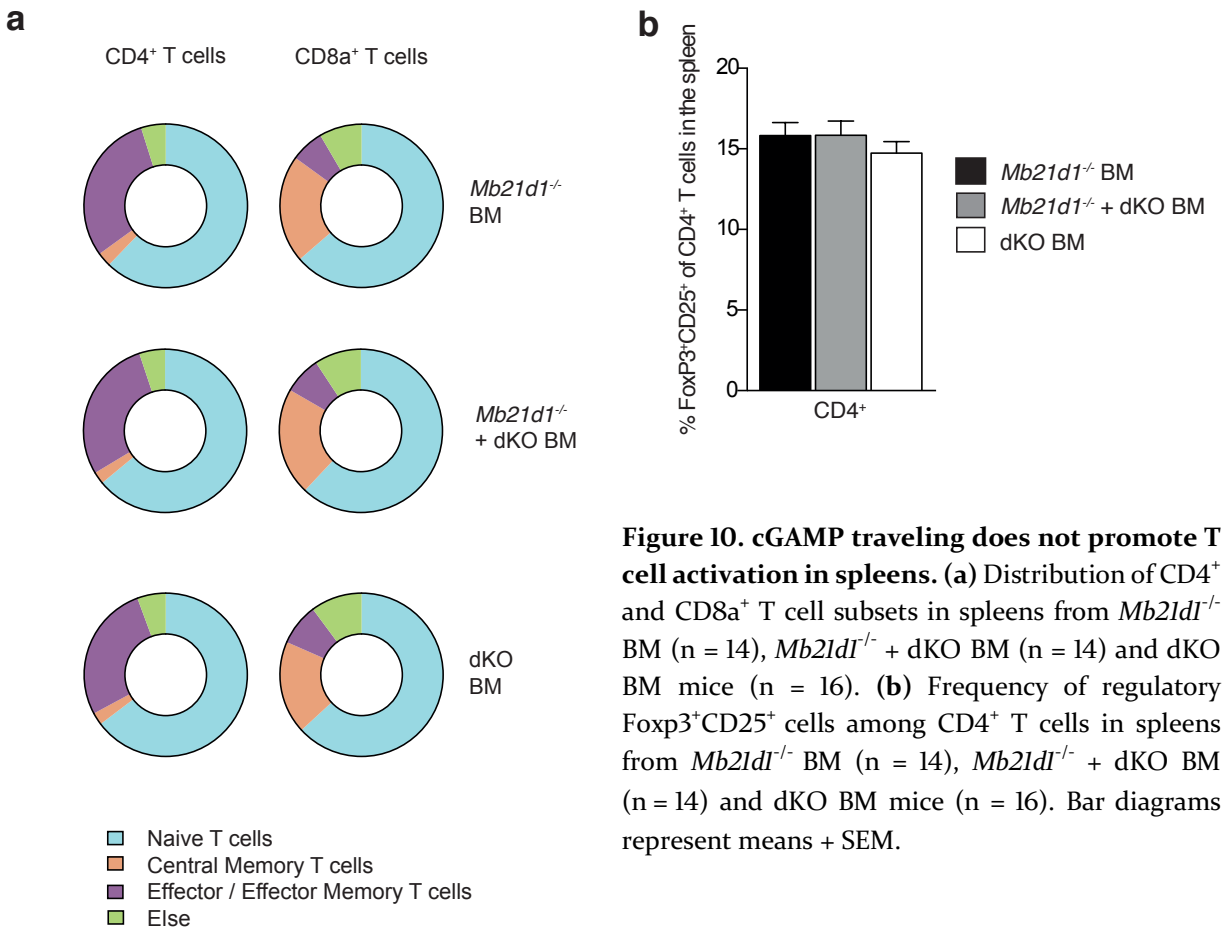

Figure 10. cGAMP traveling does not promote T cell activation in spleens. (a) Distribution of $CD4^+$ and $CD8a^+$ T cell subsets in spleens from *Mb21d1*$^{-/-}$ BM (n = 14), *Mb21d1*$^{-/-}$ + dKO BM (n = 14) and dKO BM mice (n = 16). **(b)** Frequency of regulatory $Foxp3^+CD25^+$ cells among $CD4^+$ T cells in spleens from *Mb21d1*$^{-/-}$ BM (n = 14), *Mb21d1*$^{-/-}$ + dKO BM (n = 14) and dKO BM mice (n = 16). Bar diagrams represent means + SEM.

To determine whether the spread of cGAMP promotes polarization of $CD4^+$ and/or $CD8^+$ T cells into IFN-γ and TNF-α producing effectors, splenocytes were intracellularly stained for these cytokines after 4 h of stimulation with PMA and ionomycin. cGAMP-mediated bystander activation had no detectable effect on the percentage of IFN-γ/TNF-α producing $CD4^+$ and $CD8^+$ T cells (Fig. 11). These results demonstrate that although cGAMP transfer increases overall T cell abundance it does not provoke activation or differentiation of T cells.

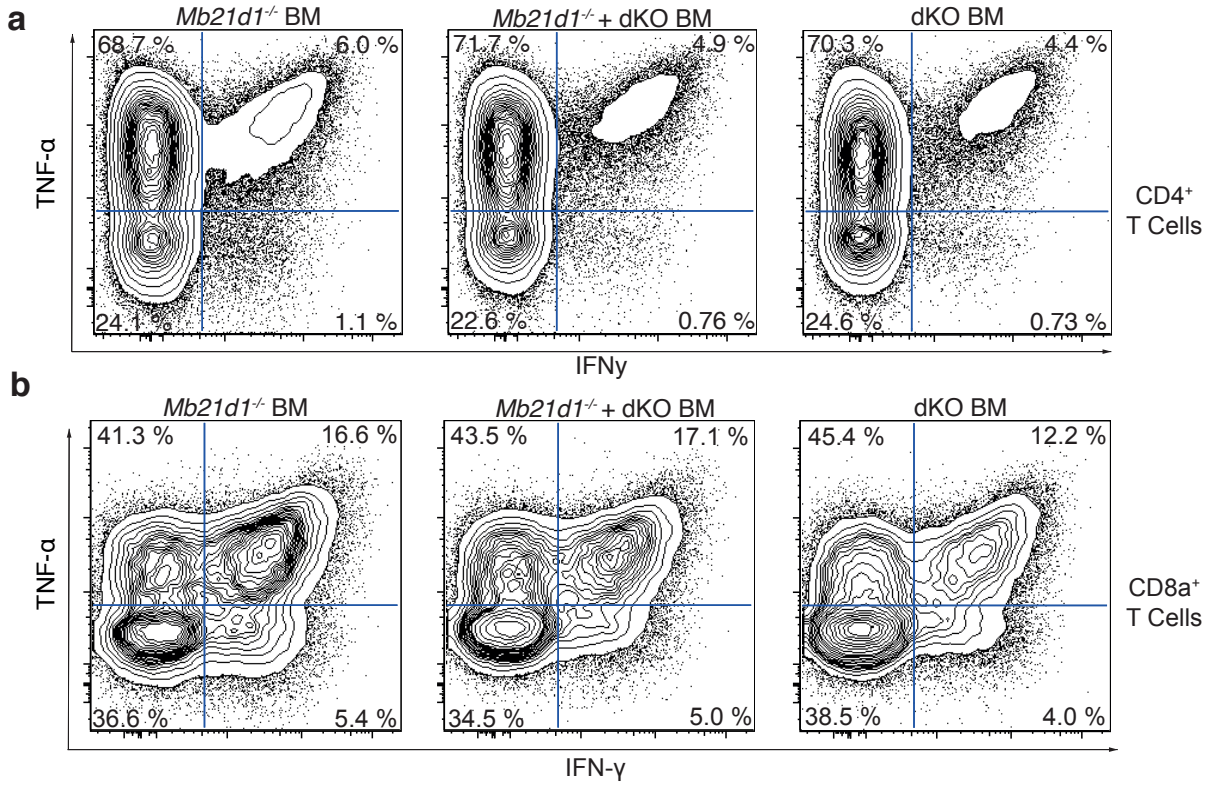

Figure 11. cGAMP transfer does not lead to elevated cytokine expression in CD4$^+$ and CD8a$^+$ lymphocytes. FACS contour plots display IFN-γ and TNF-α staining profiles of gated CD4$^+$ (upper panel) and CD8a$^+$ (lower panel) T cells of PMA- plus ionomycin-stimulated splenocytes from *Mb21d1*$^{-/-}$ BM (n = 14), *Mb21d1*$^{-/-}$ + dKO BM (n = 14), and dKO BM mice (n = 16). Values indicate percentage of live TCRß$^+$, CD4$^+$ T cells and live, TCRß$^+$, CD8a$^+$ T cells, respectively.

4.1.4 Transmission of cGAMP is unable to induce B cell differentiation into plasmablasts and autoantibody production

The activation of self-reactive B cells and induction of autoantibody formation is a defining characteristic of autoimmunity and readily detectable in TREX1 deficiency.[74] Therefore, the question arises, whether cGAMP shuttling facilitates B cell autoimmunity. First, splenic B cell numbers were determined and found to be elevated in *Mb21d1*$^{-/-}$ BM mice compared to dKO mice (Fig. 12a). As for T cells, Sca-1 protein expression levels were again higher in B cells from *Mb21d1*$^{-/-}$ BM and *Mb21d1*$^{-/-}$ + dKO BM mice than in their counterparts from dKO mice (Figs. 12b and 12c).

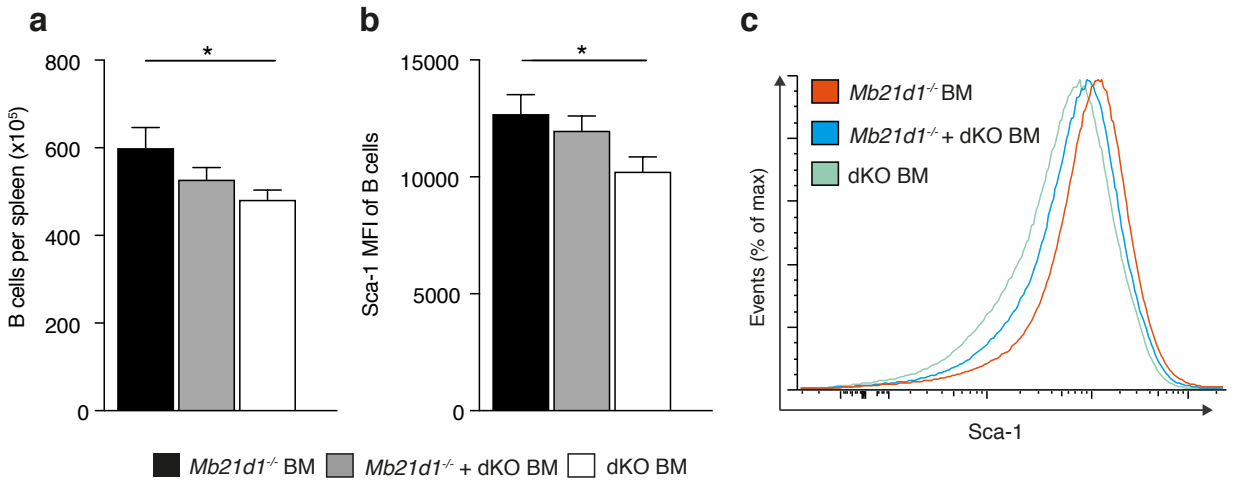

Figure 12. B cell accumulation is enhanced due to cGAMP traveling. **(a)** Number of B cells in spleens from *Mb21*dl$^{-/-}$ BM (n = 14), *Mb21dl*$^{-/-}$ + dKO BM (n = 14), and dKO BM mice (n = 16). **(b)** Mean fluorescence intensity (MFI) for Sca-1 of splenic B cells in *Mb21dl*$^{-/-}$ BM (n = 7), *Mb21dl*$^{-/-}$ + dKO BM (n = 7), and dKO BM mice (n = 6). **(c)** Representative Sca-1 staining histograms of splenic B cells. Data in bar graphs are represented as mean + SEM. Statistics were calculated by Mann-Whitney-U Test with *p < 0.05. Data are pooled from 4 (a) or 2 (b) independent experiments.

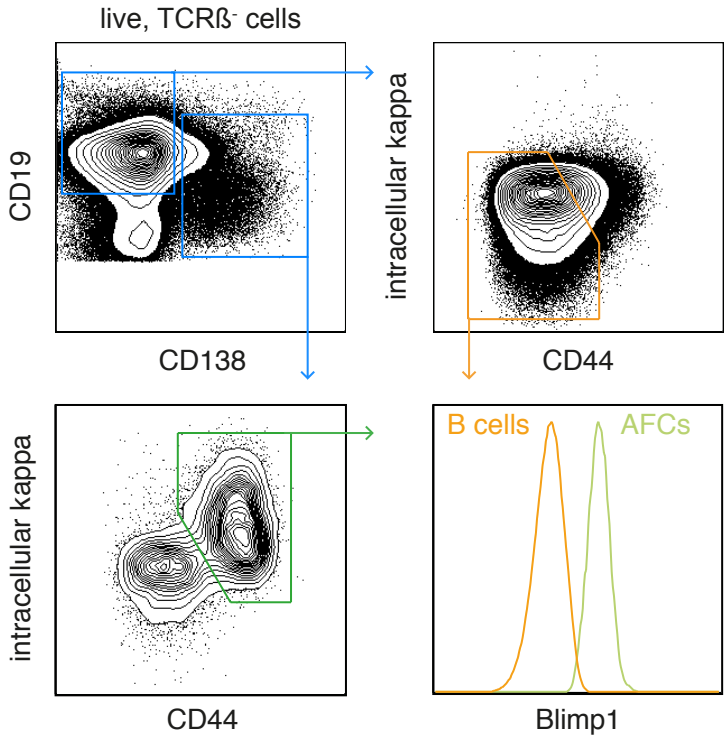

Figure 13. Gating Strategy for B cells and AFCs. Contour plots show the gating strategy for B cells (orange gate) and AFCs (green gate). The histogram illustrates expression of Blimp1, which drives the terminal differentiation of B cells to plasma cells, in B cells and AFCs.

Differentiation of activated B cells into antibody secreting plasmablasts and plasma cells is accompanied by the downregulation of the common B cell marker CD19 and upregulation of syndecan-1 (CD138) to high levels on the cell surface. Furthermore, the differentiation of B cells into antibody-forming cells (AFCs) is highly dependent on the transcription factor Blimp1.[76–78] Therefore, splenic antibody-forming cells were identified by the markers CD138^{+}CD44^{+}intracellular-kappa^{high}Blimp1^{+} and analyzed by flow cytometry (Fig. 13). Of note, antibody-forming cells in spleens of *Trex1*$^{-/-}$ mice show robust proliferation but have a high cell death rate (Figs. 14a and 14b). They likely correspond to short-lived plasmablasts rather than long-lived plasma cells. There was a trend towards more plasmablasts in *Mb21d1*$^{-/-}$ BM and *Mb21d1*$^{-/-}$ + dKO BM mice compared to dKO controls (Fig. 14c), but this effect did not reach statistical significance despite a large number of analyzed mice (n = 14-16).

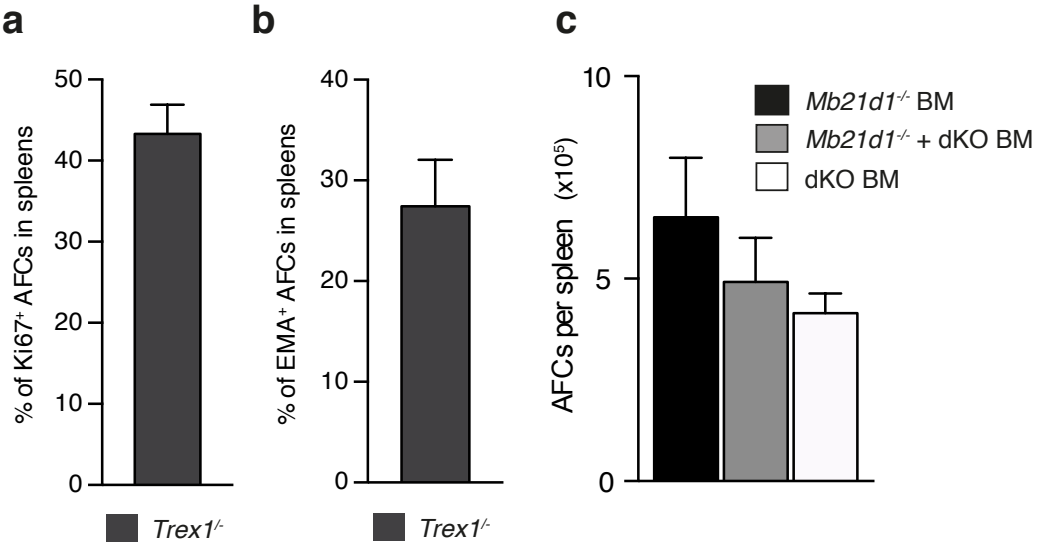

Figure 14. Antibody-forming cells (AFCs) in *Trex1*$^{-/-}$ mice are presumably specified as short-lived plasmablasts, which are not significantly upregulated in BM chimera. Frequency of **(a)** proliferating (Ki67^{+}) AFCs and **(b)** cell death rate (EMA^{+}) of AFCs in *Trex1*$^{-/-}$ mice. **(c)** Total numbers of AFCs in spleens from *Mb21d1*$^{-/-}$ BM (n = 14), *Mb21d1*$^{-/-}$ + dKO BM (n = 14) and dKO BM mice (n = 16).

Trex1$^{-/-}$ mice produce autoantibodies that bind to cardiac proteins[79] and contents of the cell nucleus. Serum IgG autoantibodies against cardiac myosin as well as nucleosomes were therefore quantified by ELISAs (Figs. 15a and 15b). Both autoantibody specificities were

consistently detectable in sera from *Trex1*$^{-/-}$ mice and MRL.*Fas*^{lpr} mice, a polygenic model of SLE, which served as a positive control. Serum concentrations in the BM transplant models, however, were not different from those in non-autoimmune C57Bl/6 mice. Thus, cGAMP shuttling did not succeed in recapitulating the self-directed humoral response in *Trex1*$^{-/-}$ mice. Overall, these results do not support the hypothesis that cGAMP-mediated bystander activation induces the production of autoantibodies.

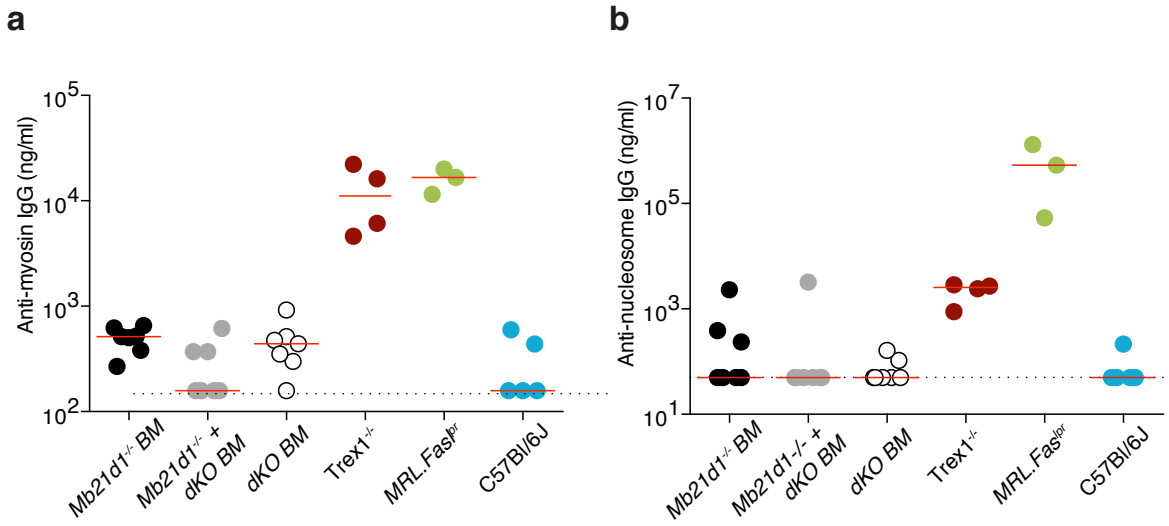

Figure 15: Transmission of cGAMP does not result in autoantibody secretion. Serum concentrations of anti-nucleosome IgG **(a)** and anti-myosin IgG **(b)** ELISA in *Mb21d1*$^{-/-}$ BM, *Mb21d1*$^{-/-}$ + dKO BM, dKO BM, lupus-prone MRL.*Fas*^{lpr} and wild-type C57BL/6J mice. Each dot represents an individual mouse. Median values are represented by horizontal red lines.

4.1.5 cGAMP travel mediates myeloid cell expansion but not dendritic cell maturation

cGAMP augments antiviral immunity after vaccination and this adjuvanticity has been ascribed to its ability to mature DCs[80–82]. Based on the finding that intercellular cGAMP transmission induced IRF3 signals in the cDCs, it could be expected that this would also give them the ability to effectively present antigens. However, there was no evidence that cGAMP travel promoted priming of self-reactive T cells. Hence, the effect of cDC stimulation by cGAMP transfer was uncertain. Unexpectedly, increased IRF3 signaling in *Mb21d1*$^{-/-}$ BM and *Mb21d1*$^{-/-}$ + dKO BM did not lead to the upregulation of MHC class II molecules or the co-stimulatory ligand CD86 (Fig. 16). These results indicate that cell-

extrinsic cGAMP does not convert immature cDCs into immunologically competent antigen presenting cells in TREX1 deficiency.

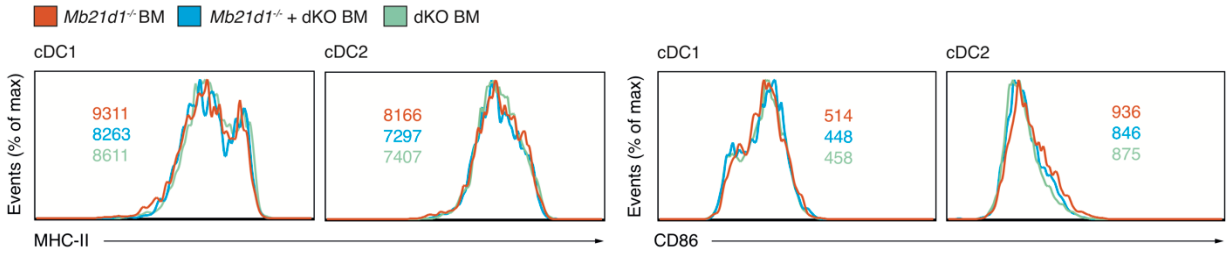

Figure 16. Dendritic cell maturation is not triggered by cGAMP traveling. Representative staining histograms for MHC-II and CD86 of gated cDCs from *Mb21*d1$^{-/-}$ BM (n = 9), *Mb21d1*$^{-/-}$ + dKO BM (n = 10), and dKO BM mice (n = 11). Values indicate the mean of the fluorescence intensity (MFI). Data are pooled from 3 independent experiments.

4.1.6 cGAMP travel guards lymphoid and myeloid immune cells from apoptosis

Because cGAMP shuttling increased T and B cell numbers in the spleen, it was disputable whether it also led to quantitative changes in the myeloid compartment. Numbers of cDC1s and cDC2s in spleen were markedly elevated in *Mb21d1*$^{-/-}$ BM compared to dKO mice, whereas pDC numbers were similar in all groups. Neutrophil and classical monocyte numbers, but not red pulp macrophages were also increased in *Mb21d1*$^{-/-}$ BM and *Mb21d1*$^{-/-}$ + dKO BM compared to dKO mice (Fig. 17).

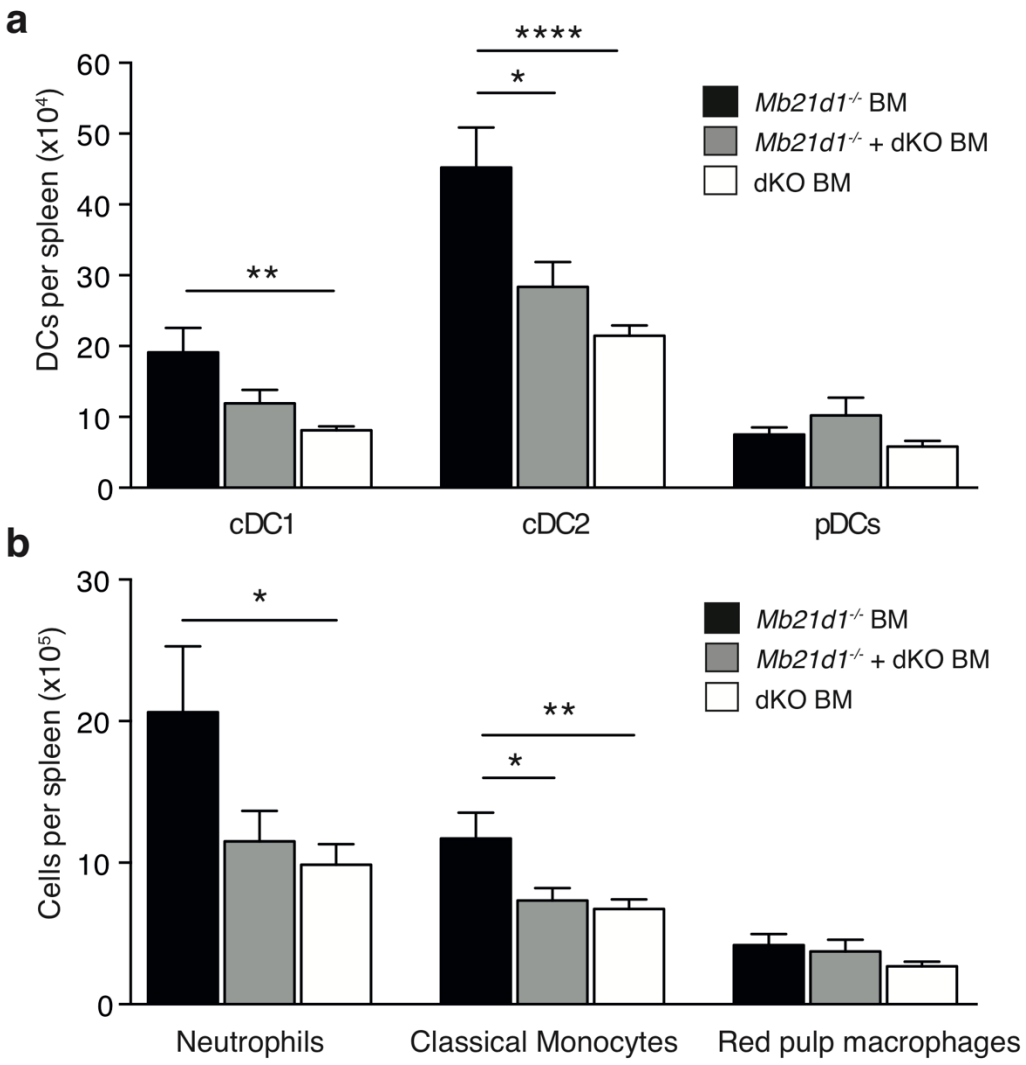

Figure 17. cGAMP transfer elevates the amounts of several myeloid cell subsets. Number of **(a)** dendritic cell subsets and **(b)** further myeloid cell subsets in spleens from *Mb21d1*$^{-/-}$ BM (n = 14), *Mb21d1*$^{-/-}$ + dKO BM (n = 14) and dKO BM mice (n = 16). Bar graphs are represented as mean + SEM. Statistics were calculated by two-tailed Mann-Whitney-U Test. *p < 0.05; **p < 0.01; **** p < 0.0001. Data are pooled from 4 independent experiments.

To understand how cGAMP transfer controls the abundance of different immune cell subsets, it was investigated whether it promotes cell survival. For this purpose, the FITC-labeled pan-caspase inhibitor VAD-FMK was used in combination with scatter characteristics to detect apoptotic cells by flow cytometry (Fig. 18d). Remarkably, in *Mb21d1*$^{-/-}$ BM mice splenic T cells, B cells, cDCs, and neutrophils underwent apoptosis at a considerably lower rate than in dKO mice (Figs. 18a-c). In addition, proliferative activity

was analyzed by staining for Ki67 antigen, but no differences between the BM transplant models were observed (Fig. 19). These results demonstrate that cGAMP transmission stimulates survival of several lymphoid and myeloid cell subsets in the spleen, thereby promoting their accumulation.

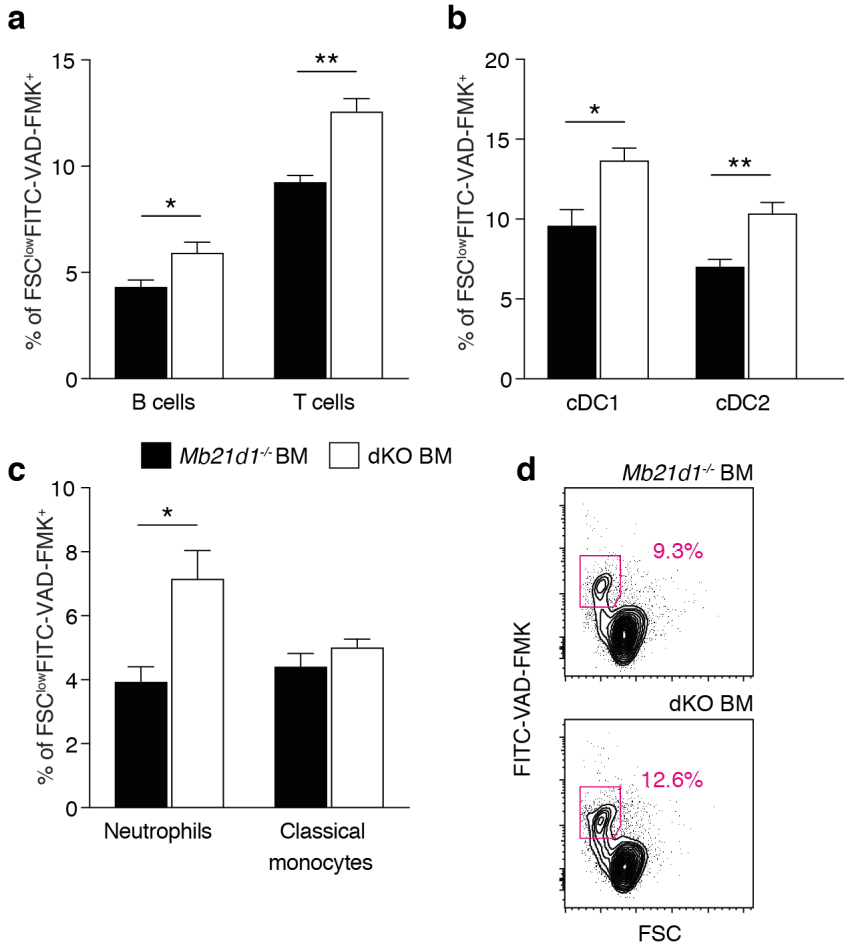

Figure 18. cGAMP transfer guards lymphoid and myeloid immune cells from apoptosis. Percentage of apoptotic cells (FSC^{low}FITC-VAD-FMK^+) among **(a)** lymphocyte and **(b, c)** myeloid cell subsets in spleens from *Mb21d1*$^{-/-}$ BM (n = 6) and dKO BM mice (n = 6). **(d)** Flow cytometry plots show gating of apoptotic T cells in spleens of *Mb21d1*$^{-/-}$ BM and dKO BM mice. Numbers indicate percentage of T cells. Data in bar graphs are represented as mean + SEM. Statistics were calculated by two-tailed Mann-Whitney-U test with *p < 0.05; **p < 0.01. Data are pooled from 2 independent experiments.

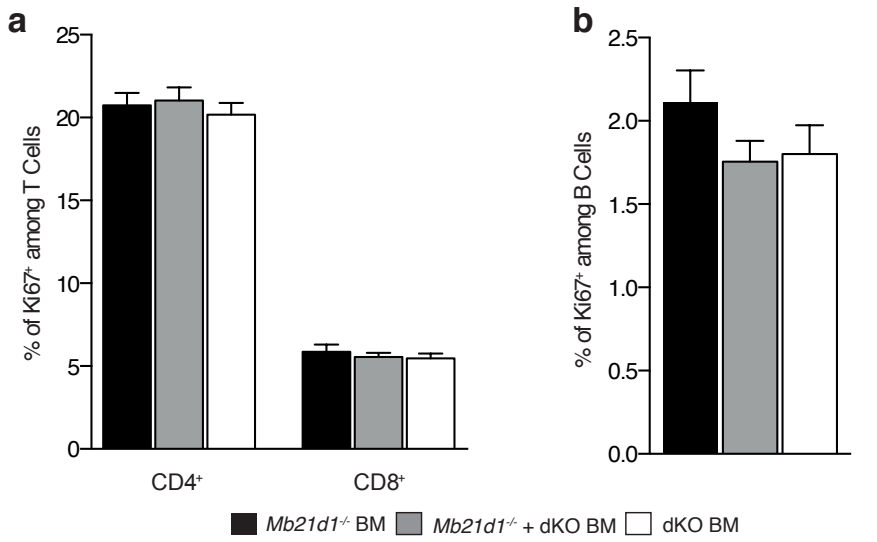

Figure 19. Proliferation of T and B cells in spleens is unaffected by cGAMP transmission. Percentage of **(a)** $CD4^+$ and $CD8^+$ T cells, and **(b)** B cells that are proliferating ($Ki67^+$) in spleens from *Mb21d1*$^{-/-}$ BM (n = 14), *Mb21d1*$^{-/-}$ + dKO BM (n = 14,) and dKO BM mice (n = 16). Data in bar graphs are represented as mean + SEM. Data are pooled from 4 independent experiments.

4.1.7 Intercellular cGAMP passage induces interface dermatitis after UV light exposure

Trex1$^{-/-}$ mice spontaneously develop multiorgan inflammation, which is clearly evident on a C57BL/6 background already at the age of 6 weeks. Cardiac and tongue muscles are reproducibly affected. To establish the impact of cGAMP-mediated bystander activation on organ disease, severity of myocarditis and glossitis was scored by histology. At 12 weeks after transplantation all groups showed only minimal signs of inflammation (Figs. 20 and 21) with no discernible difference between the bone marrow transplant models. To verify that no subtle differences were overlooked, immune cell infiltration into the heart was additionally quantitated by flow cytometry (Fig. 22), yielding similar results in all analyzed groups.

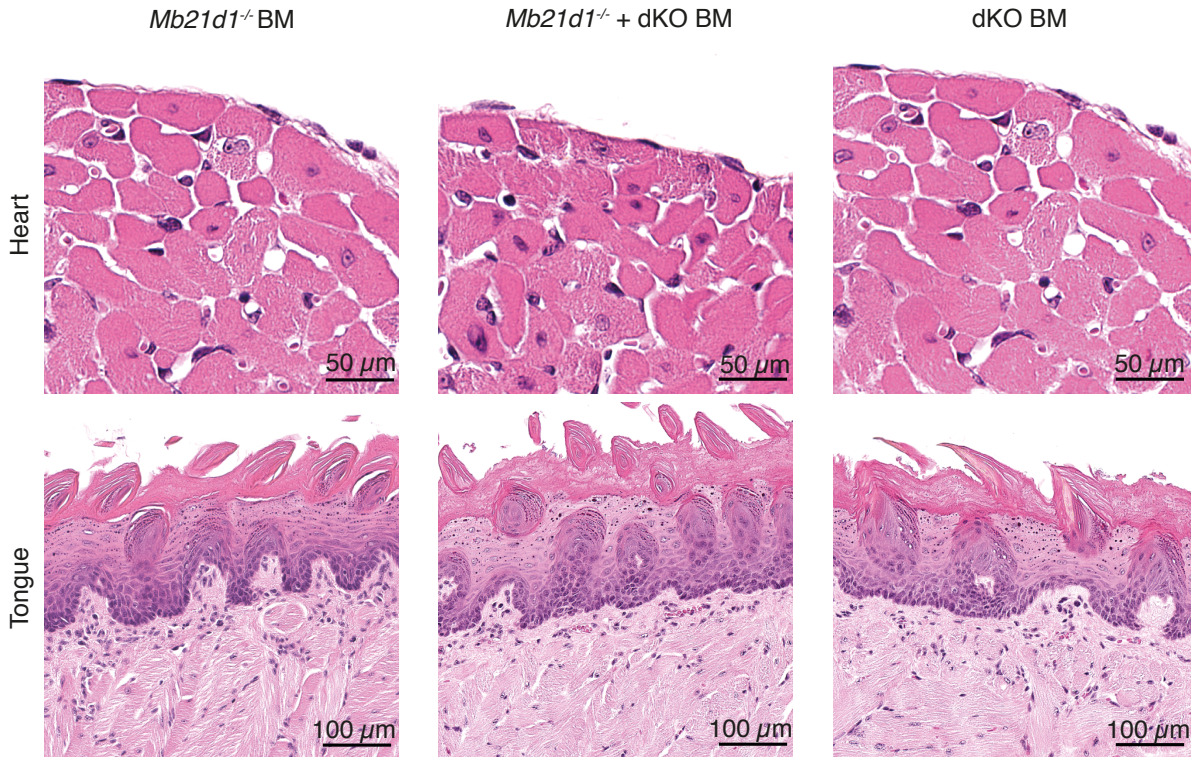

Figure 20. Spreading of innate immunity by intercellular cGAMP transfer does not lead to spontaneous organ disease in autoimmunity. Representative images of Hematoxylin & Eosin (H&E)-stained sections of hearts (upper panels) and tongues (lower panels) of *Mb21d1*$^{-/-}$ BM, *Mb21d1*$^{-/-}$ + dKO BM, and dKO BM mice. Scale bars equal 50 μm for hearts and 100 μm for tongues.

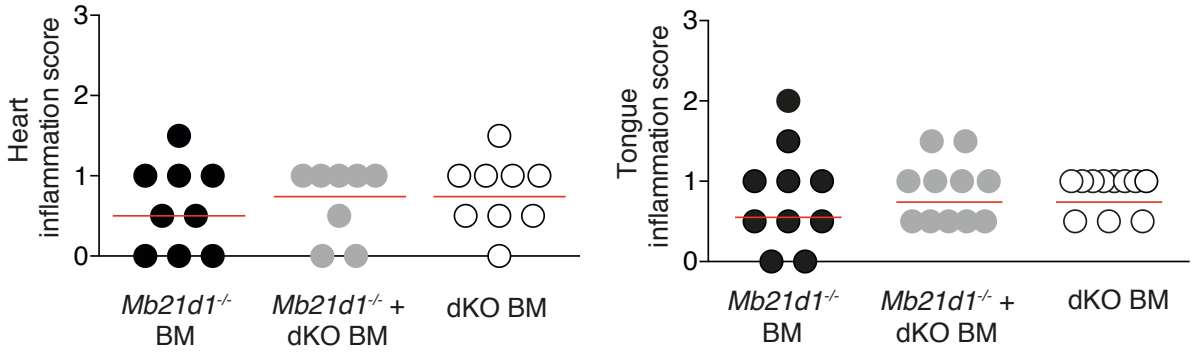

Figure 21. cGAMP transfer does not initiate organ inflammation in hearts or tongues of BM-transplanted animals. Inflammation in hearts and tongues was scored from 0 to 3 with no sample reaching an inflammation score of 3 or higher. Shown are scores of *Mb21d1*$^{-/-}$ BM, *Mb21d1*$^{-/-}$ + dKO BM and dKO BM mice. Each dot depicts an individual mouse, Median values are represented by horizontal red lines.

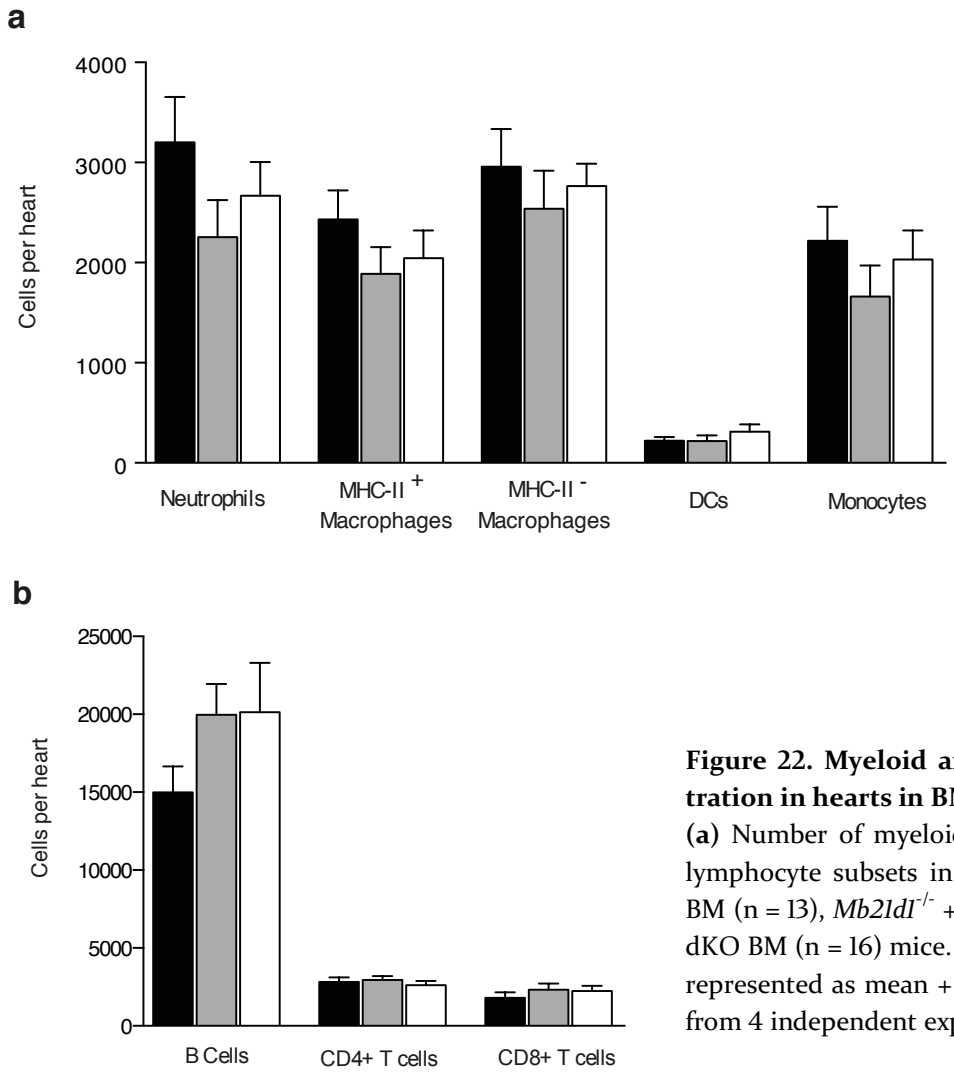

Figure 22. Myeloid and lymphocyte infiltration in hearts in BM transplant models. **(a)** Number of myeloid cell subsets and **(b)** lymphocyte subsets in hearts from *Mb21d1*$^{-/-}$ BM (n = 13), *Mb21d1*$^{-/-}$ + dKO BM (n = 14), and dKO BM (n = 16) mice. Data in bar graphs are represented as mean + SEM. Data are pooled from 4 independent experiments.

Oxidized DNA is less sensitive to TREX1-degradation, and sunlight is a major source of oxidation damage to DNA in the skin.[83] UV light causes cutaneous lupus erythematosus-like skin lesions with interface dermatitis in TREX1-deficient mice.[84] Therefore, the question arises whether the passage of cGAMP between cells could also trigger a UV-dependent autoimmune dermatitis. Strikingly, after UV exposure only *Mb21d1*$^{-/-}$ BM and *Mb21d1*$^{-/-}$ + dKO BM but not dKO BM mice displayed clear histological signs of cell-poor interface dermatitis with basal hydropic degeneration of the epidermis (Fig. 23). Taken together, UV light stimulation led to cutaneous lupus erythematosus-like skin pathology that was dependent on cell-to-cell transmission of cGAMP.

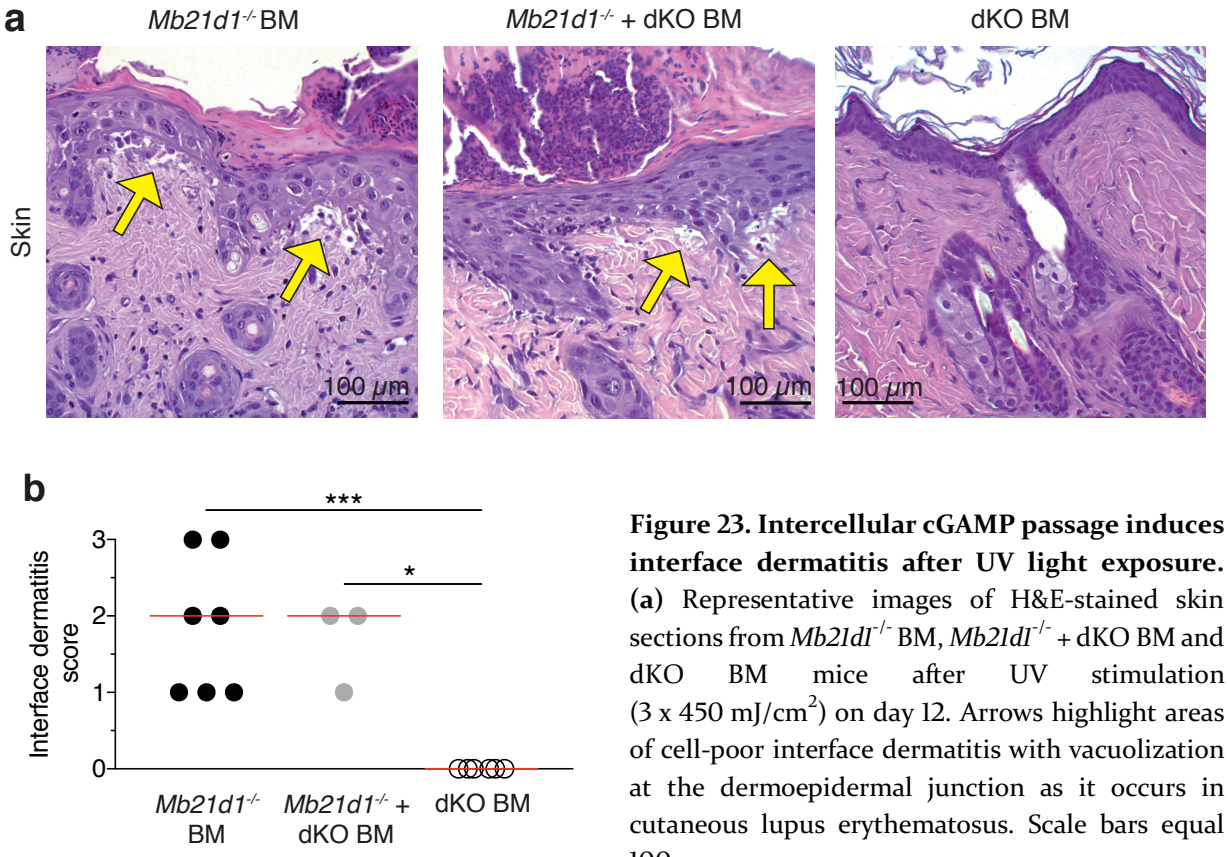

Figure 23. Intercellular cGAMP passage induces interface dermatitis after UV light exposure. **(a)** Representative images of H&E-stained skin sections from *Mb21d1*$^{-/-}$ BM, *Mb21d1*$^{-/-}$ + dKO BM and dKO BM mice after UV stimulation (3 x 450 mJ/cm^2) on day 12. Arrows highlight areas of cell-poor interface dermatitis with vacuolization at the dermoepidermal junction as it occurs in cutaneous lupus erythematosus. Scale bars equal 100 µm.

(b) Interface dermatitis was scored from 0 to 3. Shown are scores of *Mb21d1*$^{-/-}$ BM, *Mb21d1*$^{-/-}$ + dKO BM and dKO BM mice. In scatter dot plots each dot depicts an individual mouse and horizontal red lines represent median values. Statistics were calculated by two-tailed Mann-Whitney-U Test with *$p < 0.05$, ***$p < 0.001$.

4.2 UNC93B1 collaborates with STING on the production of self-directed antibodies in *Trex1*$^{-/-}$-related autoimmunity

The second part of this project was designed to gain a deeper understanding of the importance of TLR signaling in conjunction with the cGAS-STING axis. In TREX1 deficiency, self-DNA sensing of cGAS is crucial for the induction of type I IFNs and interferon stimulated genes (ISGs), thus enabling the initiation of autoimmunity.[59] However, it remains unclear whether further DNA sensors, such as TLRs, are involved and if so to what extent their co-activation may play a role in the development of autoimmunity and the selection of therapeutic interventions.

Endosomal TLRs, specifically TLR7 and TLR9, can be stimulated by extracellular self-NAs which leads to APC activation and presentation of autoantigens to T cells (Fig. 24). To evaluate the impact of TLR signaling on autoimmune disease, *Trex1*$^{-/-}$ mice were used that feature an additional mutation in the UNC93B1 protein (genotype referred to as *Unc93b1*$^{3d/3d}$ hereafter). The 3d mutation specifically refers to a single point mutation of *Unc93b1* at the codon of histidine 412, which is located in the C-terminal transmembrane domain. UNC93B1 is a trafficking chaperone, translocating several TLRs directly from the ER to endolysosomes upon their activation.[25] Over time, UNC93B1 has been shown to enable the correct travelling and function of at least seven TLRs (TLR3, TLR7, TLR8, TLR9, TLR11, TLR12 and TLR13) by directly controlling the packaging of TLRs into vesicles, budding from the ER.[85] More recently, it has been observed that UNC93B1 is also crucial for plasma membrane localization and signaling of TLR5.[26] UNC93B1 has been shown to regulate maturation of TLRs at an early stage, and is crucial to maintain their stability and expression.[27] Hence, the 3d mutation of *Unc93b1* leads to a near-complete loss of the endosomal TLR activity (TLR3, TLR7, and TLR9), which makes the *Unc93b1*$^{-/-}$ mice a suitable deficiency model for studying these TLRs.[25] Additionally, UNC93B1 has been described to be involved in antigen presentation, but this result remains controversial. Some studies revealed impaired antigen presentation resulting in a reduced T cell response in mice with a defect in UNC93B1, while others could not reproduce these effects on antigen presentation.[67,86–88]

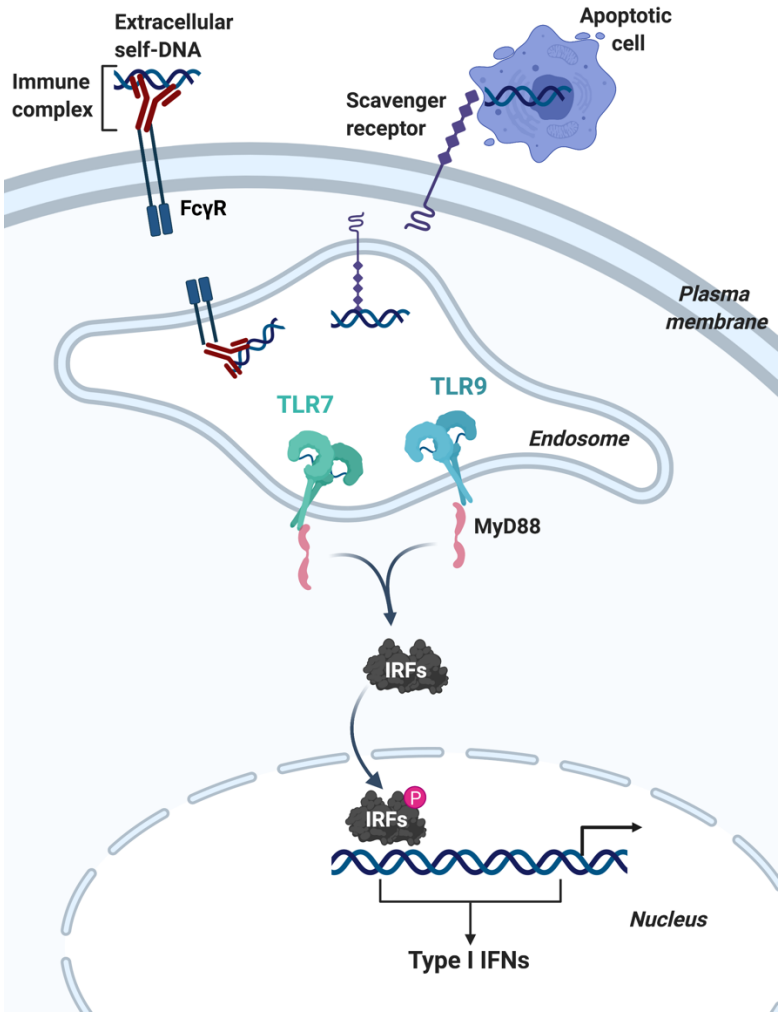

Figure 24. Schematic overview on receptor-mediated self-NA uptake and sensing by TLR7 or TLR9. Uptake of immune complexes containing autoantigens into APCs can be mediated by the Fcγ receptor, delivering self-NAs to endosomes, where they are detected by local TLRs (RNA by TLR7 and DNA by TLR9). Self-DNA originating from apoptotic cells can be ingested by phagocytosis. In B cells, a direct B cell receptor mediated uptake is possible (not shown).[89] TLR activation eventually triggers type I IFN production via IRFs. Figure created with BioRender.

4.2.1 *Trex1*$^{-/-}$;*Unc93b1*$^{3d/3d}$ mice develop more severe myocarditis than *Trex1*$^{-/-}$ mice

To investigate the impact of the defective TLR signaling caused by the *Unc93b1*$^{3d/3d}$ mutation on tissue disease of TREX1-deficient mice, I generated double-deficient animals for both TREX1 and UNC93B1 (*Trex1*$^{-/-}$;*Unc93b1*$^{3d/3d}$). As an important hallmark of autoimmunity, the presence of myocarditis was used as a readout of disease severity. Therefore, inflammation in hearts of these animals were scored by histology at 12 weeks of age. In H&E stained histology images, *Trex1*$^{-/-}$;*Unc93b1*$^{3d/3d}$ mice displayed more severe signs of inflammation in hearts compared to *Trex1*$^{-/-}$ mice (Fig. 25a). Furthermore, scoring of myocarditis revealed significantly elevated inflammation, when scored from 0 (no inflammation) to 4 (severe inflammation) (Fig. 25b).

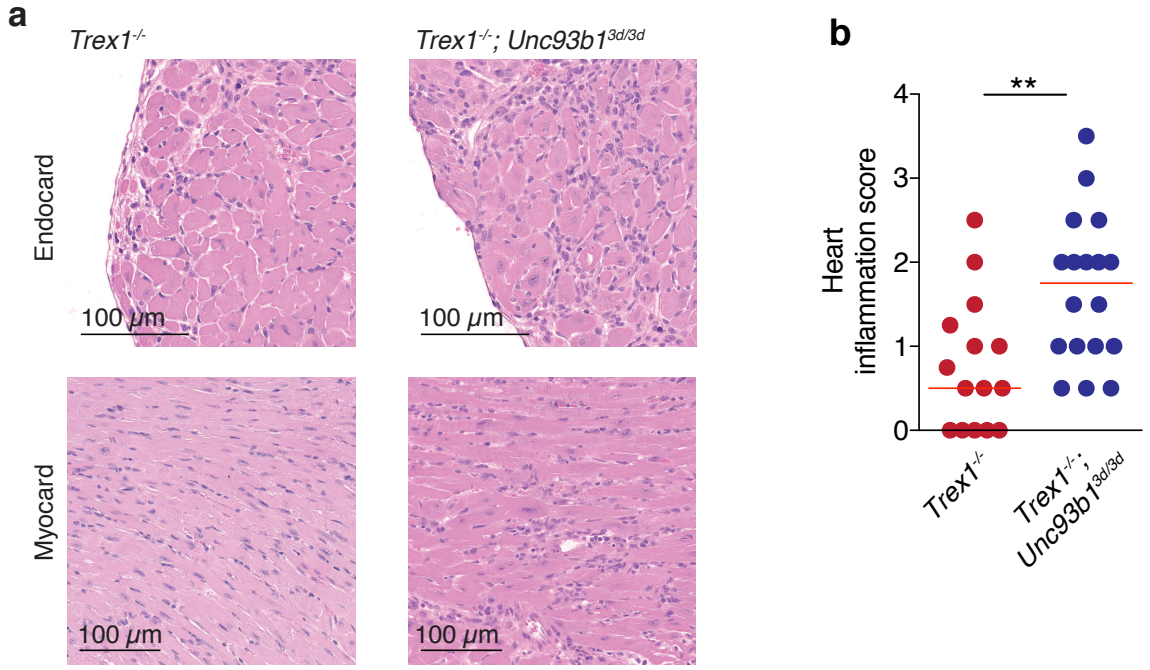

Figure 25. *Unc93b1* 3d mutation aggravates autoimmune-related inflammation in cardiac muscle. **(a)** Representative images of H&E-stained sections of hearts from *Trex1*$^{-/-}$ and *Trex1*$^{-/-}$;*Unc93b1*$^{3d/3d}$ mice. Scale bars equal 100 µm. **(b)** Cardiac inflammation was scored from 0 (no inflammation) to 4 (severe inflammation) in in *Trex1*$^{-/-}$ (n = 15) and *Trex1*$^{-/-}$;*Unc93b1*$^{3d/3d}$ (n = 18) mice. Each dot depicts an individual mouse. Median values are represented by horizontal red lines.

4.2.2 *Unc93b1* 3d results in left ventricular hypertrophy and dysfunction in *Trex1*$^{-/-}$ mice

Several studies have revealed abnormalities in left ventricular structure and mass in the cardiac manifestation among SLE patients. Autoimmunity directly induces these changes by causing chronic myocarditis.[90,91] To evaluate the left ventricular function of *Trex1*$^{-/-}$ and *Trex1*$^{-/-}$;*Unc93b1*$^{3d/3d}$ mice, echocardiography was employed. Hearts of *Trex1*$^{-/-}$;*Unc93b1*$^{3d/3d}$ mice were substantially impaired regarding ejection fraction and fractional shortening in comparison with *Trex1*$^{-/-}$ animals (Figs. 26a and 26b). The left ventricular mass was significantly increased, which was also readily detectable during dissection of *Trex1*$^{-/-}$;*Unc93b1*$^{3d/3d}$ mice (Fig. 26c). These data demonstrate that defects of UNC93B1 cause left ventricular hypertrophy and impairs contractility.

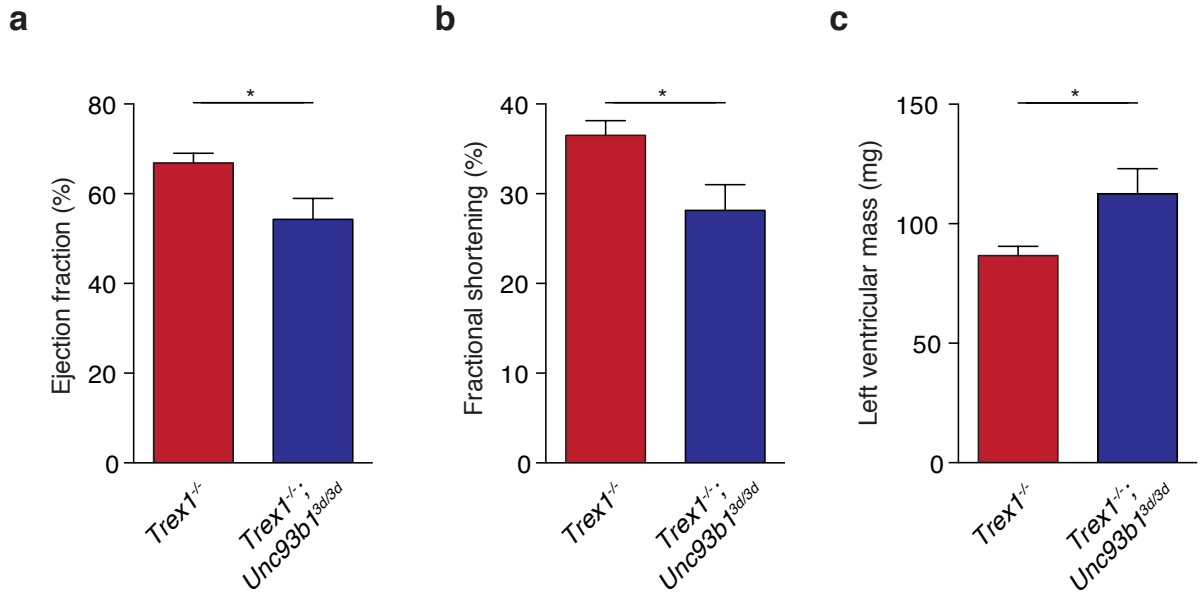

Figure 26. Loss of functional UNC93B1 attenuates inflammatory cardiomyopathy in *Trex1*$^{-/-}$ autoimmunity. Bar graphs display **(a)** ejection fraction, **(b)** fractional shortening and **(c)** left ventricular mass as measured via echocardiography[92] of *Trex1*$^{-/-}$ (n = 15) and *Trex1*$^{-/-}$;*Unc93b1*$^{3d/3d}$ (n = 9) mice. Data shown as mean + SEM. Statistics were calculated by Mann-Whitney-U Test with *$p < 0.05$.

4.2.3 T cell infiltration of hearts is aggravated due to *Unc93b1* 3d mutation

Even though T cells were found to be not crucial for the IFN production in *Trex1*$^{-/-}$ mice, as has been demonstrated for Rag2$^{-/-}$ animals, T cells play an important role in the autoimmune destruction of target tissues.[79] It has been shown that T cells are required for tissue-specific autoimmune inflammation and fibrosis, probably by targeting tissue-specific autoantigens. The following experiment was conducted to determine the contribution of TLR signaling to T cell-dependent autoimmunity and the development of myocarditis in *Trex1*$^{-/-}$ animals. As described above, histopathological scoring of cardiac inflammation in *Trex1*$^{-/-}$*;Unc93b1*$^{3d/3d}$ animals showed a considerable increase when compared to *Trex1*$^{-/-}$ controls (Fig. 25). Correspondingly, numbers of CD4^{+} (Fig. 27a), as well as CD8a^{+} T cells (Fig. 27b) were markedly elevated in mice carrying the 3d mutation.

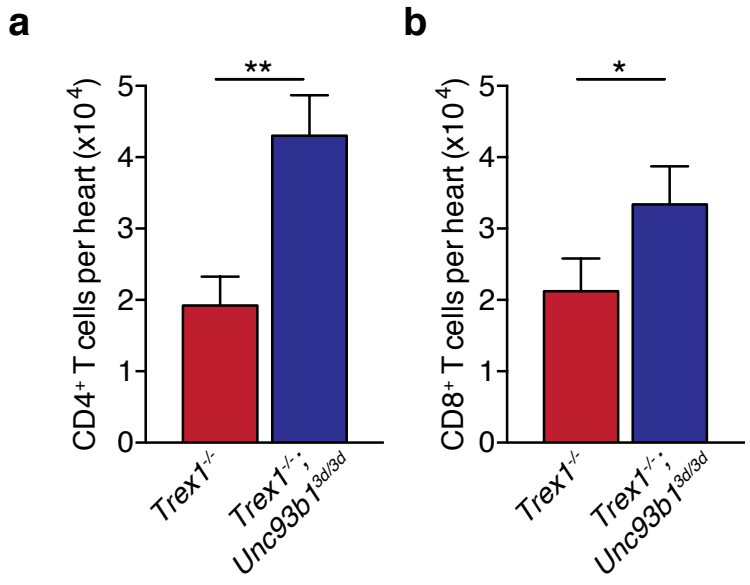

Figure 27. *Unc93b1* 3d mutation increases CD4^{+} and CD8^{+} T cell response in *Trex1*$^{-/-}$ autoimmunity. Numbers of **(a)** CD4^{+} and **(b)** CD8^{+} T cells in hearts of *Trex1*$^{-/-}$ (n = 14) and *Trex1*$^{-/-}$*;Unc93b1*$^{3d/3d}$ (n = 15) mice. Data are represented as mean + SEM. Statistics were calculated by Mann-Whitney-U Test with *p < 0.05, **p < 0.01.

To determine whether the defect of UNC93B1 would also affect T cell differentiation into IFNγ- and TNFα-producing effector cells, splenocytes from both *Trex1*$^{-/-}$ and *Trex1*$^{-/-}$*;Unc93b1*$^{3d/3d}$ mice were stained intracellularly for these cytokines after *in vitro* re-activation. Percentages of both IFNγ- and TNFα-producing CD4^{+} T cells were significantly elevated in *Trex1*$^{-/-}$*;Unc93b1*$^{3d/3d}$ animals. Similarly, CD8^{+} T cells displayed a trend towards an increased cytokine-producing population in mice with defective UNC93B1, but this did

not reach statistical significance (Fig. 28). Together, the spontaneously developing self-directed T cell response observed in *Trex1*$^{-/-}$ animals is enhanced by the 3d mutation suggesting that TLR signaling restricts T cell autoimmunity.

These results contradict the initial reports on the *Unc93b1* 3d mutation indicating that it also causes an antigen presentation defect.[67] If this was the case, one would expect a rather reduced T cell response in *Trex1*$^{-/-}$;*Unc93b1*$^{3d/3d}$ mice compared to TREX1-deficient animals. If there are actually any antigen presentation defects due to the 3d mutation in *Unc93B1*, these did not play a major role in the experiments presented.

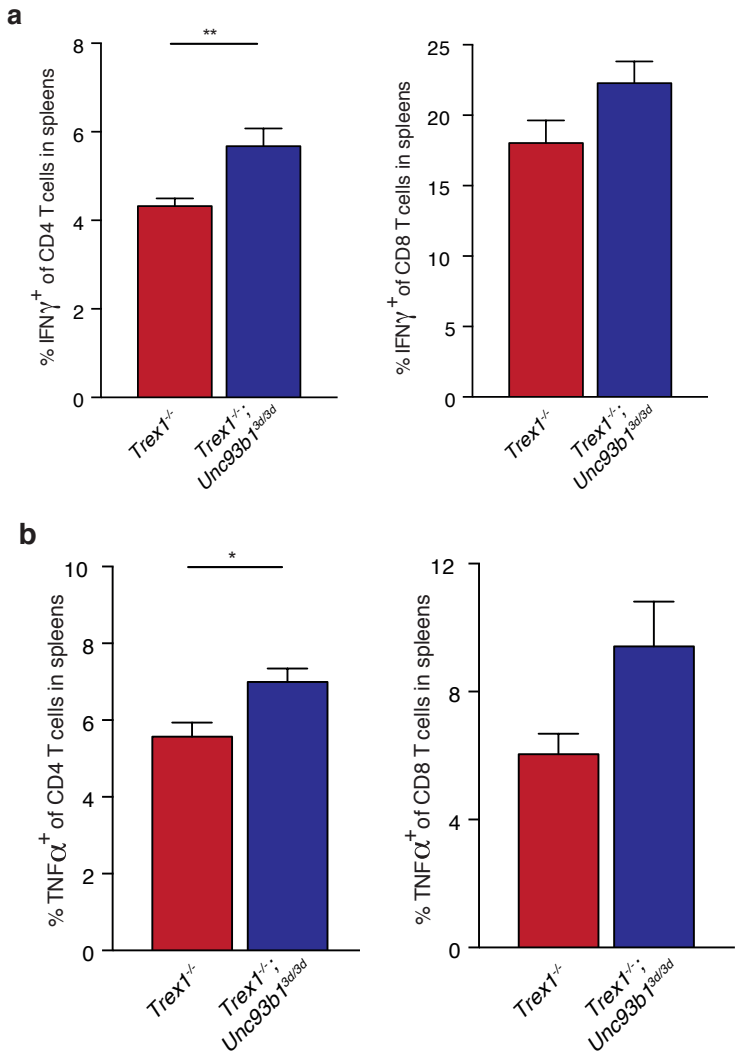

Figure 28. Cytokine production of T cells is elevated in spleens of *Trex1*$^{-/-}$;*Unc93b1*$^{3d/3d}$ mice. Percentages of **(a)** IFNγ$^+$ CD4 and CD8 T cells and **(b)** TNFα$^+$ CD4 and CD8 T cells in spleens of *Trex1*$^{-/-}$ (n = 12) and *Trex1*$^{-/-}$;*Unc93b1*$^{3d/3d}$ (n = 11) mice. Data are represented as mean + SEM. Statistics were calculated by Mann-Whitney-U Test with *p < 0.05 and **p < 0.01.

4.2.4 *Unc93b1* 3d increases monocyte and cDC numbers in hearts of *Trexl*$^{-/-}$ mice

After determining an elevation of CD4^{+} and CD8^{+} T cells in hearts of *Trexl*$^{-/-}$ mice that additionally lack specific TLR signaling due to the *Unc93b1* 3d mutation, the amount of myeloid cell was investigated. Hence, flow cytometric analysis of heart tissue was performed to analyze the infiltrating myeloid cell populations. Heart infiltration of monocytes was considerably higher in *Trexl*$^{-/-}$;*Unc93b1*$^{3d/3d}$ mice, whereas neutrophil counts remained unchanged. Slight increases of macrophage numbers did not reach statistical significance (Fig. 29a). cDC numbers were increased in hearts and spleens (Figs. 29b and 29c).

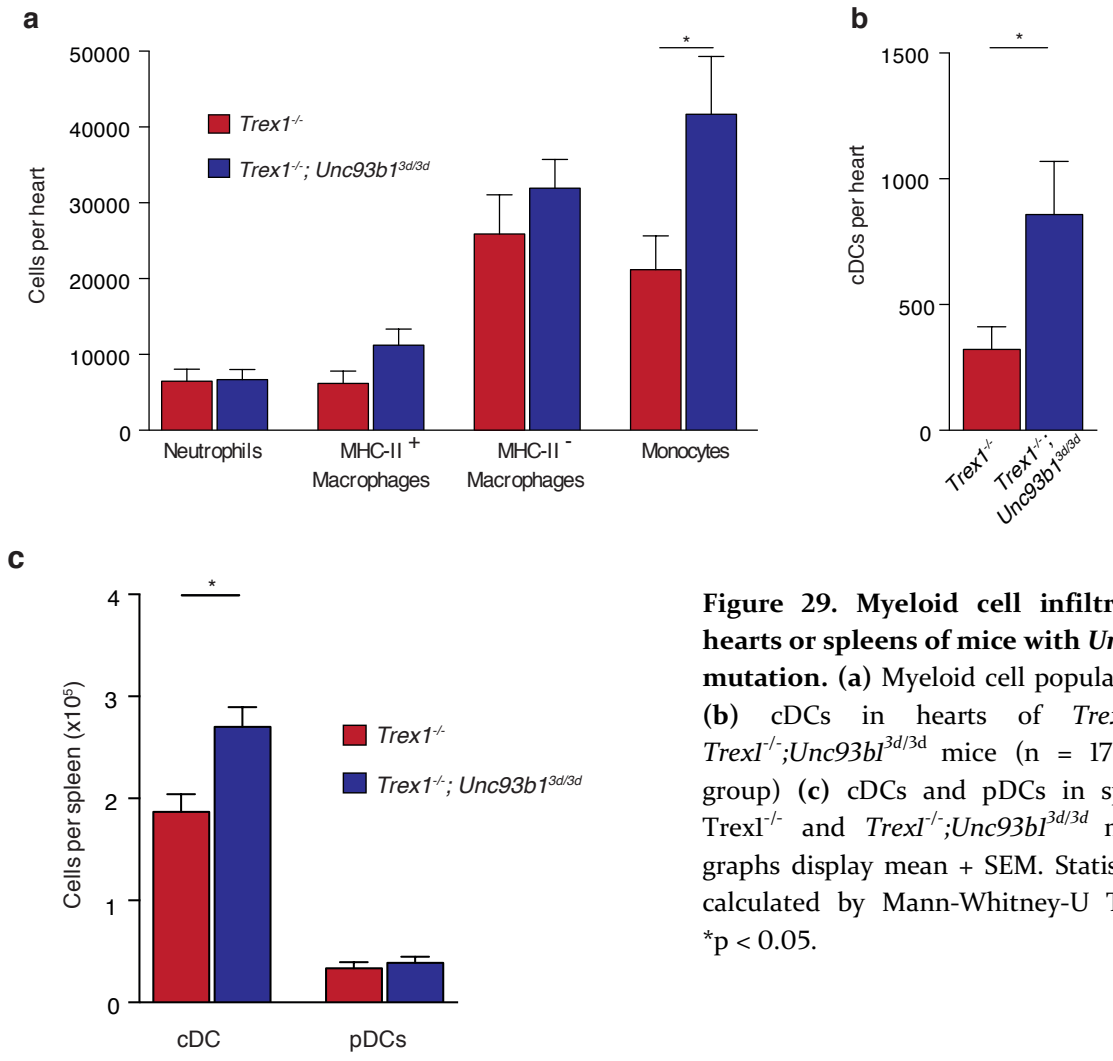

Figure 29. Myeloid cell infiltration in hearts or spleens of mice with *Unc93b1* 3d mutation. **(a)** Myeloid cell populations and **(b)** cDCs in hearts of *Trexl*$^{-/-}$ and *Trexl*$^{-/-}$;*Unc93b1*$^{3d/3d}$ mice (n = 17 in each group) **(c)** cDCs and pDCs in spleens of Trexl$^{-/-}$ and *Trexl*$^{-/-}$;*Unc93b1*$^{3d/3d}$ mice. Bar graphs display mean + SEM. Statistics were calculated by Mann-Whitney-U Test with *$p < 0.05$.

To better understand how UNC93B1 controls T cell autoimmunity, sorted cDCs from *Trex1*$^{-/-}$ and *Trex1*$^{-/-}$;*Unc93b1*$^{3d/3d}$ mice were analyzed by 3'-mRNA-Seq, demonstrating that *Trex1*$^{-/-}$;*Unc93b1*$^{3d/3d}$ animals upregulate gene sets in response to type I IFNs and IFN-γ (Fig. 30). The data indicate that a loss of endosomal TLR signaling leads to a stronger IFN signature in autoimmune-prone *Trex1*$^{-/-}$ mice. Type I IFN-mediated signals promote DC maturation and their capability to prime naïve T cells.[93] These results might thus explain how the 3d mutation enhances T cell autoimmunity in *Trex1*$^{-/-}$ mice.

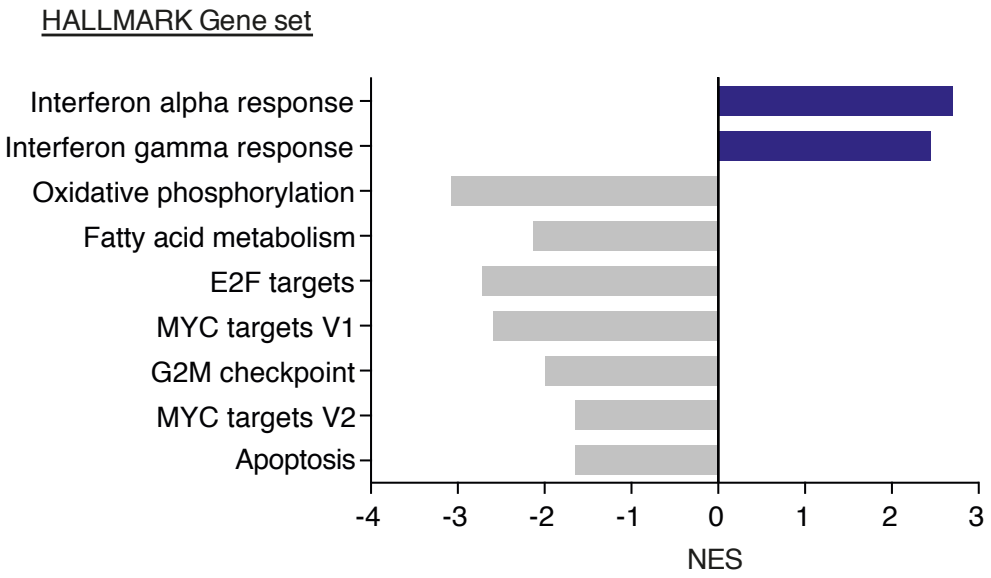

Figure 30. *Unc93b1* 3d mutation elevates expression of IFN-induced gene sets in TREX1 deficiency. Global gene expression analysis by 3'-RNA-seq comparing cDCs sorted from spleens of *Trex1*$^{-/-}$ and *Trex1*$^{-/-}$;*Unc93b1*$^{3d/3d}$ mice (n = 3 per genotype). Normalized Enrichment Scores (NES) of Hallmark gene sets significantly up- or downregulated (false discovery rate q value < 0.01) in *Trex1*$^{-/-}$;*Unc93b1*$^{3d/3d}$ mice compared to *Trex1*$^{-/-}$ mice in a pre-ranked Gene Set Enrichment Analysis (GSEA) based on a metric score calculated by $\log_2$(fold change) x (-$\log_{10}$(p value)).

4.2.5 Endogenous retroviruses are reactivated in *Trex1*$^{-/-}$;*Unc93b1*$^{3d/3d}$ mice

As a relic from the ancient germline infection with retroviruses, the genome of vertebrates contains largely nonfunctional endogenous retroviruses (ERVs). Some of the best-studied retroviruses are the murine leukemia viruses (MuLVs).[94] A study from Yu *et al.* reported

that the loss of TLRs 3, 7, and 9 in C57Bl/6 mice leads to MuLV viremia, demonstrating that these receptors are essential for immune control of ERVs.[95] Furthermore, a study from Stetson *et al.* suggested that the NAs activating cGAS in TREX1-deficient cells are of retroviral origin.[42,74]

To gain a better understanding of the mechanisms that potentially lead to an increased IFN signature in *Trex1*$^{-/-}$*;Unc93b1*$^{3d/3d}$ animals compared to *Trex1*$^{-/-}$ mice, experiments were performed based on the hypothesis that a defect of UNC93B1 might promote the reactivation of MuLV in *Trex1*$^{-/-}$*; Unc93b1*$^{3d/3d}$ mice, which in turn leads to more pronounced cGAS activation and IFN production. Hence, an antibody against the MuLV envelope glycoprotein 70 (anti-MuLV gp70 env), an endogenous viral envelope component that is encoded in the murine genome and transcriptionally silenced under physiological conditions[96] was applied for quantification of MuLV. Indeed, in thymocytes and splenocytes, MuLV was significantly upregulated in *Trex1*$^{-/-}$*;Unc93b1*$^{3d/3d}$ mice (Fig. 31), supporting the assumption that MuLV transcription was reactivated in *Trex1*$^{-/-}$ mice carrying the 3d mutation. Thus, expression of ERVs might contribute to the increased IFN response in *Trex1*$^{-/-}$*;Unc93b1*$^{3d/3d}$ mice.

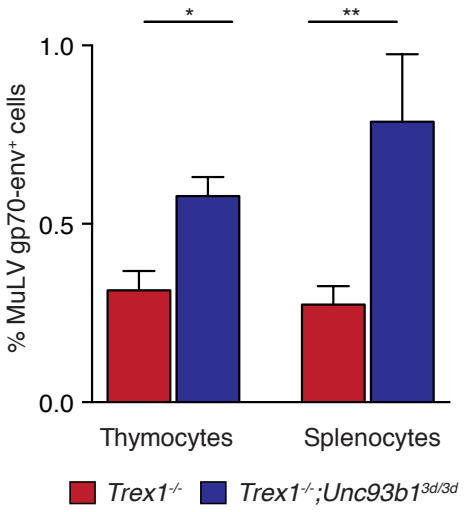

Figure 31. Endosomal TLRs are crucial for the control of endogenous retroviruses. Endogenous retroviruses, represented by murine leukemia virus, present in mice deficient for TREX1 or both TREX1 and UNC93B1. Bar graphs illustrate intracellular flow cytometry staining for MuLV gp70-env in thymocytes and splenocytes of Trex1$^{-/-}$ (n = 6) and Trex1$^{-/-}$;Unc93b1$^{3d/3d}$ (n = 4) mice. Data are displayed as mean + SEM. Statistics were calculated by Mann-Whitney-U Test with *p < 0.05 and **p < 0.01.

4.2.6 *Trex1*$^{-/-}$;*Unc93b1*$^{3d/3d}$ mice show improved survival despite augmented inflammatory myocarditis

In line with the increased organ inflammation and occurrence of myocarditis in *Trex1*$^{-/-}$;*Unc93b1*$^{3d/3d}$ mice compared to the already autoimmunity-prone *Trex1*$^{-/-}$ mice, a correspondingly lower survival rate was expected for these animals. However, after 12 weeks (84 days), *Trex1*$^{-/-}$ animals showed decreased survival than *Trex1*$^{-/-}$;*Unc93b1*$^{3d/3d}$ mice (Fig. 32).

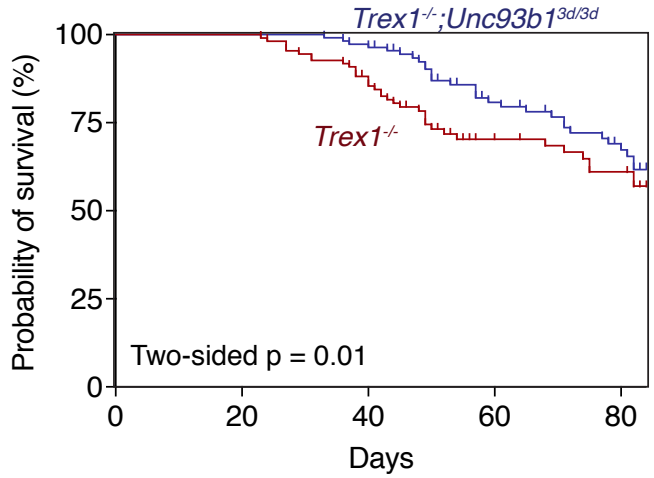

Figure 32. Probability of survival of mice with *Trex1*$^{-/-}$-associated autoimmunity is dependent on functional TLRs. Kaplan-Meier survival analysis[97,98] shows the probability of survival for Trex1$^{-/-}$ (n = 79) and Trex1$^{-/-}$;Unc93b1$^{3d/3d}$ (n = 80) mice. Tick marks indicate censored data since these animals were killed for being used in an experiment. Maximum observation period was 12 weeks (day 84). Data were analyzed by two-sided Gehan-Breslow-Wilcoxon Test.

4.2.7 Signaling of endosomal TLRs is dependent on STING activation and both are required for the production of anti-nuclear antibodies

In various monogenic models of autoimmunity, such as DNase II deficiency, the production of self-reactive antibodies is dependent on endosomal TLRs, particularly on TLR7 and TLR9.[35] Therefore, it was investigated whether ANA formation in *Trex1*$^{-/-}$ animals is likewise based on endosomal TLR signaling. The polygenic MRL.*Fas*^{lpr} mouse model, which serves as a positive control for the following experiments, resembles SLE and features a massive production of antibodies against autoantigens and aberrant T cell proliferation. In this model, the formation of anti-nucleosome and anti-RNA antibodies also entirely depends on TLR9 and TLR7, respectively.[99,100]

To evaluate the presence of ANAs, HEp-2 cells attached to slides were used and treated with mouse sera to detect IgGs against elements of the nucleus. The *Trex1*$^{-/-}$ group of mice produced a homogenous staining pattern, which demonstrates the presence of anti-

chromatin antibodies (Fig. 33a), just like in MRL.*Fas*^{lpr} animals (not shown). Neither in TLR defective mice (*Trex1*$^{-/-}$;*Unc93b1*$^{3d/3d}$) nor in STING deficient mice (*Trex1*$^{-/-}$;*Tmem173*$^{gt/gt}$) ANAs could be detected (Fig. 33b), suggesting that both TLR signaling and previous signaling via the adaptor molecule STING are required for the production of ANAs.

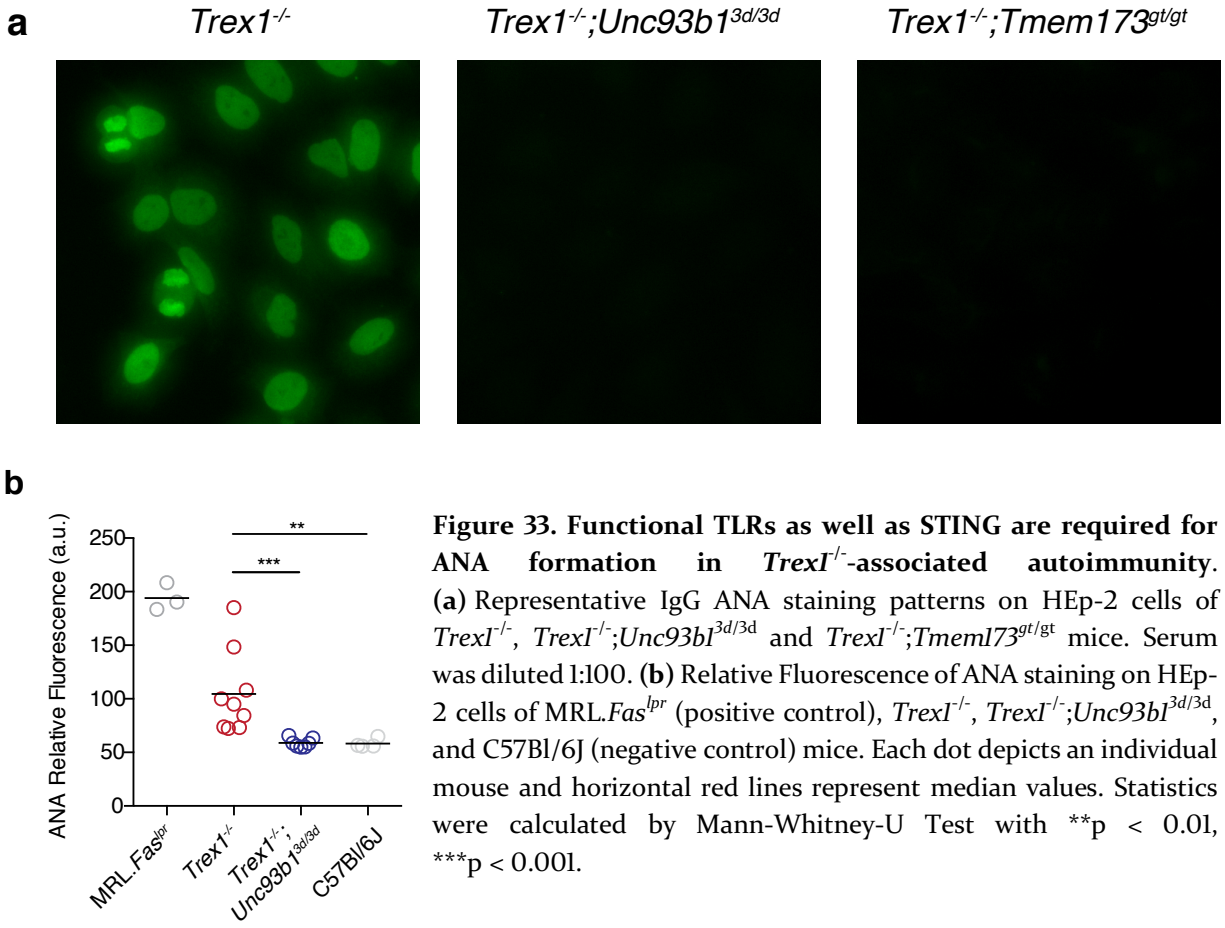

Figure 33. Functional TLRs as well as STING are required for ANA formation in *Trexl*$^{-/-}$-associated autoimmunity. **(a)** Representative IgG ANA staining patterns on HEp-2 cells of *Trexl*$^{-/-}$, *Trexl*$^{-/-}$;*Unc93b1*$^{3d/3d}$ and *Trexl*$^{-/-}$;*Tmem173*$^{gt/gt}$ mice. Serum was diluted 1:100. **(b)** Relative Fluorescence of ANA staining on HEp-2 cells of MRL.*Fas*^{lpr} (positive control), *Trexl*$^{-/-}$, *Trexl*$^{-/-}$;*Unc93b1*$^{3d/3d}$, and C57Bl/6J (negative control) mice. Each dot depicts an individual mouse and horizontal red lines represent median values. Statistics were calculated by Mann-Whitney-U Test with **p < 0.01, ***p < 0.001.

In an additional experimental approach, to examine the dependence of ANAs on TLRs and functional STING protein in TREX1 deficiency, anti-nucleosome and anti-RNA IgG serum concentration were evaluated by ELISA. In *Trexl*$^{-/-}$;*Unc93b1*$^{3d/3d}$ mice, both anti-nucleosome and anti-RNA IgGs were virtually absent in the serum, comparable to levels in wild-type mice. However, anti-myosin antibodies could be detected and were of similar concentration as in *Trexl*$^{-/-}$ mice (Fig. 34), suggesting that this species of autoantibodies, not directed against self-NAs, is not dependent on functional UNC93B1.

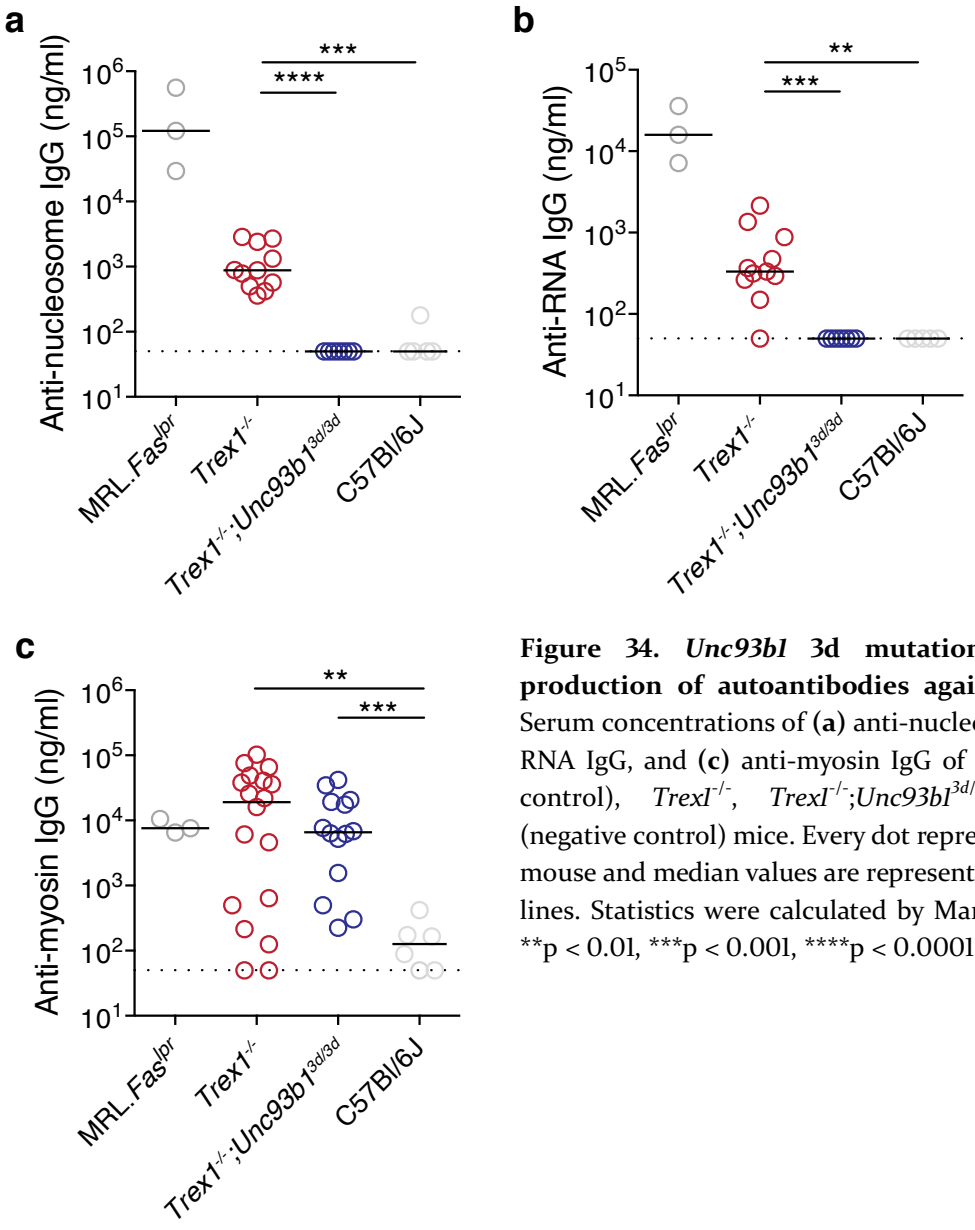

Figure 34. *Unc93b1* 3d mutation eliminates the production of autoantibodies against nucleic acids. Serum concentrations of **(a)** anti-nucleosome IgG, **(b)** anti-RNA IgG, and **(c)** anti-myosin IgG of MRL.*Fas*^{lpr} (positive control), *Trex1*$^{-/-}$, *Trex1*$^{-/-}$;*Unc93b1*$^{3d/3d}$, and C57Bl/6J (negative control) mice. Every dot represents one individual mouse and median values are represented by horizontal red lines. Statistics were calculated by Mann-Whitney-U Test, **p < 0.01, ***p < 0.001, ****p < 0.0001.

Anti-nucleosome and anti-RNA antibodies were also completely abolished in STING-deficient (*Trex1*$^{-/-}$;*Tmem173*$^{gt/gt}$) animals (Fig. 35), suggesting that functional STING is likewise required for the production of anti-nuclear autoantibodies in *Trex1*$^{-/-}$-related autoimmunity and that STING activation enables downstream TLR activation.

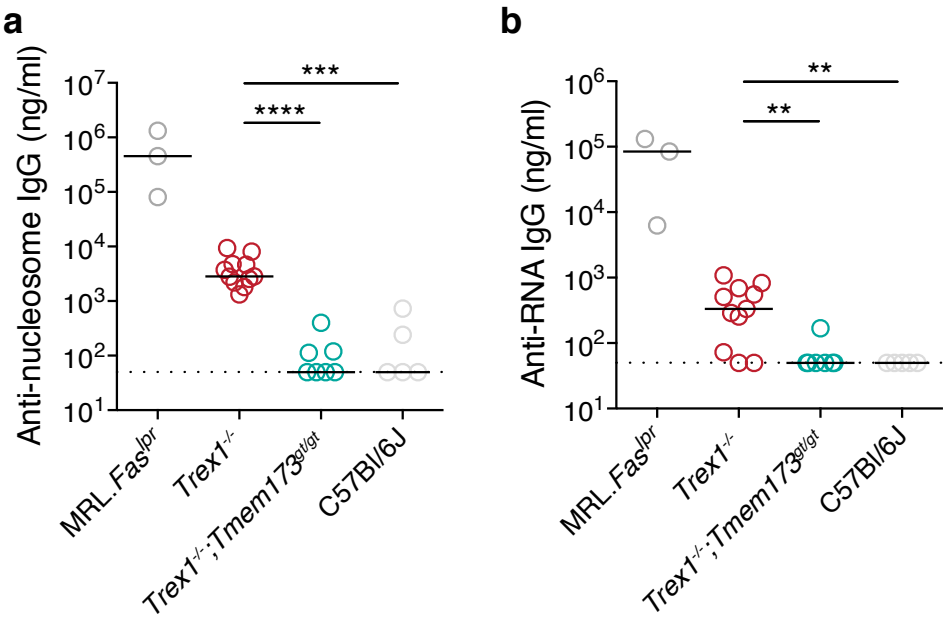

Figure 35. Functional STING is required for the production of anti-nuclear antibodies in autoimmunity. Serum concentrations of **(a)** anti-nucleosome IgG and **(b)** anti-RNA IgG of MRL.*Fas*^{lpr} (positive control), *Trex1*$^{-/-}$, *Trex1*$^{-/-}$;*Tmem173*$^{gt/gt}$ and C57Bl/6J (negative control) mice. Every dot represents an individual mouse. Median values are displayed by horizontal red lines. Statistics were calculated by Mann-Whitney-U Test, **p < 0.01, ***p < 0.001, ****p < 0.0001.

In addition, STING has been reported to play a role in the induction of cell death.[101] Dying cells might thus provide free NAs to TLRs that lead to their activation and eventually to the production of auto-antibodies. To further investigate the role of STING in the production of ANAs, DNA concentrations in the serum of TREX1- and STING-deficient *Trex1*$^{-/-}$;*Tmem173*$^{gt/gt}$ mice were measured. Serum DNA concentrations were substantially diminished in STING-deficient animals (Fig. 36a). Consistently, when measuring cell death of splenocytes via Yo-Pro1 staining, the percentage of Yo-Pro1^{+} cells was significantly lower when STING was absent (Fig. 36b). These results suggest that DNA and conceivably also RNA originating from cell death might provide a trigger for NA-detecting TLRs in autoimmunity related to TREX1 deficiency.

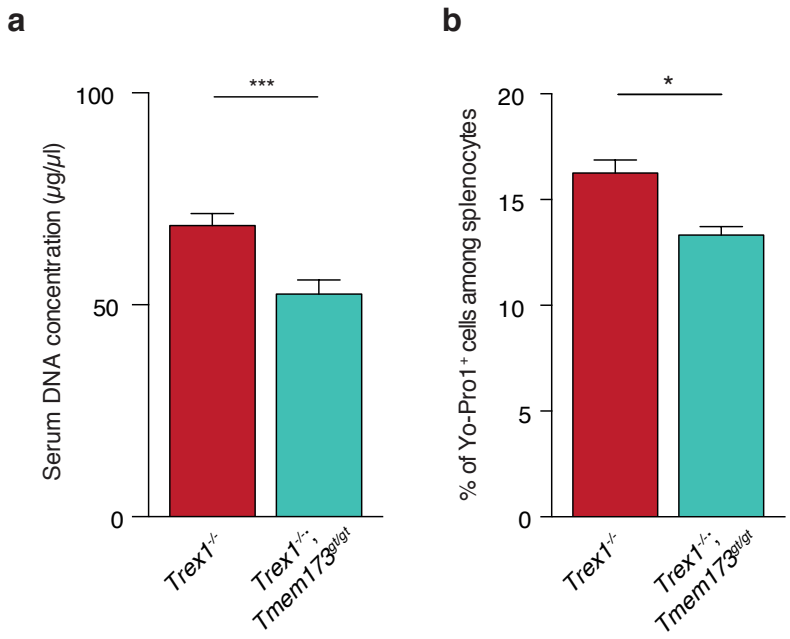

Figure 36. STING promotes elevated serum DNA concentration and cell death in *Trex1*$^{-/-}$-related autoimmunity. Bar graphs illustrate **(a)** serum DNA concentrations in sera of *Trex1*$^{-/-}$ (n = 6) and *Trex1*$^{-/-}$;*Tmem173*$^{gt/gt}$ (n = 12) mice and **(b)** percentage of Yo-Pro1^{+} splenocytes from *Trex1*$^{-/-}$ and *Trex1*$^{-/-}$;*Tmem173*$^{gt/gt}$ animals. Data are displayed as mean + SEM. Statistics were calculated by Mann-Whitney-U Test with *p < 0.05; ***p < 0.001.

4.2.8 Differentiation into antibody-forming plasmablasts is impaired in *Trex1*$^{-/-}$ mice with defective TLR signaling

In accordance with the findings on ANA formation, which was virtually absent in *Trex1*$^{-/-}$;*Unc93b1*$^{3d/3d}$ animals, AFC numbers were greatly reduced in *Trex1*$^{-/-}$;*Unc93b1*$^{3d/3d}$ mice, indeed to a level found in non-autoimmune wild-type animals (Fig. 37a) whereas the absolute numbers of B cells in the spleens of *Unc93b1*-3d-mutated animals were not reduced (Fig. 37b). This indicates that even in a model of autoimmunity, in which disease development is induced by the cGAS-STING axis, the anti-self B cell response, as assessed by autoantibody production and AFC differentiation, is to a great extent TLR-dependent.

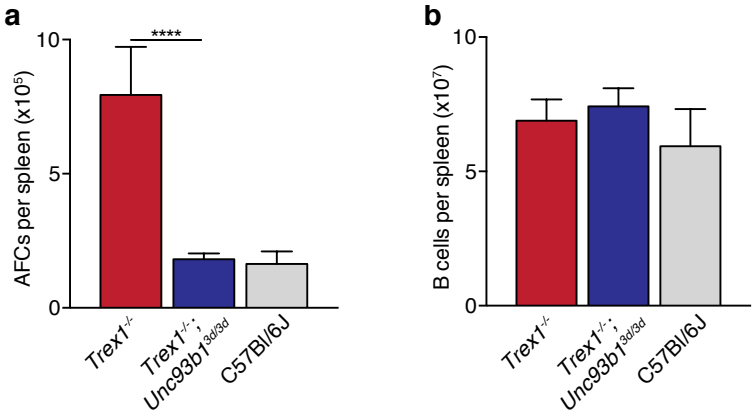

Figure 37. Numbers of splenic AFCs in *Trexl*$^{-/-}$ mice with an additional defect in endosomal TLR signaling (*Unc93bl*$^{3d/3d}$) are reduced to levels of non-autoimmune wild-type mice. Numbers of **(a)** AFCs and **(b)** B cells in spleens of *Trexl*$^{-/-}$ (n = 12), *Trexl*$^{-/-}$;*Unc93bl*$^{3d/3d}$ (n = 12), and wild-type C57Bl/6J (n = 4) mice. Data are represented as mean + SEM. Statistics were calculated by Mann-Whitney-U Test with ****p < 0.0001.

AFCs in *Trexl*$^{-/-}$ as well as in *Trexl*$^{-/-}$;*Unc93bl*$^{3d/3d}$ animals showed an equally high proliferation rate (Fig. 38a). In contrast, B cell proliferation was significantly reduced in TREX1-deficient mice with *Unc93b1* 3d (Fig. 38b). B cells in *Trexl*$^{-/-}$;*Unc93bl*$^{3d/3d}$ mice also had a lower cell death rate (as represented by EMA^{+} cells) than their counterparts in *Trexl*$^{-/-}$ mice (Fig. 38c). These findings are consistent with less activation-induced cell death, which occurs as a regulatory mechanism of the B cell immune response.

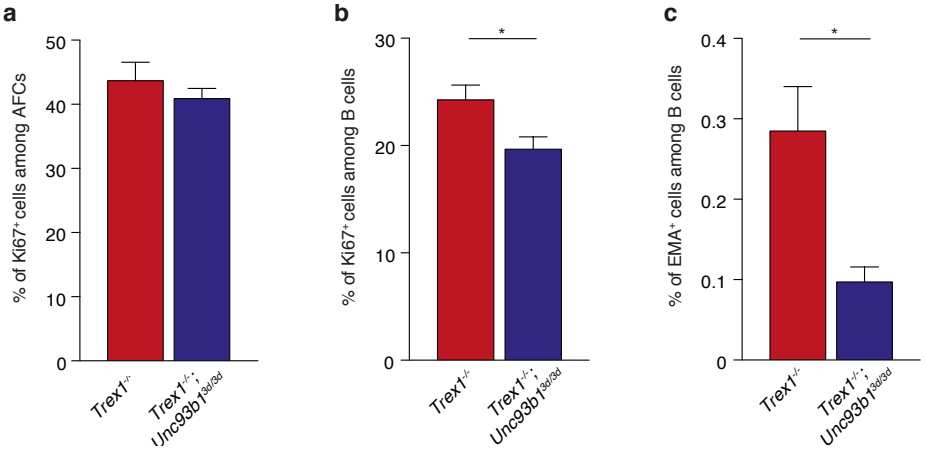

Figure 38. Endosomal TLR signaling facilitated B cell proliferation but also enhanced cell death in *Trexl*$^{-/-}$-mediated autoimmunity. Frequency of proliferating **(a)** AFCs and **(b)** B cells in spleens from *Trexl*$^{-/-}$ and *Trexl*$^{-/-}$;*Unc93bl*$^{3d/3d}$ mice. **(c)** Frequency of cell death rate (EMA^{+}) of B cells in *Trexl*$^{-/-}$ and *Trexl*$^{-/-}$;*Unc93bl*$^{3d/3d}$ mice. Bar graphs are shown as mean + SEM. Statistics were calculated by Mann-Whitney-U Test with *p < 0.05.

An extrafollicular $CD4^+$ helper T cell population in the splenic red pulp resembles T_{fh} cells regarding gene expression profile and B cell helper function. These cells were designated as extrafollicular T helper cells (T_{efh}) and have been shown to enable autoantibody production in murine models of autoimmunity.[102,103]

T_{efh} cell frequencies of $CD4^+$ T cells were measured via flow cytometry analysis in *Trex1*$^{-/-}$ and *Trex1*$^{-/-}$*;Unc93b1*$^{3d/3d}$ mice. T_{efh} cells were identified by downregulation of P-selectin glycoprotein ligand 1 (PSGL-1). Interestingly, the 3d mutation in *Unc93b1* resulted in a significantly reduced T_{efh} cell percentage among $CD4^+$ T cells compared to TREX1-deficient control mice (Fig. 39). Hence, the decrease in antibody-forming plasmablasts in *Trex1*$^{-/-}$*;Unc93b1*$^{3d/3d}$ animals is accompanied by a reduced T_{efh} cell frequency in these mice.

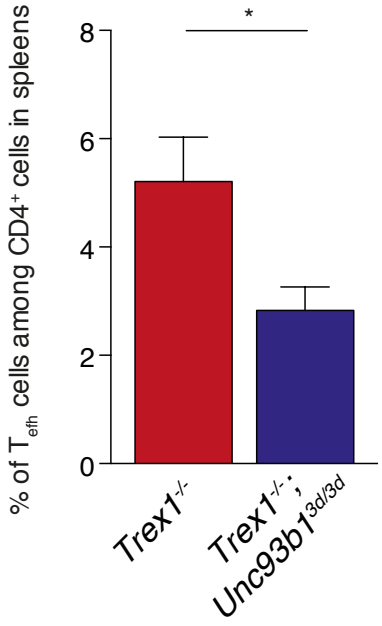

Figure 39. Impaired endosomal TLR signaling impedes T_{efh} cell differentiation in autoimmunity related to TREX1 deficiency. Frequency of extrafollicular T helper cells among $CD4^+$ T cells in spleens of *Trex1*$^{-/-}$ and *Trex1*$^{-/-}$*;Unc93b1*$^{3d/3d}$ mice (n = 17 for each group). T_{efh} cells were identified via their downregulation of PSGL-1 (CD162) in flow cytometry analysis. Bar graphs are displayed as mean + SEM. Statistics were calculated by Mann-Whitney-U Test with $^*p < 0.05$.

5 Discussion

In the **first part** of my project, I evaluated the importance of bystander cell activation in autoimmunity. Bystander activation occurs through a variety of mechanisms.[52] These mechanisms include secretion of cytokines (*e.g.* IL-1β), release of nucleic acids from damaged tissues, ejection of polymeric particles formed by the adaptor protein apoptosis-associated speck-like protein (ASC), and exosomal transfer of viral RNA and Ca^{2+} influx through gap junctions.

This study was conducted to evaluate whether dissemination of innate immune response by intercellular transfer of the second messenger molecule cGAMP promotes autoimmune disease. For this purpose, I successfully constructed mixed bone-marrow chimera in which cGAMP is accumulated due to the lack of TREX1 and subsequent cytosolic DNA-detection by cGAS. However, within the cGAMP-producing cells, cGAMP is not able to activate cell-intrinsic immune signaling due to the lack of STING but can be shuttled to neighboring bystander cells. Overall, the shown experiments provide evidence that in TREX1 deficiency transmission of cGAMP leads to innate immune signaling, IFN induction and, in the presence of environmental triggers, as exposure to UV light, tissue inflammation.

In particular, it was tested whether cGAMP transmission has the ability to activate primary immune cells *in-vivo* in autoimmunity. Intriguingly, cell-extrinsic cGAMP induced IRF3 signaling in cDCs in TREX1-deficient mice. Investigation of other cell types that are potential recipients of cGAMP, such as red pulp macrophages, neutrophils, B and T cells, did not reveal increased IRF3 phosphorylation in these populations.

It was questionable, which cell types deliver cGAMP to immune cells, such as cDCs, in TREX1 deficiency. The finding that innate immune induction was clearly detectable in *Mb21d1*$^{-/-}$ BM animals, in which *Mb21d1*$^{-/-}$ BM was transplanted into *Trex1*$^{-/-}$*;Tmem173*$^{gt/gt}$ mice, establishes that immune cells receive cGAMP from radioresistant cells. These largely consist of non-hematopoietic cells but also include some residual radioresistant hematopoietic cells, for example certain tissue-resident macrophages and mast cells.

Interestingly, *Mb21d1*$^{-/-}$ + dKO BM mice, which were reconstituted with a mixture of *Trex1*$^{-/-}$*;Tmem173*$^{gt/gt}$ and *Mb21d1*$^{-/-}$ bone marrow (*Mb21d1*$^{-/-}$ + dKO BM mice), and thus had a substantially larger number of hematopoietic cells that might provide cGAMP to neighboring cells in contrast to *Mb21d1*$^{-/-}$ BM mice, did not show a more robust immune activation than *Mb21d1*$^{-/-}$ BM animals. In fact, *Mb21d1*$^{-/-}$ + dKO BM mice displayed an ameliorated phenotype probably due to the 50% lower frequency of cGAMP-responsive *Mb21d1*$^{-/-}$ cells in the hematopoietic compartment. If hematopoietic cells were the primary source of cGAMP for bystander activation of immune cells, one would have expected a more pronounced immune response in *Mb21d1*$^{-/-}$ + dKO BM compared to *Mb21d1*$^{-/-}$ BM mice. However, this was not the case suggesting that immune cells are activated by cGAMP derived from non-hematopoietic cells. This notion is consistent with data demonstrating that *Trex1*$^{-/-}$ non-hematopoietic cells like keratinocytes and fibroblasts spontaneously produce IFN-β.[104]

The ability of DCs to regulate T cell immunity depends on their maturation state. cGAMP induces DC maturation and is an effective adjuvant for potentiating an antiviral CD8$^+$ T cell response after vaccination.[80–82] Surprisingly, although DCs undergoing cGAMP-mediated bystander activation exhibited increased IRF3 signaling, they did not evolve into mature, immunologically competent antigen presenting cells. Consistent with this, intercellular cGAMP transmission did not promote CD4$^+$ or CD8$^+$ T cell activation or differentiation in the steady state. These data indicate that cGAMP levels might have to cross a relatively high threshold level to render DCs immunogenic, which constitutes an important safety mechanism considering that it is not obvious how DCs matured via cGAMP transfer would select antigen for presentation.

Although I could detect an activation of DCs in response to cGAMP transfer, no impact on T cell proliferation was found. Instead, cGAMP-dependent bystander activation protected several immune cell subsets from apoptosis. Contrarily, others have previously reported that STING signaling promotes cell death in certain cell populations.[101,105,106] Even though these findings seem contradictory, the mentioned studies also indicated that a

rather high signal strength of STING is required for induction of apoptosis induction, which was presumably not the case here.

Even though cGAMP shuttling did not cause organ inflammation under steady state conditions, it mediated interface dermatitis after UV exposure. The pathogenesis of interface dermatitis is not very well understood and might depend on the underlying molecular reason for dermatitis development. Traditionally, it is thought to involve cytotoxic T cell-mediated keratinocytic cell death.[107] This would suggest that exogenous triggers, such as UV light, might enable T cell priming by antigen-presenting cells activated via cGAMP transfer. However, the histological picture of interface dermatitis can, under certain circumstances, develop independently of lymphocytes and thus does not necessarily imply T cell autoimmunity.[108]

This study provided evidence that cGAMP travel does neither promote B cell differentiation into antibody-forming cells nor autoantibody formation. There are several explanations that may account for this result. First, B cells might not serve as receiver cells for cGAMP. Second, B cell-intrinsic STING signaling alone might not lead to the activation of self-reactive B cells. There is limited data available regarding the role of cGAS-STING signaling in B cells. An early report indicated that B cell-expressed cGAS is critically involved in T-independent B cell responses, but this article was later retracted.[109] Later work revealed that B cells can be directly activated by cyclic-di-GMP in a STING-dependent manner[110]. Mice deficient for STING selectively in B cells had reduced antigen-specific IgG and IgA serum concentrations after intranasal immunization with ovalbumin and cyclic-di-GMP, although this decrease was much more pronounced with a global STING deficiency. Unlike for TLR driven models of autoimmunity, in which it has been shown that autoantibody production entirely relies on B cell-intrinsic signaling of the TLR adaptor MyD88[111], the contributions of B cell-intrinsic cGAS-STING signaling to the humoral response in STING-mediated autoimmunity have yet to be defined.

In summary of the **first part**, cGAMP-mediated bystander activation seems to serve as a mechanism to broaden innate immune activation in autoimmune diseases, which can lead to organ inflammation when triggering factors, such as UV light are encountered.

However, in the steady state intercellular cGAMP transfer was insufficient to induce self-directed adaptive immunity. This highlights the requirement for cell-intrinsic PRR engagement in the activation of autoreactive T and B cells. Collectively, these findings delineate the pathological consequences of cGAMP transmission in the development of systemic autoimmunity.

In the **second part** of this project, the focus was shifted on the contribution of TLR signaling to the development of cGAS-driven autoimmunity. Strikingly, in autoimmune-prone TREX1 deficiency an additional 3d mutation in *Unc93b1* led to increased organ inflammation in these animals compared to their TREX1-deficient counterparts.

It could further be demonstrated that *Trex1*$^{-/-}$*;Unc93b1*$^{3d/3d}$ animals suffer from more severe myocarditis, left ventricular hypertrophy and dysfunction as revealed by echocardiography, likely due to the elevated immune cell infiltration, in particular T cells, into the hearts of these animals. Besides T cells, cDCs were also found in higher quantities in affected tissues of *Trex1*$^{-/-}$*;Unc93b1*$^{3d/3d}$ mice. CD11c^{+} cells such as cDCs and some macrophages have been found to locally prevent apoptosis of tissue infiltrating T cells[103] and might thus promote T cell accumulation in target organs.

The 3d mutation, and thus probably endosomal TLR signaling, caused elevated IFN signaling and more severe organ inflammation in TREX1 deficiency. Reactivation of endogenous retroviruses might contribute to the increased IFN levels, since it has been suggested that retroelement-derived cDNA is a major substrate for TREX1 and therefore triggers autoimmunity in TREX1 deficiency.[74] Furthermore, TLR3, TLR7, and TLR9 seem to be key receptors in the control of ERV viremia. Notably, higher MuLV gp70 env expression was found in *Trex1*$^{-/-}$*;Unc93b1*$^{3d/3d}$ mice than in *Trex1*$^{-/-}$ controls. Thus, in *Trex1*$^{-/-}$*;Unc93b1*$^{3d/3d}$ mice, higher amounts of reactivated ERVs could act as inducers of an elevated IFN signature due to the recognition of viral cDNA by cGAS, resulting in the upregulation of inflammatory cytokines and type I IFN.

Survival data of *Trex1*$^{-/-}$ mice versus double deficient mice for TREX1 and UNC93B1 were in marked contrast to observations on heart pathology because *Trex1*$^{-/-}$*;Unc93b1*$^{3d/3d}$ animals

had a significantly longer life span than *Trex1*$^{-/-}$ mice. To gain a better insight into the underlying mechanisms of improved survival, autoantibody production was examined in more detail. Strikingly, animals homozygously harboring the *Unc93b1* 3d mutation showed virtually no anti-nucleosome or anti-RNA antibody production. The same was true for *Trex1*$^{-/-}$*; Tmem173*$^{gt/gt}$ animals, which do not feature a functional STING adaptor protein and therefore cannot signal via the cytosolic cGAS-STING pathway. These findings reveal that STING and UNC93B1 collaborate on ANA formation.

It is reasonable to assume that the absence of ANAs observed in *Trex1*$^{-/-}$*;Unc93b1*$^{3d/3d}$ animals can be attributed to the deficiency of endosomal NA-sensing TLRs, since several studies demonstrated that the formation of anti-DNA antibodies in autoimmunity requires TLR9, whereas the production of anti-RNA antibodies needs TLR7.[100,112] Thus, STING presumably licenses TLR activation.

A recent study has revealed proapoptotic functions of STING[101]. Consistent with this, I found that the death rate of splenocytes from TREX1- and STING double-deficient mice was reduced compared to *Trex1*$^{-/-}$ animals. Cell death potentially increases free DNA and RNA in the serum, which can then be recognized by TLRs in B cells, ultimately leading to the production of ANAs. Notably, free serum DNA was diminished in *Trex1*$^{-/-}$ mice lacking STING when compared to those with functional STING.

A limitation of using *Trex1*$^{-/-}$*;Unc93b1*$^{3d/3d}$ mice is that although the observed phenotype is most likely due to defective TLR signaling, other causes cannot be completely excluded. To formally prove that TLRs are required for the B cell activation and the formation of ANAs in TREX1-deficient animals, the most suitable model would be to generate TREX1-deficient mice with a single TLR knockout. TLR9 would be the best candidate as it is able to recognize DNA that accumulates in TREX1-deficient cells. In mice, however, the coding gene sequences of both *Trex1* and *Tlr9* are located in relatively close proximity on chromosome 9, which makes the generation of double knockout animals by intercrossing difficult. This obstacle could be overcome by using CRISPR/Cas9 technology to generate double-knockout mice. An alternative complementary experiment would be the adoptive transfer of TLR9-deficient B cells into *Trex1*$^{-/-}$*;Rag1*$^{-/-}$ mice which fail to generate mature B

or T lymphocytes to investigate whether the production of ANAs is specifically dependent on TLR9 signaling in B cells.

Taken together, the **second part** of this thesis provided evidence for the co-operation of STING and NA-sensing endosomal TLRs in establishing the full clinical picture of *Trex1*$^{-/-}$-associated autoimmunity. Surprisingly, defects of UNC93B1 in TREX1 deficiency promoted IFN production and T cell-dependent tissue inflammation but at the same time abolished ANA formation and resulted in improved survival.

6 Concluding remarks

Trex1$^{-/-}$-associated autoimmunity is characterized by the accumulation of intracellular DNA, its aberrant recognition as a danger signal and subsequent excessive immune activation. My experiments successfully substantiated the occurrence of cGAMP migration to bystander cells *in vivo* and confirmed its ability to induce innate immune activation in autoimmunity, which leads to organ inflammation in the presence of triggering environmental factors. Furthermore, I was able to show that NA-sensing pathways, including recognition via endosomal TLRs and the cytosolic cGAS-STING pathway, regulate each other in a complex interplay. The results of both projects provide insights into the interaction of immune cells through cGAMP-mediated bystander activation as well as between different NA-detecting sensors in the development of autoimmune diseases. These advances support the effort to develop new therapeutic strategies for patients suffering from systemic autoimmunity.

7 References

1. Medzhitov, R. & Janeway, C. Innate immune recognition: mechanisms and pathways. *Immunol. Rev.* **173**, 89–97 (2000).
2. Chen, Q., Sun, L. & Chen, Z. J. Regulation and function of the cGAS-STING pathway of cytosolic DNA sensing. *Nat. Immunol.* **17**, 1142–1149 (2016).
3. Turvey, S. E. & Broide, D. H. Chapter 2: Innate Immunity. *J Allergy Clin Immunol* **125**, S24–S32 (2010).
4. Land, W. G. Innate Alloimmunity, Part 1: Innate Immunity and Host Defense. *Lengerich, Germany: Pabst International Publishers* (2011).
5. Herzner, A.-M. *et al.* Sequence-specific activation of the DNA sensor cGAS by Y-form DNA structures as found in primary HIV-1 cDNA. *Nat Immunol* **16**, 1025–1033 (2015).
6. Sun, L., Wu, J., Du, F., Chen, X. & Chen, Z. J. Cyclic GMP-AMP synthase is a cytosolic DNA sensor that activates the type I interferon pathway. *Science* **339**, 786–91 (2013).
7. Wu, J. *et al.* Cyclic-GMP-AMP Is an Endogenous Second Messenger in Innate Immune Signaling by Cytosolic DNA. *Science* **339**, 826-830 (2013).
8. Xiao, T. S. & Fitzgerald, K. A. The cGAS-STING pathway for DNA sensing. *Mol Cell* **51**, 135–139 (2013).
9. Ablasser, A. *et al.* cGAS produces a 2'-5'-linked cyclic dinucleotide second messenger that activates STING. *Nature* **498**, 380–384 (2013).
10. Cai, X., Chiu, Y.-H. & Chen, Z. J. The cGAS-cGAMP-STING pathway of cytosolic DNA sensing and signaling. *Mol. Cell* **54**, 289–296 (2014).
11. Liu, S. *et al.* Phosphorylation of innate immune adaptor proteins MAVS, STING, and TRIF induces IRF3 activation. *Science* **347**, aaa2630 (2015).
12. Ishikawa, H. & Barber, G. N. STING is an endoplasmic reticulum adaptor that facilitates innate immune signalling. *Nature* **455**, 674–678 (2008).
13. Galluzzi, L., Vanpouille-Box, C., Bakhoum, S. F. & Demaria, S. SnapShot: CGAS-STING Signaling. *Cell* **173**, 276-276.e1 (2018).

14. Hertlein, E., Wang, J., Ladner, K. J., Bakkar, N. & Guttridge, D. C. RelA/p65 Regulation of IκBβ. *Mol Cell Biol* **25**, 4956–4968 (2005).
15. Adli, M. & Baldwin, A. S. IKK-i/IKKepsilon controls constitutive, cancer cell-associated NF-kappaB activity via regulation of Ser-536 p65/RelA phosphorylation. *J. Biol. Chem.* **281**, 26976–26984 (2006).
16. Mercurio, F. *et al.* IκB Kinase (IKK)-Associated Protein 1, a Common Component of the Heterogeneous IKK Complex. *Mol Cell Biol* **19**, 1526–1538 (1999).
17. Pradère, J.-P. *et al.* Negative regulation of NF-κB p65 activity by serine 536 phosphorylation. *Sci Signal* **9**, ra85 (2016).
18. Medzhitov, R. & Janeway, C. A. Innate immunity: impact on the adaptive immune response. *Curr. Opin. Immunol.* **9**, 4–9 (1997).
19. Flo, T. H. & Aderem, A. Pathogen Recognition by Toll-like Receptors. in *NeuroImmune Biology* Vol. 5 167–182 (2005).
20. Kawasaki, T. & Kawai, T. Toll-Like Receptor Signaling Pathways. *Front Immunol* **5**, 461 (2014).
21. Georg, P. & Sander, L. E. Innate sensors that regulate vaccine responses. *Curr. Opin. Immunol.* **59**, 31–41 (2019).
22. Tanji, H. *et al.* Toll-like receptor 8 senses degradation products of single-stranded RNA. *Nature Structural & Molecular Biology* **22**, 109–115 (2015).
23. Roers, A., Hiller, B. & Hornung, V. Recognition of Endogenous Nucleic Acids by the Innate Immune System. *Immunity* **44**, 739–754 (2016).
24. Fitzgerald, K. A. & Kagan, J. C. Toll-like Receptors and the Control of Immunity. *Cell* **180**, 1044–1066 (2020).
25. Kim, Y.-M., Brinkmann, M. M., Paquet, M.-E. & Ploegh, H. L. UNC93B1 delivers nucleotide-sensing toll-like receptors to endolysosomes. *Nature* **452**, 234–238 (2008).
26. Huh, J.-W. *et al.* UNC93B1 is essential for the plasma membrane localization and signaling of Toll-like receptor 5. *Proc. Natl. Acad. Sci. U.S.A.* **111**, 7072–7077 (2014).
27. Pelka, K. *et al.* The Chaperone UNC93B1 Regulates Toll-like Receptor Stability Independently of Endosomal TLR Transport. *Immunity* **48**, 911-922.e7 (2018).

28. Shiokawa, D., Shika, Y., Saito, K., Yamazaki, K. & Tanuma, S. Physical and biochemical properties of mammalian DNase X proteins: non-AUG translation initiation of porcine and bovine mRNAs for DNase X. *Biochem J* **392**, 511–517 (2005).
29. Morita, M. *et al.* Gene-targeted mice lacking the Trex1 (DNase III) 3'→5' DNA exonuclease develop inflammatory myocarditis. *Mol Cell Biol* **24**, 6719–27 (2004).
30. Takeshita, H. *et al.* Mouse deoxyribonuclease I (DNase I): biochemical and immunological characterization, cDNA structure and tissue distribution. *Biochem. Mol. Biol. Int.* **42**, 65–75 (1997).
31. Hartmann, G. Nucleic Acid Immunity. *Adv. Immunol.* **133**, 121–169 (2017).
32. Martínez Valle, F., Balada, E., Ordi-Ros, J. & Vilardell-Tarres, M. DNase 1 and systemic lupus erythematosus. *Autoimmunity Reviews* **7**, 359–363 (2008).
33. Napirei, M. *et al.* Features of systemic lupus erythematosus in Dnase1-deficient mice. *Nat. Genet.* **25**, 177–181 (2000).
34. Evans, C. J. & Aguilera, R. J. DNase II: genes, enzymes and function. *Gene* **322**, 1–15 (2003).
35. Baum, R. *et al.* Cutting edge: AIM2 and endosomal TLRs differentially regulate arthritis and autoantibody production in DNase II-deficient mice. *J. Immunol.* **194**, 873–877 (2015).
36. Pawaria, S. *et al.* Cutting Edge: DNase II Deficiency Prevents Activation of Autoreactive B Cells by Double-Stranded DNA Endogenous Ligands. *The Journal of Immunology* **194**, 1403–1407 (2015).
37. Lindahl, T., Gally, J. A. & Edelman, G. M. Properties of Deoxyribonuclease III from Mammalian Tissues. *J. Biol. Chem.* **244**, 5014–5019 (1969).
38. Wolf, C. *et al.* RPA and Rad51 constitute a cell intrinsic mechanism to protect the cytosol from self DNA. *Nat Commun* **7**, 11752 (2016).
39. Grieves, J. L. *et al.* Exonuclease TREX1 degrades double-stranded DNA to prevent spontaneous lupus-like inflammatory disease. *Proc. Natl. Acad. Sci. U.S.A.* **112**, 5117–5122 (2015).

40. Chowdhury, D. *et al.* The exonuclease TREX1 is in the SET complex and acts in concert with NM23-H1 to degrade DNA during granzyme A-mediated cell death. *Mol. Cell* **23**, 133–142 (2006).
41. Stetson, D. B. Endogenous retroelements and autoimmune disease. *Curr. Opin. Immunol.* **24**, 692–697 (2012).
42. Volkman, H. E. & Stetson, D. B. The enemy within: endogenous retroelements and autoimmune disease. *Nat. Immunol.* **15**, 415–422 (2014).
43. Yang, Y.-G., Lindahl, T. & Barnes, D. E. Trex1 exonuclease degrades ssDNA to prevent chronic checkpoint activation and autoimmune disease. *Cell* **131**, 873–886 (2007).
44. Harley, I. T. W., Kaufman, K. M., Langefeld, C. D., Harley, J. B. & Kelly, J. A. Genetic Susceptibility to Lupus: New Insights from fine mapping and genome-wide association studies. *Nat Rev Genet* **10**, 285–290 (2009).
45. Rönnblom, L. The importance of the type I interferon system in autoimmunity. *Clin. Exp. Rheumatol.* **34**, 21–24 (2016).
46. Kaplan, M. J. & Salmon, J. E. How does IFN-α insult the vasculature? Let me count the ways. *Arthritis Rheum* **63**, 334–336 (2011).
47. Lee-Kirsch, M. A., Wolf, C. & Günther, C. Aicardi-Goutières syndrome: a model disease for systemic autoimmunity. *Clin. Exp. Immunol.* **175**, 17–24 (2014).
48. Crow, Y. J. & Manel, N. Aicardi-Goutières syndrome and the type I interferonopathies. *Nat Rev Immunol* **15**, 429–440 (2015).
49. Lockshin, M. D. Sex differences in autoimmune disease. *Lupus* **15**, 753–756 (2006).
50. Kaul, A. *et al.* Systemic lupus erythematosus. *Nature Reviews Disease Primers* **2**, 1–21 (2016).
51. Chen, L. *et al.* Genome-wide assessment of genetic risk for systemic lupus erythematosus and disease severity. *Hum. Mol. Genet.* **29,** 1745-1756 (2020).
52. Holmgren, A. M., McConkey, C. A. & Shin, S. Outrunning the Red Queen: bystander activation as a means of outpacing innate immune subversion by intracellular pathogens. *Cell Mol Immunol* **14**, 14–21 (2017).

53. Tough, D. F., Borrow, P. & Sprent, J. Induction of Bystander T Cell Proliferation by Viruses and Type I Interferon in Vivo. *Science* **272**, 1947–1950 (1996).
54. Murali-Krishna, K. *et al.* Counting Antigen-Specific CD8 T Cells: A Reevaluation of Bystander Activation during Viral Infection. *Immunity* **8**, 177–187 (1998).
55. Zarozinski, C. C. & Welsh, R. M. Minimal Bystander Activation of CD8 T Cells during the Virus-induced Polyclonal T Cell Response. *J Exp Med* **185**, 1629–1640 (1997).
56. Ablasser, A. *et al.* Cell intrinsic immunity spreads to bystander cells via the intercellular transfer of cGAMP. *Nature* **503**, 530–534 (2013).
57. Gentili, M. *et al.* Transmission of innate immune signaling by packaging of cGAMP in viral particles. *Science* **349**, 1232–1236 (2015).
58. Zhou, C. *et al.* Transfer of cGAMP into Bystander Cells via LRRC8 Volume-Regulated Anion Channels Augments STING-Mediated Interferon Responses and Anti-viral Immunity. *Immunity* (2020).
59. Ablasser, A. *et al.* TREX1 deficiency triggers cell-autonomous immunity in a cGAS-dependent manner. *J Immunol* **192**, 5993–5997 (2014).
60. Chen, Q. *et al.* Carcinoma-astrocyte gap junctions promote brain metastasis by cGAMP transfer. *Nature* **533**, 493–498 (2016).
61. Marcus, A. *et al.* Tumor-Derived cGAMP Triggers a STING-Mediated Interferon Response in Non-tumor Cells to Activate the NK Cell Response. *Immunity* **49**, 754-763.e4 (2018).
62. Schadt, L. *et al.* Cancer-Cell-Intrinsic cGAS Expression Mediates Tumor Immunogenicity. *Cell Reports* **29**, 1236-1248.e7 (2019).
63. Pacheco, Y. *et al.* Bystander activation and autoimmunity. *J Autoimmun* **103**, 102301 (2019).
64. Smatti, M. K. *et al.* Viruses and Autoimmunity: A Review on the Potential Interaction and Molecular Mechanisms. *Viruses* **11**, 762 (2019).
65. Sauer, J.-D. *et al.* The N-ethyl-N-nitrosourea-induced Goldenticket mouse mutant reveals an essential function of Sting in the in vivo interferon response to Listeria monocytogenes and cyclic dinucleotides. *Infect. Immun.* **79**, 688–694 (2011).

66. Schoggins, J. W. *et al.* Pan-viral specificity of IFN-induced genes reveals new roles for cGAS in innate immunity. *Nature* **505**, 691–695 (2014).
67. Tabeta, K. *et al.* The Unc93b1 mutation 3d disrupts exogenous antigen presentation and signaling via Toll-like receptors 3, 7 and 9. *Nature immunology* **7**, 156–164 (2006).
68. Losman, M. J., Fasy, T. M., Novick, K. E. & Monestier, M. Monoclonal autoantibodies to subnucleosomes from a MRL/Mp(-)+/+ mouse. Oligoclonality of the antibody response and recognition of a determinant composed of histones H2A, H2B, and DNA. *The Journal of Immunology* **148**, 1561–1569 (1992).
69. Blanco, F., Kalsi, J. & Isenberg, D. A. Analysis of antibodies to RNA in patients with systemic lupus erythematosus and other autoimmune rheumatic diseases. *Clin Exp Immunol* **86**, 66–70 (1991).
70. Dobin, A. *et al.* STAR: ultrafast universal RNA-seq aligner. *Bioinformatics* **29**, 15–21 (2013).
71. Love, M. I., Huber, W. & Anders, S. Moderated estimation of fold change and dispersion for RNA-seq data with DESeq2. *Genome Biol* **15**, 550 (2014).
72. Subramanian, A. *et al.* Gene set enrichment analysis: A knowledge-based approach for interpreting genome-wide expression profiles. *Proc Natl Acad Sci U S A* **102**, 15545–15550 (2005).
73. Yoneyama, M. *et al.* Direct triggering of the type I interferon system by virus infection: activation of a transcription factor complex containing IRF-3 and CBP/p300. *EMBO J* **17**, 1087–1095 (1998).
74. Stetson, D. B., Ko, J. S., Heidmann, T. & Medzhitov, R. Trex1 prevents cell-intrinsic initiation of autoimmunity. *Cell* **134**, 587–98 (2008).
75. Lee, P. Y. *et al.* TLR7-dependent and FcγR-independent production of type I interferon in experimental mouse lupus. *J Exp Med* **205**, 2995–3006 (2008).
76. Shapiro-Shelef, M. *et al.* Blimp-1 is required for the formation of immunoglobulin secreting plasma cells and pre-plasma memory B cells. *Immunity* **19**, 607–620 (2003).
77. Rawstron, A. C. Immunophenotyping of Plasma Cells. *Current Protocols in Cytometry* **36**, 6.23.1-6.23.14 (2006).

78. Nojima, T. *et al.* In-vitro derived germinal centre B cells differentially generate memory B or plasma cells in vivo. *Nature Communications* **2**, 465 (2011).
79. Gall, A. *et al.* Autoimmunity initiates in nonhematopoietic cells and progresses via lymphocytes in an interferon-dependent autoimmune disease. *Immunity* **36**, 120–31 (2012).
80. Li, T. *et al.* Antitumor Activity of cGAMP via Stimulation of cGAS-cGAMP-STING-IRF3 Mediated Innate Immune Response. *Sci Rep* **6**, (2016).
81. Gutjahr, A. *et al.* The STING ligand cGAMP potentiates the efficacy of vaccine-induced CD8+ T cells. *JCI Insight* **4**, e125107 (2019).
82. Wang, H. *et al.* cGAS is essential for the antitumor effect of immune checkpoint blockade. *Proc Natl Acad Sci U S A* **114**, 1637–1642 (2017).
83. Gehrke, N. *et al.* Oxidative damage of DNA confers resistance to cytosolic nuclease TREX1 degradation and potentiates STING-dependent immune sensing. *Immunity* **39**, 482–495 (2013).
84. Scholtissek, B. *et al.* Immunostimulatory Endogenous Nucleic Acids Drive the Lesional Inflammation in Cutaneous Lupus Erythematosus. *J. Invest. Dermatol.* **137**, 1484–1492 (2017).
85. Lee, B. L. *et al.* UNC93B1 mediates differential trafficking of endosomal TLRs. *eLife* ***2*** e00291 (2013).
86. Maschalidi, S. *et al.* UNC93B1 interacts with the calcium sensor STIM1 for efficient antigen cross-presentation in dendritic cells. *Nat Commun* **8**, 1640 (2017).
87. Deguine, J., Lee, B. L., Newman, Z. R. & Barton, G. M. No antigen-presentation defect in Unc93b1(3d/3d) (3d) mice. *Nat. Immunol.* **14**, 1101–1102 (2013).
88. Tabeta, K., Hoebe, K., Janssen, E. M., Xia, Y. & Beutler, B. Respond to 'No antigen-presentation defect in Unc93b1(3d/3d) (3d) mice'. *Nat. Immunol.* **14**, 1102–1103 (2013).
89. Marshak-Rothstein, A. Toll-like receptors in systemic autoimmune disease. *Nat. Rev. Immunol.* **6**, 823–835 (2006).

90. Crozier, I. G., Li, E., Milne, M. J. & Nicholls, M. G. Cardiac involvement in systemic lupus erythematosus detected by echocardiography. *Am. J. Cardiol.* **65**, 1145–1148 (1990).
91. Pieretti, J. *et al.* Systemic lupus erythematosus predicts increased left ventricular mass. *Circulation* **116**, 419–426 (2007).
92. Gardin, J. M., Siri, F. M., Kitsis, R. N., Edwards, J. G. & Leinwand, L. A. Echocardiographic Assessment of Left Ventricular Mass and Systolic Function in Mice. *Circulation Research* **76**, 907–914 (1995).
93. Ardouin, L. *et al.* Broad and Largely Concordant Molecular Changes Characterize Tolerogenic and Immunogenic Dendritic Cell Maturation in Thymus and Periphery. *Immunity* **45**, 305–318 (2016).
94. Weiss, R. A. The discovery of endogenous retroviruses. *Retrovirology* **3**, 67 (2006).
95. Yu, P. *et al.* Nucleic acid-sensing Toll-like receptors are essential for the control of endogenous retrovirus viremia and ERV-induced tumors. *Immunity* **37**, 867–879 (2012).
96. Scrimieri, F. *et al.* Murine leukemia virus envelope gp70 is a shared biomarker for the high-sensitivity quantification of murine tumor burden. *OncoImmunology* **2**, e26889 (2013).
97. Stel, V. S., Dekker, F. W., Tripepi, G., Zoccali, C. & Jager, K. J. Survival analysis I: the Kaplan-Meier method. *Nephron Clin Pract* **119**, c83-88 (2011).
98. Zee, J. & Xie, S. X. The Kaplan-Meier Method for Estimating and Comparing Proportions in a Randomized Controlled Trial with Dropouts. *Biostat Epidemiol* **2**, 23–33 (2018).
99. Christensen, S. R. *et al.* Toll-like receptor 9 controls anti-DNA autoantibody production in murine lupus. *J. Exp. Med.* **202**, 321–331 (2005).
100. Christensen, S. R. *et al.* Toll-like receptor 7 and TLR9 dictate autoantibody specificity and have opposing inflammatory and regulatory roles in a murine model of lupus. *Immunity* **25**, 417–428 (2006).

101. Gulen, M. F. *et al.* Signalling strength determines proapoptotic functions of STING. *Nat Commun* **8**, 427 (2017).
102. Odegard, J. M. *et al.* ICOS-dependent extrafollicular helper T cells elicit IgG production via IL-21 in systemic autoimmunity. *J. Exp. Med.* **205**, 2873–2886 (2008).
103. Teichmann, L. L. *et al.* Local triggering of the ICOS coreceptor by CD11c(+) myeloid cells drives organ inflammation in lupus. *Immunity* **42**, 552–565 (2015).
104. Peschke, K. *et al.* Loss of Trex1 in Dendritic Cells Is Sufficient to Trigger Systemic Autoimmunity. *J Immunol* **197**, 2157–2166 (2016).
105. Gaidt, M. M. *et al.* The DNA Inflammasome in Human Myeloid Cells Is Initiated by a STING-Cell Death Program Upstream of NLRP3. *Cell* **171**, 1110-1124.e18 (2017).
106. Larkin, B. *et al.* Cutting Edge: Activation of STING in T Cells Induces Type I IFN Responses and Cell Death. *J. Immunol.* **199**, 397–402 (2017).
107. Wenzel, J. Cutaneous lupus erythematosus: new insights into pathogenesis and therapeutic strategies. *Nat Rev Rheumatol* **15**, 519–532 (2019).
108. Page, A. *et al.* IKKbeta leads to an inflammatory skin disease resembling interface dermatitis. *J. Invest. Dermatol.* **130**, 1598–1610 (2010).
109. Zeng, M. *et al.* MAVS, cGAS, and endogenous retroviruses in T-independent B cell responses. *Science* **346**, 1486–1492 (2014).
110. Hahn, W. O. *et al.* cGAS-mediated control of blood-stage malaria promotes Plasmodium-specific germinal center responses. *JCI Insight* **3**, e94142 (2018).
111. Teichmann, L. L., Schenten, D., Medzhitov, R., Kashgarian, M. & Shlomchik, M. J. Signals via the adaptor MyD88 in B cells and DCs make distinct and synergistic contributions to immune activation and tissue damage in lupus. *Immunity* **38**, 528–540 (2013).
112. Jackson, S. W. *et al.* Opposing impact of B cell-intrinsic TLR7 and TLR9 signals on autoantibody repertoire and systemic inflammation. *J. Immunol.* **192**, 4525–4532 (2014).

8 Abbreviations

AFC	antibody-forming cell
ANA	anti-nuclear antibody
APC	antigen-presenting cell
BM	bone marrow
BSA	bovine serum albumin
bp	base pairs
CCR	C-C chemokine receptor
CD	cluster of differentiation
cDC	conventional dendritic cell
cGAMP	cyclic guanosine monophosphate
cGAS	cyclic GMP-AMP-synthase
CRISPR	clustered regularly interspaced short palindromic repeats
DAMP	danger-associated molecular pattern
DC	dendritic cell
ddH_2O	distilled deionized water
DNA	deoxyribonucleic acid
DNase	deoxyribonuclease
ds	double-stranded
EDTA	ethylenediaminetetraacetic acid
ELISA	enzyme-linked immunosorbent assay
ER	endoplasmatic reticulum
ERV	endogenous retrovirus
FACS	fluorescence activated cell sorting
FBS	fetal bovine serum
Fig	figure
FITC	fluorescein isothiocyanate
FSC	forward scatter

gt	goldenticket mutation
H&E	hematoxylin and eosin
HBSS	Hank's balanced salt solution
HEPES	4-(2-hydroxyethyl)-1-piperazineethanesulfonic acid
IFN	interferon
IκB	inhibitor of NF-κB
IKK	IκB kinase
IL	interleukin
IRF	interferon regulatory factor
ISG	interferon stimulated gene
kb	kilo base pair
KO	knockout
LRR	leucin-rich repeat
MHC	major histocompatibility complex
MuLV	murine leukemia virus
MyD88	myeloid differentiation primary response gene 88
NA	nucleic acid
NES	normalized enrichment score
NF-κB	nuclear factor kappa-light-chain-enhancer of activated B cells
PAMP	pathogen-associated molecular pattern
PBS	phosphate-buffered saline
PCR	polymerase chain reaction
pDC	plasmacytoid dendritic cell
PE	phycoerythrin
PFA	paraformaldehyde
PGS	Partek® Genomics Suite®
PMA	phorbol 12-myristate 13-acetate
PRR	pathogen recognition receptor

PSGL-1	P-selectin glycoprotein ligand 1
qRT-PCR	quantitative reverse transcriptase polymerase chain reaction
rcf	relative centrifugal force
RIG-I	retinoic acid inducible gene I
RNA	ribonucleic acid
RPMI	Roswell Park Memorial Institute Medium
RT	room temperature
Sca-1	stem cell antigen 1
SEM	standard error of the mean
SLE	systemic lupus erythematosus
ss	single-stranded
STING	stimulator of interferon genes
TANK	TRAF family member-associated nuclear NF-κB activator
TBK1	TANK binding kinase 1
TBS	Tris-buffered saline
TCR	T cell receptor
T_{efh}	extrafollicular T helper
T_{fh}	follicular T helper
TLR	toll-like receptor
TNF	tumor necrosis factor
TREX1	three prime repair exonuclease 1
UNC93B1	unc-93 homolog B1
wt	wild-type

9 Index of Figures and Tables

10 Acknowledgements

First of all, I would like to thank **Professor Peter Brossart** for the opportunity to conduct my research and complete my doctoral thesis in his Institute for Internal Medicine III at the University of Bonn. Many thanks to my second reviewer, **Professor Sven Burgdorf,** for dedicating his time and efforts to reading and examining this work. I would also like to express my gratitude towards **Professor Jörg Wenzel** and **Professor Jochen Dingfelder** for their commitment to being part of my dissertation committee.

In particular, I would like to express my gratitude towards **Dr. Lino Teichmann** for his supervision and constant support throughout my research project. Thank you, Lino, for always contributing valuable ideas and advice as my mentor, for your motivation when things did not go as planned, and of course for reading my manuscripts and your constructive suggestions.

I am very grateful to my colleagues in the lab for all the interesting discussions and for your help and assistance whenever needed. Thank you, Kevin, for your help in the lab and mouse house, the many hours we spent together at the FACS and of course for the good time we had outside of work. I would also like to thank AG Wolf, AG Feldmann, and AG Paeschke for the consistent good atmosphere in- and outside the lab. Especially I would like to mention Calvin, Miri, and Sebastian - thank you for a great time! Many thanks to Thomas from the Institute of Cardiology for your help with the ultrasound examinations of the mice. Additionally, I want to thank Professor Natalio Garbi and Professor Wolfgang Kastenmüller for the working cooperation and their groups for the friendly and helpful assistance anytime I visited the lab. Thanks to everyone from the Flow Cytometry Core Facility for your help and insights, whenever I got stuck with my experiments. Many thanks to Gabi and Meike for carefully reading my manuscripts and for the useful comments and suggestions for improvement. Additionally, I would like to thank the entire Di Monte group for making my last year of work a valuable and enjoyable experience.

Special thanks to my friends and family for making the last years an amazing journey. You shared so many great moments with me and were always there for me when I needed help in stressful times. Loads of thanks go to Tatjana, Paul and Mino, Meike, Julian and Fabian. You have made my life better! Finally, my deepest gratitude goes to my parents for making all this possible and for your constant support throughout the last thirty years.

Thank You!